

ENHANCED COMPUTERIZED SURGICAL PLANNING SYSTEM IN  
CRANIOMAXILLOFACIAL SURGERY

A Dissertation

by

YU-BING CHANG

Submitted to the Office of Graduate Studies of  
Texas A&M University  
in partial fulfillment of the requirements for the degree of

DOCTOR OF PHILOSOPHY

May 2011

Major Subject: Electrical Engineering

ENHANCED COMPUTERIZED SURGICAL PLANNING SYSTEM IN  
CRANIOMAXILLOFACIAL SURGERY

A Dissertation

by

YU-BING CHANG

Submitted to the Office of Graduate Studies of  
Texas A&M University  
in partial fulfillment of the requirements for the degree of

DOCTOR OF PHILOSOPHY

Approved by:

Chair of Committee,	Zixiang Xiong
Committee Members,	Ulisses Braga-Neto
	Jim Ji
	Harold P. Boas
Head of Department,	Costas N. Georghiades

May 2011

Major Subject: Electrical Engineering

## ABSTRACT

Enhanced Computerized Surgical Planning System in Craniomaxillofacial Surgery.

(May 2011)

Yu-Bing Chang, B.S., National Cheng Kung University;

M.S., National Taiwan University

Chair of Advisory Committee: Dr. Zixiang Xiong

In the field of craniomaxillofacial (CMF) surgery, surgical planning is an important and necessary procedure due to the complex nature of the craniofacial skeleton. Computed tomography (CT) has brought about a revolution in virtual diagnosis, surgical planning and simulation, and evaluation of treatment outcomes. It provides high-quality 3D images and models of skull for computer-aided surgical planning system (CSPS).

During the planning process, one of the essential steps is to reestablish the dental occlusion. In the first project, a new approach is presented to automatically and efficiently reestablish dental occlusion. It includes two steps. The first step is to initially position the models based on dental curves and a point matching technique. The second step is to reposition the models to the final desired occlusion based on iterative surface-based minimum distance mapping with collision constraints. With linearization of rotation matrix, the alignment is modeled by solving quadratic programming. The simulation was completed on 12 sets of digital dental models. Two sets of dental models were partially edentulous, and another two sets have first premolar extractions for orthodontic treatment. Two validation methods were applied to the articulated models. The results show that using the proposed method, the dental models can be successfully articulated with a small degree of deviations from the occlusion achieved with the gold-standard method.

Low contrast resolution in CBCT image has become its major limitation in building skull model. Intensive hand-segmentation is required to reconstruct the skull model. Thin bone images are particularly affected by this limitation. In the second project, a novel segmentation approach is presented based on wavelet active shape model (WASM) for a particular interest in the outer surface of the anterior wall of maxilla. 19 CBCT datasets are used to conduct two experiments. This model-based segmentation approach is validated and compared with three different segmentation approaches. The results show that the performance of this model-based segmentation approach is better than those of the other approaches. It can achieve  $0.25 \pm 0.2\text{mm}$  of surface error distance from the ground truth of the bone surface.

Field of view (FOV) can be reduced in order to reduce unnecessary radiation dose in CBCT. This ROI imaging is common in most of the dentomaxillofacial imaging and orthodontic practices. However, a truncation effect is created due to the truncation of projection images and becomes one of the limitation in CBCT. In the third project, a method for small region of interest (ROI) imaging and reconstruction of the image of ROI in CBCT and two experiments for measurement of dosage are presented. The first experiment shows at least 60% and 70% of radiation dose can be reduced. It also demonstrates that the image quality was still acceptable with little variation of gray by using the traditional truncation correction approach for ROI imaging. The second experiment demonstrates that the images reconstructed by CBCT reconstruction algorithms without truncation correction can be degraded to unacceptable image quality.

To my parents

## ACKNOWLEDGMENTS

I would like to thank my parents for their spiritual and financial supports during my study. I did not need to worry about anything so that I could be entirely concentrated on my research. When I needed any help anytime, they were always the first ones to provide support to ensure that I could continue my study. I also would like to thank my advisor Prof. Xiong for providing the opportunity of conducting off-campus research at the Methodist Hospital Research Institute. He always encouraged me and inspired confidence in me. I also want to thank my supervisors Dr. Zhou and Dr. Xia at the Methodist Hospital Research Institute for their lessons on research and paper writing for this study. The comments made by my committee members were very helpful to my dissertation. I appreciate what my friends have brought to me. They make my life complete.

## TABLE OF CONTENTS

CHAPTER		Page
I	INTRODUCTION TO COMPUTERIZED SURGICAL PLANNING SYSTEM (CSPS) IN CRANIOMAXILLOFACIAL (CMF) SURGERY . . . . .	1
	A. Traditional Surgical Planning in CMF Surgery . . . . .	3
	B. Computerized Surgical Planning System (CSPS) in CMF . . . . .	5
	1. Composite Skull Model . . . . .	5
	2. Natural Head Position in Composite Skull Model . . . . .	7
	3. Computer-aided Surgical Simulation (CASS) . . . . .	9
	4. Transfer Digital Plan to Patient . . . . .	10
	C. The Organization of the Dissertation . . . . .	11
II	REESTABLISHMENT OF DIGITAL DENTAL OCCLUSION . . . . .	14
	A. Introduction to Digital Dental Occlusion . . . . .	14
	B. Data Acquisition and Preprocessing . . . . .	17
	C. Initial Alignment . . . . .	18
	1. Identification of Feature Points on Maxillary and Mandibular Occlusal Surfaces . . . . .	20
	a. Feature Points in the Mandibular Model . . . . .	23
	b. Feature Points in the Maxillary Model . . . . .	23
	2. Point Matching Algorithm . . . . .	24
	D. Dental Alignment Using Iterative Surface-based Minimum Distance Mapping . . . . .	29
	1. The Modelling of Dental Occlusion . . . . .	31
	2. Minimization of the Distance of Occlusal Surfaces and the Algorithm . . . . .	33
	E. Validations and Results . . . . .	35
	1. Validation 1: Translational Deviations on Mesiobuccal Cusps, Central Dental Midline, and Centroid . . . . .	39
	2. Validation 2: Angular Deviations . . . . .	42
	F. Discussion . . . . .	43

CHAPTER	Page	
III	3D SEGMENTATION OF MAXILLA IN CONE-BEAM COMPUTED TOMOGRAPHY IMAGING USING BASE INVARIANT WAVELET SHAPE MODEL . . . . .	49
	A. Introduction . . . . .	49
	B. Data Acquisition and Preprocessing . . . . .	55
	C. Shape Customization and Surface Wavelet Transform . . . . .	56
	1. Training Shape Extraction and Patch Decomposition . . . . .	56
	2. Parameterization . . . . .	59
	3. 3D Landmarks Digitalization Using Catmull-Clark Subdivision . . . . .	60
	D. Wavelet Active Shape Model . . . . .	63
	1. Point Distribution Model . . . . .	63
	2. Discrete Surface Wavelet Transform Based on Catmull-Clark Subdivision . . . . .	66
	3. Wavelet Distribution Model . . . . .	72
	4. Image Feature Model . . . . .	73
	E. Base Invariant Wavelet Active Shape Model . . . . .	74
	1. Preliminary Studies . . . . .	75
	2. Customized Wavelet Base Initialization . . . . .	80
	3. Base-Invariant Wavelet Active Shape Model . . . . .	84
	F. Validations and Results . . . . .	86
	1. Data Preparation . . . . .	87
	2. Results . . . . .	91
	G. Discussion . . . . .	93
IV	REGION OF INTEREST RECONSTRUCTION AND DOSE REDUCTION ESTIMATION IN COLLIMATED CONE-BEAM COMPUTED TOMOGRAPHY IMAGING . . . . .	96
	A. Introduction . . . . .	96
	B. Materials and Methods . . . . .	97
	1. CBCT Imaging System and Collimators . . . . .	97
	2. ROI Reconstruction Using Truncation Correction . . . . .	98
	3. Analytical Reconstruction in Collimated ROI Imaging . . . . .	102
	4. Evaluation of Radiation Dose Reduction . . . . .	102
	C. Results . . . . .	106
	1. ROI Reconstruction Using Truncation Correction . . . . .	106
	2. FDK and II-line Reconstruction under Severe Truncation . . . . .	107
	3. Reduction of Radiation Dose . . . . .	110

CHAPTER	Page
D. Discussion . . . . .	112
V           CONCLUSION . . . . .	116
REFERENCES . . . . .	119
APPENDIX A . . . . .	132
APPENDIX B . . . . .	134
APPENDIX C . . . . .	135
APPENDIX D . . . . .	136
VITA . . . . .	139

## LIST OF TABLES

TABLE		Page
I	A List of Symbols Appearing in the Point Matching Algorithm . . . . .	30
II	The Parameter in the Simulation of Initial Alignment . . . . .	40
III	The Translational Deviations in the Simulation of Initial Alignment and ISMDM . . . . .	41
IV	The Angular Deviations in the Simulation of Initial Alignment and ISMDM . . . . .	43
V	List of Acronyms . . . . .	54
VI	The Computation Times in the First Experiment . . . . .	93
VII	Physical Specifications of the CBCT System. . . . .	98
VIII	Dose, Tube Voltages, and Tube Currents with Fixed $C_l = 295mm$ . . . . .	109
IX	Dose, Tube Voltages, and Tube Currents with Varying FOV . . . . .	112

## LIST OF FIGURES

FIGURE		Page
1	The flowchart of surgical planning in CMF surgery . . . . .	2
2	The flowchart of CSPS . . . . .	5
3	(a) An axial slice of CT image. (b) Mesh dataset used for 3D visualization and modeling. . . . .	7
4	Composite skull model developed by Xia <i>et al.</i> . . . . .	8
5	Cephalogram emulated using ray casting algorithm by projecting CT voxels onto the sagittal plane. . . . .	9
6	Orientation of composite skull model to NHP. . . . .	10
7	Illustration of computer-aid surgical simulation. . . . .	11
8	Surgical dental splints and templates created using our computer- aided designing/computer-aided manufacturing technique. . . . .	12
9	The overview of the procedure for digital dental occlusion. . . . .	17
10	The digital dental model scanned by laser scanner. . . . .	19
11	Illustration of dental curves . . . . .	20
12	The occlusal plane and range image of a dental model. . . . .	21
13	Illustration of cross-sectional dental model and the extracted fea- ture points. . . . .	22
14	Match of feature points. . . . .	27
15	The selection of origin and the constraints. . . . .	32
16	Two sets of partial edentulous dental models. . . . .	36
17	The <i>Cartesian</i> coordinates used for validations. . . . .	37

FIGURE	Page
18	The plots of $d_S$ (mm) versus iteration $k$ in the simulation of IS-MDM for 12 sets of the models. . . . . 38
19	Mean deviations. . . . . 42
20	A skull model reconstructed by Marching Cube Algorithm after thresholding segmentation is performed on a 3D CBCT volumetric image. . . . . 50
21	The procedure of performing segmentation in the study. . . . . 52
22	Four different skull models and the particular interest. . . . . 53
23	The procedure of generating training shapes with digitalized landmarks. 57
24	Training shape extraction and patch decomposition. . . . . 58
25	Illustration of parameterization. . . . . 60
26	Catmull-Clark subdivision. . . . . 61
27	The average operators $\bar{\mathbf{k}}_m^j$ without superscript index $j$ . . . . . 62
28	The remeshed shape with landmarks after different number of Catmull-Clark subdivisions. . . . . 63
29	The flowchart of creating WDM and IFM. . . . . 64
30	Illustration of scaling coefficients for different patch decomposition of the shape. . . . . 67
31	The decompositions in 1D DWT. . . . . 68
32	(a) One decomposition of 2D DWT using lifting steps (b) One decomposition of 2D DWT using composite lifting steps. . . . . 70
33	DSWT of Fig. 28(d) . . . . . 72
34	The image profile in IFM. . . . . 75
35	The flowchart of performing the proposed CWBI and BIWASM. . . . 76

FIGURE	Page
36	Control landmarks of a shape. . . . . 78
37	The initial shapes. . . . . 79
38	The flowchart of data preparations. . . . . 86
39	(a), (b), and (c) are mean surface distances, standard deviation of surface distances, and mean Hausdorff distances in the first set of the experiments. (d), (e), and (f) are mean surface distances, standard deviation of surface distances, and mean Hausdorff distances in the second set of the experiments. . . . . 90
40	The initial and final shapes (blue meshes) calculated by four approaches using the segmentation dataset ( $D_{17}$ ) and 18 model datasets. 92
41	ROI imaging with movable collimators. . . . . 99
42	Illustration of truncation correction. . . . . 100
43	Entrance dose calculation. . . . . 103
44	The CTDI head phantom was placed in the center of the trajectory with an ion chamber inserted alternately at the center and periphery (the solid points). . . . . 105
45	The reconstruction of "without collimation" (a), $C_t = 150\text{mm}$ , $C_l = 83\text{mm}$ (b), and $C_t = 110\text{mm}$ , $C_l = 77\text{mm}$ (c). . . . . 107
46	The images are shown in the display window . . . . . 108
47	The graph shows the entrance dosage $D$ relative to full field in % versus the $A_{FOV}$ . . . . . 109
48	Relative central and peripheral dose. . . . . 111
49	The intersection of $L_1$ with the object is entirely inside the ROI, but $L_2$ and $L_3$ are not. . . . . 114
50	An example of a rectilinear grid. . . . . 134

FIGURE		Page
51	(a) Selection of landmark points for initialization using user interaction. (b) The same user interaction but the skull shape is hidden to visualize the internal content of the slice. . . . .	135
52	Geometry of $\pi$ -line reconstruction. . . . .	137

## CHAPTER I

INTRODUCTION TO COMPUTERIZED SURGICAL PLANNING SYSTEM  
(CSPS) IN CRANIOMAXILLOFACIAL (CMF) SURGERY

The field of craniomaxillofacial (CMF) surgery involves the correction of congenital and acquired deformities of the skull and face. It includes dentofacial deformities, congenital deformities, combat injuries, post-traumatic defects, defects after tumor ablation, and deformities of the temporomandibular joint (TMJ). Due to the complex nature of the craniofacial skeleton, the surgical correction of CMF deformities is among the most challenging. These types of surgeries usually require extensive surgical planning. The success of these surgeries depends not only on the technical aspects of the operation, but to a larger extent on the formulation of a precise surgical plan. During the past 50 years, there have been significant improvements in the technical aspects of surgery (e.g., rigid fixation, resorbable materials, distraction osteogenesis, minimally invasive approaches, etc). However, the planning methods remain mostly unchanged [1–4]. At present, in CMF surgery, it is clear that many unwanted surgical outcomes are the result of deficient planning.

The advent of computed tomography (CT) and its 3D reconstruction have brought about a revolution in diagnostic radiology since cross-sectional imaging became available [5–7]. 3D rendered visualization provides a surgeon with readily recognizable images of complex anatomic structures. It can exactly record and represent the life-size and the shape of soft tissue and bone for precise surgical planning and simulation. In conjunction with appropriate computer software and hardware, computer-aided surgical simulation (CASS) has been developed and has created a number of options

---

The journal model is *IEEE Transactions on Medical Imaging*.

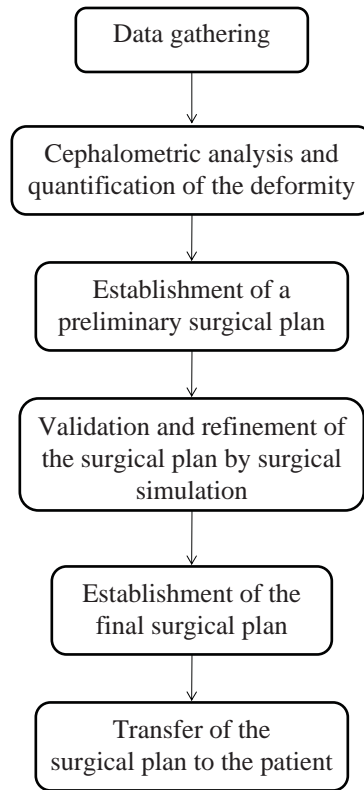


Fig. 1. The flowchart of surgical planning in CMF surgery

for CMF surgeries [3], [8–12].

In the following, the traditional surgical planning and its current bottlenecks in CMF surgeries will be first described in Section A. Next, a recently developed computerized surgical planning system (CSPS) for CMF surgery will be introduced in Section B. Although CSPS has solved most of the problems in the traditional surgical planning and has reduced surgical planning time, it still has drawbacks and creates new challenges. In Section C, three major existing drawbacks of CSPS will be briefly addressed. The proposed approaches to overcoming these drawbacks will be comprehensively described in Chapter II, III, and IV.

### A. Traditional Surgical Planning in CMF Surgery

The general procedure of traditional surgical planning in CMF surgeries is summarized in Fig. 1. The first step in planning is data gathering. Currently, data is gathered from multiple sources. The sources include the physical examination, medical photographs, plain x-rays (cephalogram and orthopantomogram), computed tomography (CT) and mounted plaster dental models. Each of these sources provides a portion of the whole data set that is needed for successful planning.

The next step is the cephalometric analysis<sup>1</sup> and quantification of the deformity. It provides diagnostic information for quantifying the deformities and changes during the treatment. The current standard is the 2D cephalometry using conventional radiography such as x-ray film. Until now, surgeons have accomplished this by utilizing a series of incomplete and unmatched data sets in a sequential manner. As an example, they first examine the patient in the natural head position (NHP)<sup>2</sup>, they then perform a cephalometric analysis with the cephalogram oriented to the Frankfort Horizontal plane, they then visualize the bony and soft tissue anatomy on a CT that has been obtained in the supine position, and finally, they evaluate the occlusion on plaster dental models that have been mounted to the Axis-Orbital plane. Therefore, at no time during the process, the surgeon is able to see the whole picture. Moreover, the use of different coordinate systems for each data set biases their observations. These problems frequently result in a flawed analysis and a flawed surgical plan.

The next step in the planning is the formulation of a preliminary surgical plan. This plan is then validated and refined during surgical simulation. The surgical simulation methods currently in use are very limited. In orthognathic surgery, surgeons

---

<sup>1</sup>Cephalometric analysis is the measurement of size, and relationships of the jaws, teeth, and cranium in the human head.

<sup>2</sup>Natural head position is the orientation of the head when a patient is standing or sitting, and his visual axis is horizontal.

simulate outcomes by performing prediction tracings and dental model surgery. Prediction tracing is done by tracing the silhouette of the facial bones from a cephalogram into a piece of acetate. These tracings are then cut and moved to evaluate possible outcomes. An obvious limitation of this technique is that it is 2D thus it is impossible to simulate 3D complex surgeries like facial asymmetries. Dental models surgery is done to establish the occlusion. A real limitation of dental model surgery is that the dental models do not depict the surrounding bones. Therefore, the surgeon is unable to visualize the effects of surgery on the facial skeleton, a really important issue. For other types of surgery (e.g. trauma, pathology and reconstruction) the current standard in surgical simulation is even more limited. Most of the time, these types of surgeries are not simulated, although skeletal surgery can be simulated on CT based physical models that are manufactured by different rapid prototyping techniques (e.g., stereolithography). Drawbacks of this method are cost and the inability to simulate different iterations of a given plan on a single model (once the model is cut, the cut cannot be undone).

Once the final surgical plan has been formulated, it needs to be transferred to the patient at the time of surgery. In cases involving the jaws, this is done by using dental splints. These splints help the surgeon place the jaws in the desired position. Currently, most surgeons make their own splints by hand, a process that is time consuming. Moreover, in cases that do not involve dentition, surgeons currently do not have an accurate method of transferring the plan to the operating room. Certain measurements taken during the planning process can be used to guide surgery but most commonly, the placement of the bones in the desired position is more an art than a science. There are reports on the use of navigation for this purpose, but this technique has not been universally adopted.

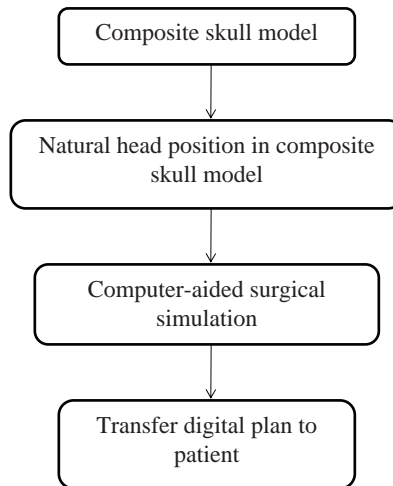


Fig. 2. The flowchart of CSPPS

## B. Computerized Surgical Planning System (CSPPS) in CMF

Because of the problems mentioned in Section A, it is evident that the current methods used to plan CMF surgery are often inadequate. In addition, it is also known that in many cases these methods produce unwanted outcomes. Moreover, the whole planning process is time consuming. An experienced surgeon frequently spends 4-6 hours to complete the surgical plan and to fabricate the splints. Finally, the cost of planning a complex case, both in time and in resources can be fairly high. The need to improve the current surgical planning methods has led surgeons to develop a 3D CSPPS. Fig. 2 shows the flowchart of the currently developed procedure of CSPPS. It will be addressed in the following subsections.

### 1. Composite Skull Model

The first step of CSPPS is the creation of a skull model. The purpose of this step is to merge all the patient's information, including 3D CT scans, digital dental models and reference planes into computer. To acquire a 3D skull image, the patient is first

scanned by CT. The 3D volumetric image is then reconstructed by CT reconstruction algorithm such as filter-backprojection algorithm [13]. The image intensity in each pixel is represented in terms of standard CT Hounsfield Unit (HU). Ideally, HU is a linear transformation of the linear attenuation coefficient and a normalized unit to represent different densities in scanned objects. Generally, the range of hard tissue in HU is above 250 HU. The skull image can be segmented by choosing a threshold near this value. This segmentation method is called threshold segmentation and has been widely used because of its simple calculation to quickly obtain the image. Since CT images can precisely display HU values of scanned objects, the threshold segmentation is applicable in CT images. After the skull images are segmented and labelled as bone images, the surface of the skull images can be calculated by Marching Cube Algorithm (MCA) [14] to obtain 3D mesh datasets. The polygonal meshes are mainly used for visualization and 3D modeling. Fig. 3 shows an axial slice of CT skull image and visualization of mesh dataset.

Although CT imaging is excellent for generating bone models, the CT does not accurately render the surfaces of teeth. Furthermore, orthodontic metal brackets and dental restorations may lead to severe streak artifacts and affect several slices which contain images of teeth in reconstructed 3D images. This is because when photons of x-rays pass through the metallic dental restorations, insufficient photons reach the detector. Fig. 3(b) illustrates the streak artifacts in the reconstructed skull model due to dental restoration. For this reason, it is still infeasible to utilize the imperfect 3D images of dental models for visualization and perform digitally reestablishing occlusion during surgical simulation. Therefore, it is necessary to develop a skull model incorporated with high quality of dental models. Gateno *et al.* [15] developed a computerized composite skull model which is created by incorporating the digital dental models into a 3D CT bone model of the skull model. The high-resolution dig-

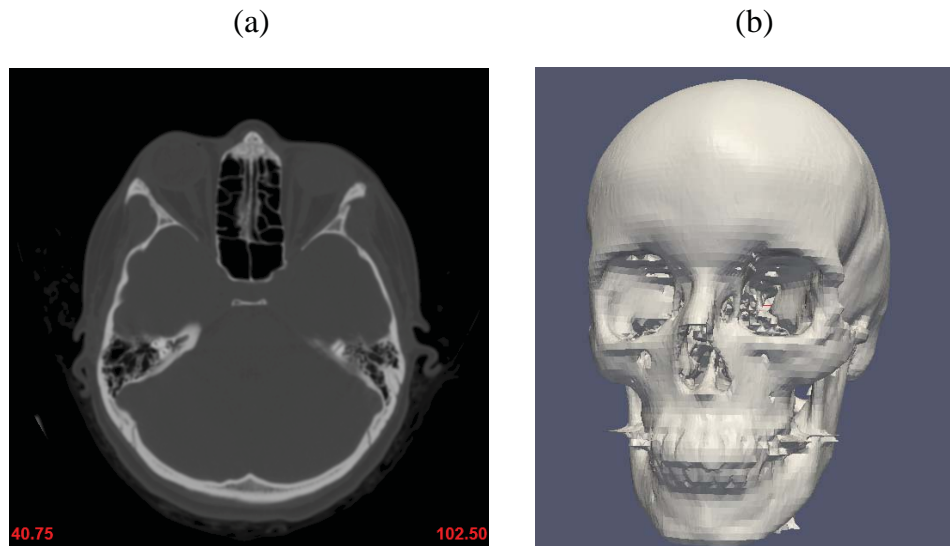


Fig. 3. (a) An axial slice of CT image. (b) Mesh dataset used for 3D visualization and modeling.

ital dental models were obtained by scanning the dental impressions using a 3D laser scanner. Swennen *et al.* [16] , [17] developed a procedure for creating an augmented virtual skull model with a detailed dental volume model acquired by a high-resolution cone-beam computed tomography (CBCT) scan of dental impressions. Those computerized composite skull models provide an artifact-free and accurate dentition feasible for CSPS. Fig. 4 (See [18]) illustrates the general procedure of creation of composite skull model.

## 2. Natural Head Position in Composite Skull Model

Establishing NHP is a vital step to provide a reference plane for cephalometric analysis and surgical planning. In CSPS, conventional radiography will be no longer required. Instead, A 2D cephalogram can be emulated by ray-casting a 3D CT image. The

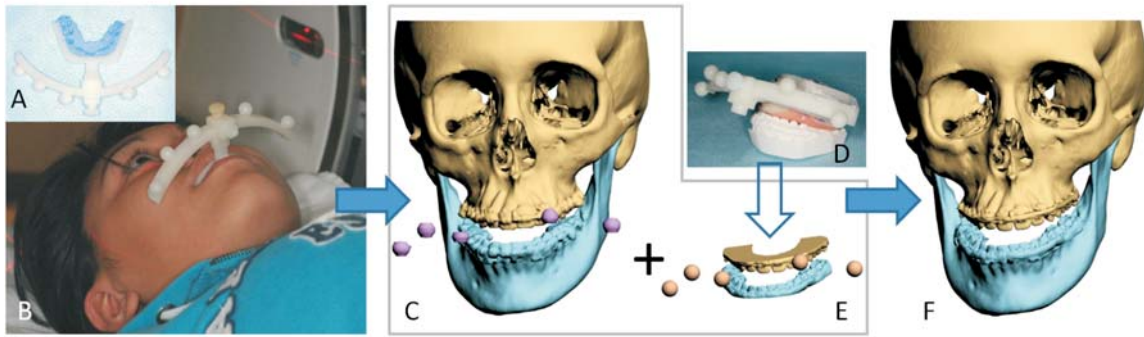


Fig. 4. Composite skull model developed by Xia *et al.*. (a) The bite jig and facebow with dental impression and fiducial markers (b) The patient biting on the bite jig and facebow during CT scan (c) The CT image of midface, mandible, and fiducial marks (d) The plaster dental models are made from dental impression. The upper and lower models and the fiducial markers are scanned by a laser scanner separately. Their positional relationship is still kept. (e) The scanned dental models and the fiducial markers. (f) By registering fiducial markers, the high quality dental models are incorporated into the skull model.

algorithm calculates the projection of a 3D CT volumetric image as if a radiograph was acquired. Fig. 5 (See [18]) shows an example of the 2D cephalogram obtained by projecting the voxels of a 3D CT model into the sagittal plane. During CT scan, the patient is in supine position, making it difficult to record NHP. Therefore, it is necessary to orient the composite skull model to NHP in the computer. Generally, NHP in the composite skull model can be defined by using standard cephalometric landmarks and intracranial planes [19]. However, because most of the patients with CMF deformities have significant asymmetries of the upper face and skull base, standard cephalometric landmarks and intracranial planes cannot be used to provide a proper reference coordinate for digitally establishing NHP of the composite skull model. It will be necessary to rely on an extracranial reference. One of the techniques to establishing NHP for composite skull model can be referred to Xia *et al.* [18] and shown in Fig. 6 (See [18]).

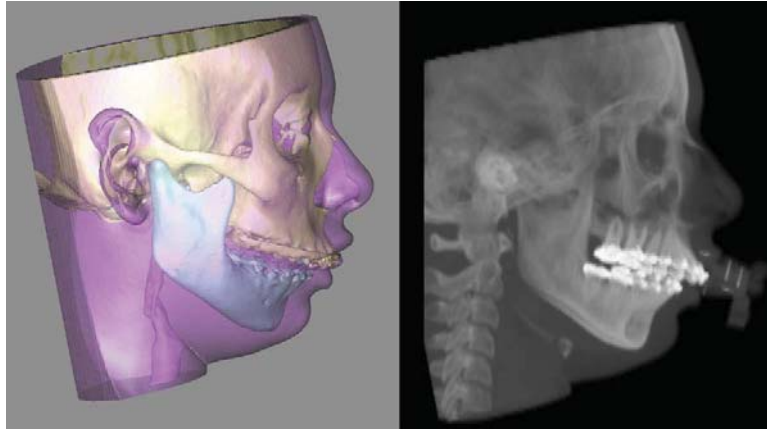


Fig. 5. Cephalogram emulated using ray casting algorithm by projecting CT voxels onto the sagittal plane.

### 3. Computer-aided Surgical Simulation (CASS)

After the composite skull model is created and the NHP is copied to the composite skull model, the surgical simulation will be performed in the computer. The surgeon will simulate any type osteotomy such Le FortI, sagittal split, maxillary and mandibular distraction. The bones can be osteotomized, moved, rotated digitally. One of the advantages of CASS is that the surgeon can perform several surgical simulations to compare the outcomes. It cannot be achieved when a physical skull model is used for surgical planning. Fig. 7 illustrates the composite skull model before and after CASS. In most of the clinical practices, the upper and lower teeth have to be occluded to achieve maximal intercuspation (MI) during performing surgical simulations. However, in the virtual world, it is difficult to align the lower jaw so that the upper and lower teeth are perfectly occluded. It is almost impossible to be certain that what is seen in the computer truly represents the best possible outcomes. Furthermore, collision detection algorithm will be required to avoid penetration of two images.

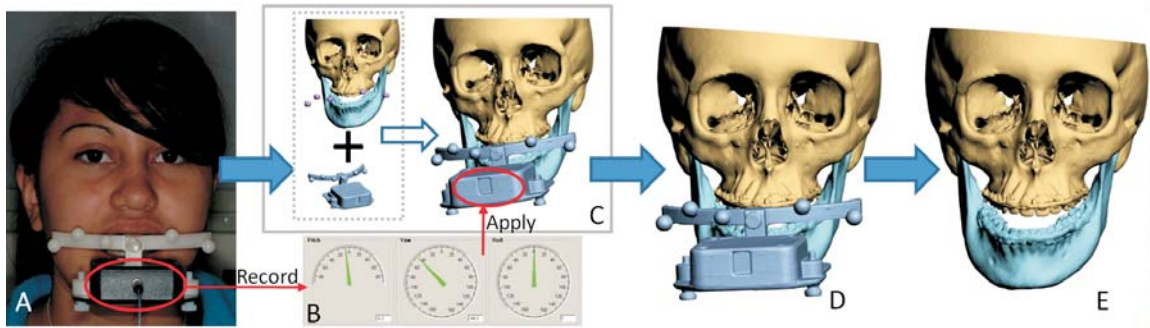


Fig. 6. Orientation of composite skull model to NHP. (a) Digital gyroscope attached to bite jig and facebow (b) Pitch, roll, and yaw of gyroscope recorded (c) Using a computer, digital replica (computer-aided design model) of gyroscope is registered to composite skull model (using fiducial markers) and the 2 objects are attached to each other. (d) Recorded pitch, roll, and yaw applied to center of gyroscope replica, reorienting composite skull model to NHP. (e) After composite skull is oriented to NHP, gyroscope replica is marked hidden.

#### 4. Transfer Digital Plan to Patient

After the surgical simulation is completed, the outcomes will be transferred to the patient at surgical. Surgical dental splints and surgical templates can be created according to the outcome of the surgical simulation. Surgical dental splints are used to reposition dentate bony segments, and surgical templates are used to reposition nondentate ones. In procedures that involve the teeth, the surgical dental splints are created by inserting a digital wafer between the maxillary and mandibular dental arches. A Boolean operation is then performed, resulting in a digital surgical splint [Fig. 8(a)<sup>3</sup>]. In procedures that do not involve the teeth, the surgical template is created to record the 3D surface geometry of the area of interest to fit the bony segment (eg, chin segment) onto the recipient bone (eg, mandibular distal segment) in a unique position [Fig. 8(b)]. Finally, the system exports the digital splints and

<sup>3</sup>Fig. 8 can be found in [18]

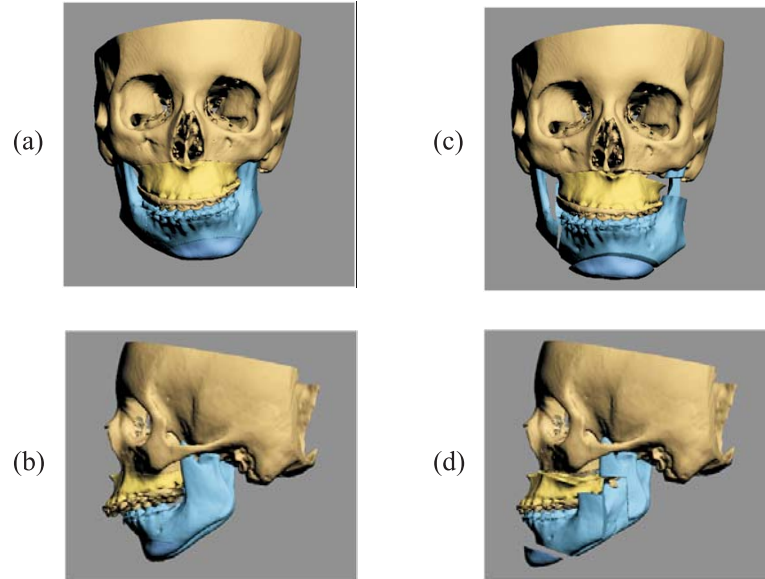


Fig. 7. Illustration of computer-aid surgical simulation. (a) and (b) are the composite skull model before performing surgical simulation. (c) and (d) illustrate the surgical simulation in the computer by successively osteotomizing, moving, and rotating bone segments.

templates in .stl format. They are then fabricated using a rapid prototyping machine and used at surgery [Fig. 8(c)-(f)].

### C. The Organization of the Dissertation

Although the CSPS has eliminated most of the problems associated with traditional planning methods, there are still challenging problems in order to improve the efficiency and feasibility of the CASS. In the following chapters, three research projects regarding solving these problems are addressed and investigated.

The first project is the reestablishment of digital dental occlusion and will be described in Chapter II. The reestablishment of dental occlusion is an essential step during CASS. However, this step is still based on traditional approaches. Surgeons still rely on the plaster dental models or manually perform 3D digital dental occlusion

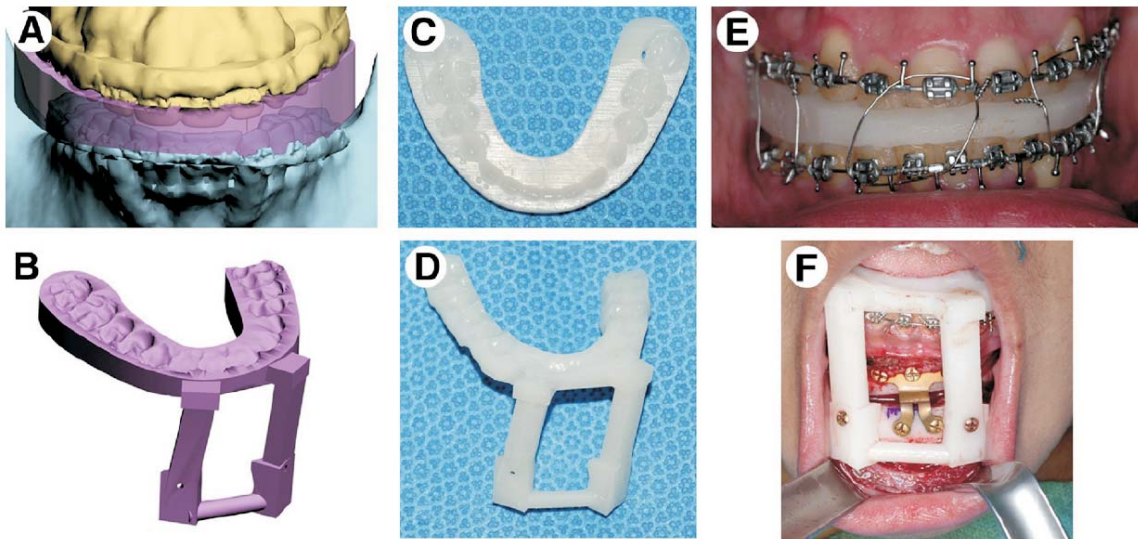


Fig. 8. Surgical dental splints and templates created using our computer-aided design-  
ing/computer-aided manufacturing technique. (a) Digital surgical splint. (b)  
Digital chin template. (b) Physical surgical splint. (d) Physical chin template.  
(e) Use of physical surgical splint at surgery. (f) Use of physical chin template  
at surgery.

in the computer. These current methods to digital establishing dental occlusion are inefficient and infeasible. A new robust and automatic algorithm for digital dental occlusion is proposed. This algorithm is designed to help surgeons achieve the MI efficiently and accurately during surgical simulation in the computer.

The second project is the segmentation in CBCT skull image and will be described in Chapter III. Currently, since the radiation dose in CT can be up to hundreds of times more than in CBCT, many studies have been discussing the possibility of replacing CT with CBCT in the field of medical imaging. It is still an open topic in the field of CSPPS for CMF surgery when the skull model is built using CBCT instead of CT. However, building a CBCT skull model is a difficult task due to the degraded image quality in CBCT. In Chapter III, a model-based segmentation for CBCT image will be proposed. An particular interest in anterior maxilla of the skull

model will be segmented by this segmentation approach. Its feasibility for CSPS will be investigated.

The third project is the technique for ROI imaging in CBCT and will be presented in Chapter IV. ROI imaging becomes popular recently due to its flexibility to a target in a patient subject. It can also reduce radiation dosage. Most of the CBCT apparatuses for the dentomaxillofacial imaging and orthodontic practices have smaller field of view (FOV) than CT since the focus for imaging is maintained on facial bones and teeth. Therefore, truncation effect becomes one of the limitations in CBCT. In Chapter IV, a study regarding designing a method for ROI imaging and radiation measurement during ROI imaging will be presented. From the results, the truncation effect can be observed. This study can help understand how this effect reduces the image quality for building a skull model in CBCT imaging. Furthermore, this study provides experiments to show the amount of radiation dose in ROI imaging can be reduced.

## CHAPTER II

## REESTABLISHMENT OF DIGITAL DENTAL OCCLUSION\*

## A. Introduction to Digital Dental Occlusion

The computer-aided surgical simulation (CASS) for craniomaxillofacial (CMF) surgery system has eliminated most of the problems associated with traditional planning methods. However, it has created a new problem because the reestablishment of the dental occlusion (i.e., maximum intercuspation (MI) position) has become more difficult and time consuming than before. Without CASS, surgeons use stone dental models to reestablish the occlusion. The physical action of aligning upper and lower dental models into MI is quick and accurate [20]. The position of MI between the dental arches can be achieved by first aligning the cusps<sup>1</sup> and grooves<sup>2</sup> of the plaster onto their ideal relationship while the models are still apart from each other, then by moving the plaster dental models towards each other until they collide, and finally by oscillating the models until the occlusion is completely seated. The visual and tactile feedback together with the cognitive insight makes dental articulation very simple. An experienced operator can complete this task in a matter of seconds.

The same is not true in the virtual world, where the dental arches are represented by two 3D images that lack collision constraints, i.e., the computer system does not stop the images from moving through each other once the model surfaces have made contact. In addition, the operator has no tactile feedback when articulating the digital dental models. Virtual articulation of an arch of 14 upper teeth (third molars are

---

\*©2010 IEEE Reprinted, with permission, from "An automatic and robust algorithm of re-establishment of digital dental occlusion" by Y. B. Chang, J. J. Xia, J. Gateno, Z. Xiong, X. Zhou, S. T. C. Wong, Sep. 2010, *IEEE Transactions on Medical Imaging*, 29(9):1652-1663.

<sup>1</sup>The small elevations on the grinding or chewing surface of a tooth.

<sup>2</sup>The valleys on the chewing surface of premolars and molars.

usually not present) against 14 lower teeth into their best possible intercuspation<sup>3</sup> is a complex task. Ideally, the 14 buccal<sup>4</sup> cusps and 4 incisal edges<sup>5</sup> of the mandibular teeth will make maximal contact against the corresponding fossae,<sup>6</sup> marginal ridges,<sup>7</sup> and lingual surfaces<sup>8</sup> of the maxillary teeth at MI position. At the same time, the palatal<sup>9</sup> cusps of the maxillary teeth also need to make contact against the fossae and marginal ridges of the lower teeth [21], [22]. Moreover, the dental midlines<sup>10</sup> should be coincidental, and the transverse relationship between the teeth should be appropriate. Finally, all of this needs to be accomplished without creating unwanted areas of overlap. Because of these difficulties, it usually takes close to an hour to achieve the "visually best possible" intercuspation in the computer. More importantly, it is almost impossible to be certain that what is seen in the computer represents the true best possible alignment. For this reason, one has not been able to rely on computerized dental alignment to treat real patients, because even a small deviation in occlusion can cause significant clinical problems. To date, one has been forced to first establish the final occlusion on physical models, scan them while in MI and then transfer this registration into CASS software. If an accurate method to automatically reestablish MI on the computer can be developed, it will result in substantial reductions in planning time and cost.

---

<sup>3</sup>The cusp-to-fossae relationship of the upper and lower posterior teeth with maximum contacting areas.

<sup>4</sup>The outer side of teeth toward the cheek.

<sup>5</sup>The cutting edges of an incisor or canine tooth.

<sup>6</sup>The valleys on the chewing surface of premolars and molars.

<sup>7</sup>An elevation of enamel that forms the proximal boundary of the occlusal surface of a tooth.

<sup>8</sup>The inner side of teeth toward the tongue (as opposed to "buccal").

<sup>9</sup>The inner side of the maxillary teeth towards the palate (as opposed to "buccal").

<sup>10</sup>The imaginary line that passes between central incisors and divides the dental model.

During digital dental articulation, collision detection/avoidance plays an essential role in solving this problem. Each manual movement in digital dental models is followed by one execution of collision detection which is a slow process used for feedback. Because of irregular surfaces of teeth, it is challenging to estimate the next movement for achieving best MI without collision. Therefore, this conventional trial-and-error alignment in the virtual world with aid of visualizing and detecting areas of collision is not practical as that in the physical world.

In this project, a solution is developed to this computerized automatic dental articulation. Fig. 9 shows the flow diagram of the approach. In Section B, the acquisition of digital dental data, the data format, and the preprocessing of the datasets will be described. In Section C, an approach of dental alignment for initially articulating the models will be addressed. A new method of searching for feature points on cusps, incisal edges, central grooves, and fossae will be developed based on the criteria of dental occlusion in Section C.1. By using those feature points, the dental models will be aligned to an initial and approximate occlusion using point matching algorithm in Section C.2. In Section D, an iterative surface-based minimum distance mapping (ISMDM) approach with occlusion constraints to complete the final alignment will be described. In Section F, the methods using 12 sets of the dental models in this project will be validated. Finally, the approach in this project will be discussed and compare it with other studies in Section G.

The notation used in this paper is described as follows. Bold symbols  $\mathbf{A}$  and  $\mathbf{a}$  are represented as a matrix and a column vector, respectively.  $\mathbf{a}^T$  defines matrix transpose of  $\mathbf{a}$ .  $\|\mathbf{a}\| \equiv \sqrt{\mathbf{a}^T \mathbf{a}}$  is the Euclidean norm of a column vector  $\mathbf{a}$ . A point  $\mathbf{a}$  by a column vector of 3-tuple  $(x, y, z)^T$  in a *Cartesian* coordinate system can be represented as  $(a_x, a_y, a_z)^T$ . The identity matrix denotes  $\mathbf{I}$ .

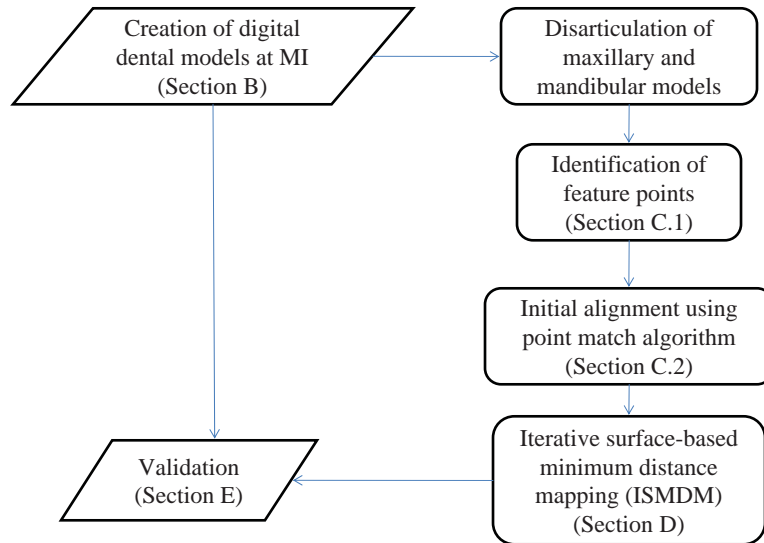


Fig. 9. The overview of the procedure for digital dental occlusion.

## B. Data Acquisition and Preprocessing

A set of stone dental models were fabricated from the original dental impressions of the patient. An experienced CMF surgeon (J. J. X.) hand-articulated the dental models to the MI position. The models were then mounted on a specially designed mounting jig to keep the maxillary and mandibular models in their MI relationship. The surfaces of the models were then scanned using a 3D laser surface scanner with an accuracy of 0.1mm by a commercially available service (GeoDigm Corp, Chanhassen, MN), resulted in a set of digital dental models that were the exact replica of their physical form at MI relationship. The dataset was saved in stereolithography (.STL) format. This scanned set of the digital dental models served as a gold standard of the occlusion at MI position in this project.

The digital dental models are closed mesh surfaces consisting of facets and vertices. The models are characterized by that each vertex is shared by its known neighboring facets, and each facet has a known normal vector going outwards from

the closed surface (toward Gouraud or Phong shading). Fig. 10(a) shows an example of a triangulated mesh surface. Although the penetration does not exist on the plaster models, the upper and lower digital dental models penetrate each other with a range of 0.08-0.35mm at the areas where the upper teeth and the lower teeth touched [Fig. 10 (b)]. This is because the surface of the model is triangulated and slightly expanded outwards.

Dental occlusion only involved the occlusal surfaces between the upper and lower teeth. Therefore, it is necessary to segment the occlusal surfaces of the teeth and discard the gums. Several approaches of teeth segmentation had already been developed to segment the entire teeth from the gums [23], [24]. However, nearly all of the patients were under orthodontic treatment prior to their orthognathic surgery. The braces and orthodontic wires were located in the middle of the buccal surfaces of the teeth. Therefore, these published methods were not applicable in this patient population. therefore, the occlusal surfaces using a commercially available software (Magics RP, Materialise, Belgium) was manually segmented.

### C. Initial Alignment

The main purpose of initial alignment is to obtain approximate dental occlusion before two dental models are finally articulated to an accurate and collision-free position and orientation. When the two dental models are initially located at an arbitrary orientation and position in a *Cartesian* coordinate system, it is necessary to estimate a transformation to bring them relatively close to each other. Two pairs of corresponding curves can be extracted from the maxillary and mandibular dental models. The two curves in each pair should be matched. In the first pair, the buccal cusps of the mandibular arch correspond to the central groove of the maxillary arch, while in the second pair, the palatal cusps of the maxillary arch correspond to the central groove

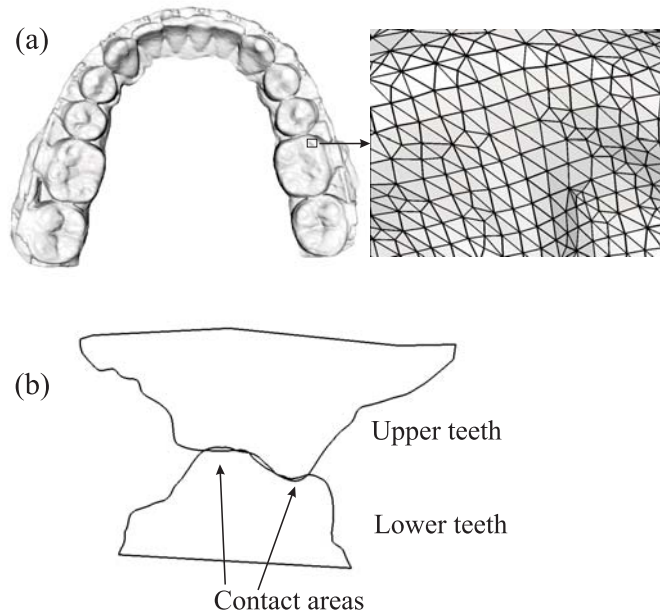


Fig. 10. The digital dental model scanned by laser scanner. (a) The surface of the digital dental model is triangulated with the enlarged view of a cusp of the molar. (b) The buccolingual cross-sectional view of upper and lower teeth obtained from the gold standard. The models penetrate each other at the contact areas due to the process of triangulation.

of the mandibular arch. Throughout this project, the first pair (Fig. 11) is used to perform initial alignment of the models. The curve of maxillary teeth [Fig. 11(a)] is extracted from maxillary fossae including the pits on incisal palatal surfaces and the central grooves of premolars and molars. The curve of mandibular teeth [Fig. 11(b)] is extracted from the incisal edges, and the buccal cusps of the premolars and molars. Ideally, the two curves should be superimposed in the MI. Those dental curves can be viewed as 3D continuous curves (not necessarily fitting polynomial curves) along the dental arches. Based on those assumptions above, an automatic approach for initially positioning the models has been developed. In the first step, feature points on the cusps, incisal edges, central grooves, pits, and fossae are identified to approximately represent the dental curves along the arches instead of finding the continuous dental

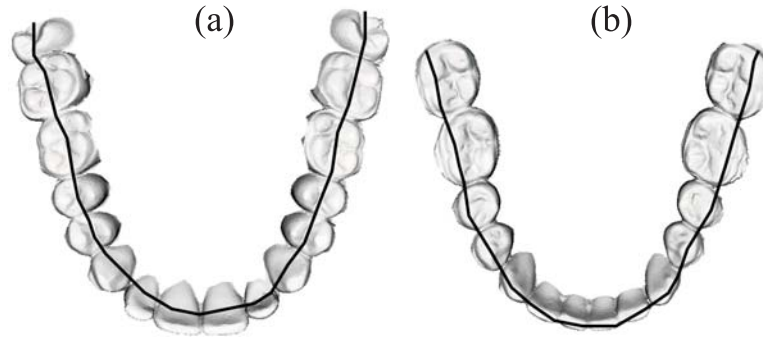


Fig. 11. Illustration of dental curves for (a) the maxillary dental model and (b) the mandibular dental model.

curves. In the second step, the dental curves of the maxillary and mandibular arches are superimposed using a point matching algorithm to complete the initial alignment.

#### 1. Identification of Feature Points on Maxillary and Mandibular Occlusal Surfaces

The occlusal plane ( $x$ - $O$ - $y$  plane) of the dental model is determined by identifying distobuccal<sup>11</sup> cusps of the first molar and the incisal edge of a central incisor<sup>12</sup> [Fig. 12(a)]. A more sophisticated generation of occlusal surface can be found in [25]. A range image (the heights of the digital model in the  $z$ -coordinate) is then calculated [Fig. 12(b)]. Based on the range image and the two-step curve fitting approach in [23], 2D dental fitting curves in the maxillary and mandibular arches are computed. These 2D fitting curves are fourth-order polynomials on the occlusal plane and fit buccal cusps and incisal edges in least square [Fig. 12(b)]. Of the note the fitting curves are 2D fitting polynomials, which are different from the dental curves defined as 3D continuous curves above in the maxillary and mandibular models. In the first step of the initial alignment algorithm, the feature points of dental models are calculated

<sup>11</sup>In dentistry, "Distal" is "situated farthest from the middle and front of the jaw".

<sup>12</sup>One of the two teeth located closest to the sagittal plane in the upper and lower jaws.

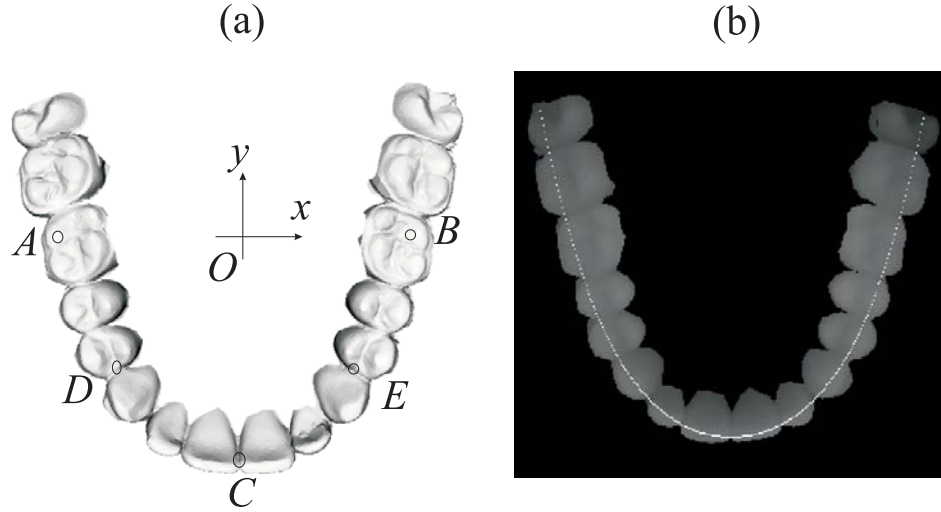


Fig. 12. The occlusal plane and range image of a dental model. (a)  $A$  and  $B$  are the points on distobuccal cusps, and  $C$  is on the cutting edge of the incisors.  $D$  and  $E$  are the points on the interstices between the canines and the first premolars. Points  $A$ ,  $B$ , and  $C$  define an occlusal plane of the model (the  $x$ - $O$ - $y$  plane). (b) The range image and the 2D dental fitting curve calculated on the  $x$ - $O$ - $y$  plane.

based on 2D fitting curves. In addition, one selects two points around the interstices<sup>13</sup> between the first premolars and canines for identifying the anterior and posterior teeth [Fig. 12(a)]. The details of feature point selection are described as follows.

The 2D fitting curves are equally sampled to obtain equal-spaced points with an interval of 1.5mm. Along the dental arches, cross-sections (in the buccolingual direction) which pass the sample points and perpendicular to the 2D fitting curve are calculated. The intersections of the cross-sections and the 3D surface of dental models are calculated. Fig. 13(a) illustrates the intersections (cross-sectional dashed curves) of the cross-sections and dental surfaces. For simplicity, the set of intersectional points at one buccolingual cross-section denotes  $\{\mathbf{s}_i\}$ , their corresponding heights are  $\{h_i\}$  in the  $z$ -coordinate, and the projections of  $\{\mathbf{s}_i\}$  onto the occlusal plane are

<sup>13</sup>A space or gap between two neighboring teeth.

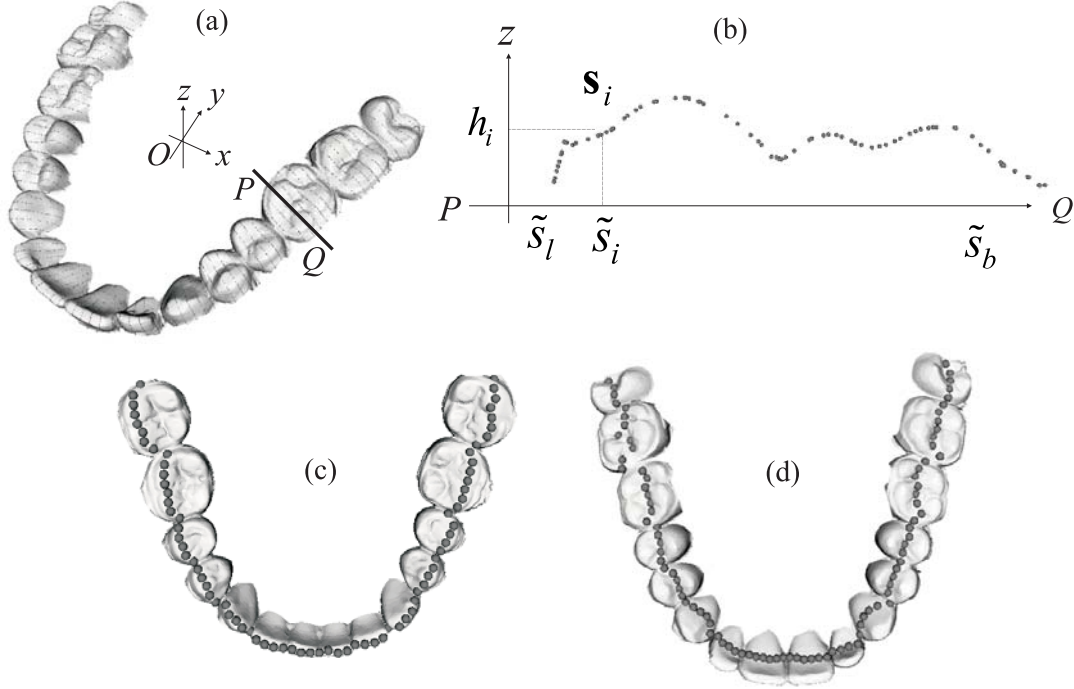


Fig. 13. Illustration of cross-sectional dental model and the extracted feature points. (a) Illustration of intersections (dashed line) of cross-sections and dental surfaces. The occlusal plane is defined by  $x$ - $O$ - $y$  plane. (b) The cross-sectional view ( $\overline{PQ}$ ) of the intersection.  $\{\tilde{s}_i\}$  is the projections of  $\{\mathbf{s}_i\}$  onto the 1D coordinate of  $\overline{PQ}$ , and  $\{h_i\}$  is the corresponding height.  $\tilde{s}_b$  and  $\tilde{s}_l$  are the most buccal and lingual values of  $\{\tilde{s}_i\}$ . (c) Feature points acquired based on cusps and incisal edges of the mandibular model. (d) Feature points acquired based on central grooves, valleys, and pits of the maxillary model.

assumed to be  $\tilde{s}_i$ . The projections  $\tilde{s}_i$  are located on a 1D coordinate which is the intersection of the buccolingual cross-section and occlusal plane. Fig. 13(b) illustrates the intersectional points and the projections in the cross-section  $\overline{PQ}$ . Assume  $\{\tilde{s}_b\}$  and  $\{\tilde{s}_l\}$  are the most buccal and lingual values of  $\{\tilde{s}_i\}$ , and  $\tilde{s}_l < \tilde{s}_b$ . Define the set  $S(\tilde{s}'_l, \tilde{s}'_b) \equiv \{i : \tilde{s}_l \leq \tilde{s}'_l < \tilde{s}_i < \tilde{s}'_b \leq \tilde{s}_b\}$ , and  $\tilde{s}_\lambda \equiv (1 - \lambda)\tilde{s}_l + \lambda\tilde{s}_b$ ,  $0 \leq \lambda \leq 1$ . The discussion will be made on how to choose the feature points on the anterior and posterior teeth in the mandibular and maxillary models, and each feature point will be selected in each set of intersectional points  $\{\mathbf{s}_i\}$ . For partial edentulous dentition, it is impossible to calculate the feature points in the missing teeth, i.e.,  $\{\mathbf{s}_i\}$  is an empty set. The missing feature points can be obtained by interpolating the neighboring feature points.

#### a. Feature Points in the Mandibular Model

The feature points on the posterior teeth are the peaks on the buccal cusps, and each of them can be identified by

$$\hat{i} = \arg \max_{i \in S(\tilde{s}_\lambda, \tilde{s}_b)} h_i \quad (2.1)$$

where one chooses  $\lambda = 0.6$  to identify buccal peaks at the buccal side of teeth. The feature points on the anterior teeth are the peaks of canines and incisors, and each of them is determined by

$$\hat{i} = \arg \max_{i \in S(\tilde{s}_l, \tilde{s}_\lambda)} h_i. \quad (2.2)$$

Fig. 13(c) shows the feature points calculated in a mandibular model.

#### b. Feature Points in the Maxillary Model

The feature points on the posterior teeth are the central grooves and valleys between the buccal and lingual peaks. Let the  $\hat{j} = \arg \max_{i \in S(\tilde{s}_l, \tilde{s}_\lambda)} h_i$  with  $\lambda = 0.4$  be the feature point on the lingual cusps. Each of feature points on the central groove can

be calculated by

$$\hat{k} = \arg \min_{i \in S(\hat{s}_j, \hat{s}_i)} h_i \quad (2.3)$$

where  $\hat{i}$  is calculated in the maxillary model using the same rule as (2.1). The maxillary anterior teeth, however, do not possess deep grooves and valleys. Instead, the lingual side of incisors and canines is characteristic of visible convex surfaces and pits. Since the bending rate on the lingual surface of anterior teeth is not large enough to detect the pits, approximate feature points of anterior teeth are calculated as follows. Let  $\bar{h}$  be the averaged height of all the feature points of posterior teeth calculated by (2.3). One chooses the feature points which are the closet to the plane  $z = \bar{h}$ :

$$\hat{k} = \arg \min_{i \in S(\hat{s}_l, \hat{s}_i)} |h_i - \bar{h}| \quad (2.4)$$

where  $\hat{i}$  is calculated in the maxillary model using the same rule as (2.2), which corresponds to peaks of anterior teeth. Finally, the feature points of anterior teeth are shifted by  $l_c$  in the lingual direction while their heights remain unchanged.  $l_c$  is 2mm for the feature point at the midline and decreased linearly in both the distal directions for the feature points of anterior teeth until  $l_c$  is 0mm for the feature points at Point  $D$  and  $E$  of Fig. 12(a) (the interstices between the canines and the first premolars). Fig. 13(d) shows the feature points calculated in a maxillary model.

## 2. Point Matching Algorithm

Let  $\{\mathbf{p}_i\}_{i=0}^{N-1}$  and  $\{\mathbf{q}_j\}_{j=0}^{K-1}$  be sets of 3D feature points of the maxillary and mandibular dental models. The two sets of points are then matched by applying a point matching approach as if the dental curves fit together when dental models are in the MI. The following point matching algorithm is based on graduated assignment combining "softassign" method [26] and a weighted least squares optimization [27]. The initial alignment becomes to find a transformation and a correspondence between the two

sets of feature points  $\{\mathbf{p}_i\}$  and  $\{\mathbf{q}_j\}$  and minimize an energy function. One calculates a rotation matrix  $\mathbf{R}$ , a translation vector  $\mathbf{t}$ , and correspondence  $[\mathbf{M}]_{ij} \equiv m_{ij}$  which minimize

$$\sum_{i=0}^{N-1} \sum_{j=0}^{K-1} m_{ij} \|\mathbf{p}_i - \mathbf{t} - \mathbf{R}\mathbf{q}_j\|^2 - \alpha \sum_{i=0}^{N-1} \sum_{j=0}^{K-1} m_{ij}$$

subject to  $\sum_{i=0}^{N-1} m_{ij} \leq 1, \forall j, \sum_{j=0}^{K-1} m_{ij} \leq 1, \forall i,$

$$m_{ij} \in \{0, 1\}, \forall i, j. \quad (2.5)$$

$\alpha$  a threshold biasing the objective function and rejecting outliers. When  $\|\mathbf{p}_i - \mathbf{t} - \mathbf{R}\mathbf{q}_j\|^2 < \alpha$ ,  $m_{ij} = 1$  is preferred to  $m_{ij} = 0$  for minimization of the objective function if all other  $m$ 's are zero in the  $i$ th row and the  $j$ th column. Hence, the pair  $\mathbf{p}_i$  and  $\mathbf{q}_j$  will not be treated as outliers with respect to each other. The graduated assignment algorithm determines the correspondence matrix  $\mathbf{M}$  and solves the transformation  $\{\mathbf{R}, \mathbf{t}\}$  in an iterative manner. After either correspondence matrix or the transformation is obtained, it can be easily used to determine the other. Given the correspondence matrix, minimization of the energy function in (2.5) becomes a weighted least square optimization.

The most challenging problem of minimizing (2.5) is to find a good correspondence matrix. To illustrate the method of point match, one consider only the equalities in the constraints of (2.5) and a square correspondence matrix. The correspondence matrix becomes a permutation matrix whose entries are either 0 or 1 and has only one 1 in each row and column. Assume constraints on the correspondence matrix with positive integer numbers are relaxed to be positive continuous real numbers. The correspondence matrix becomes a doubly stochastic matrix with all positives continuous entries and rows and columns summing to one. Based on the concept proven by Sinkhorn [28] that a doubly stochastic matrix can be obtained by

iteratively performing alternate row and column normalizations of any square matrix with all positive entries, the initial square matrix with all positive entries can be assigned as  $m_{ij} = \exp [\beta(\alpha - \|\mathbf{p}_i - \mathbf{t} - \mathbf{R}\mathbf{q}_j\|^2)]$  where  $\beta > 0$  is a control parameter. As  $\beta \rightarrow \infty$ , the exponentiation makes the maximum entry  $\max_j m_{ij}$  in a row be equal to 1 and the other entries become 0 during the process of row normalizations. The same is true to the columns. The doubly stochastic matrix obtained by Sinkhorn's iterative method will be approximately a permutation matrix if  $\beta$  is large enough. Therefore, a deterministic annealing method can be applied by increasing  $\beta$  for the sake of getting more chances of jumping out the local minima in the point matching optimization. The inequality constraints have to be considered in order to discard the outliers. By introducing positive slack variables  $m_{Nj}$  and  $m_{iK}$ , the inequalities in (2.5) can be rewritten as

$$\begin{aligned} \sum_{i=0}^N m_{ij} &\leq 1, \quad 0 \leq j \leq K - 1 \\ \sum_{j=0}^K m_{ij} &\leq 1, \quad 0 \leq i \leq N - 1. \end{aligned} \quad (2.6)$$

The correspondence matrix is unknown at the beginning of the point matching algorithm and has to be estimated appropriately based on the criteria of dental occlusion. Fig. 14(a) shows a proper situation when the point matching algorithm on these feature points is performed. The set of feature points on the arch of the mandibular model is about to match that of the maxillary model in the MI. The situations illustrated in Fig. 14(b) do not happen in real life. However, it may happen during the computation because the dental curves are relatively flat and symmetric with respect to the central incisal midline. The correspondence matrix is calculated only based on the feature points and without considering the other characteristics of the whole models. They should be prevented during the initial alignment. In order to prevent the situation of Fig. 14(b), one takes the occlusal planes of the dental models into

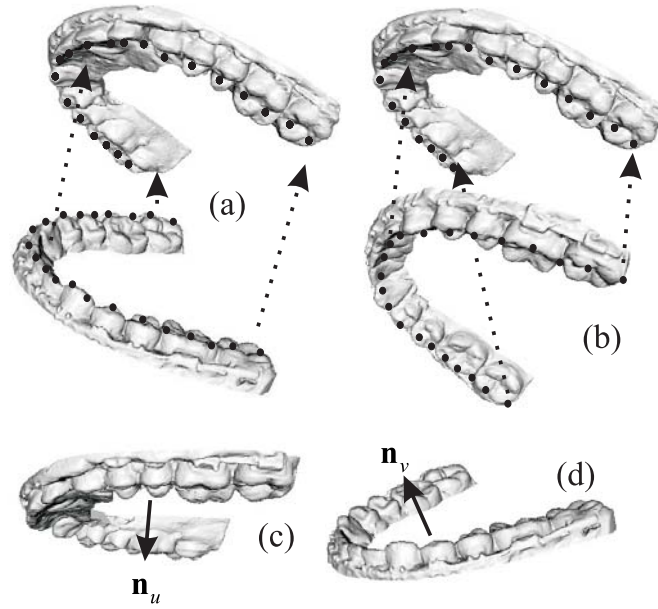


Fig. 14. Match of feature points. (a) The dental models are properly articulated when the feature points are matched. (b) The articulation is falsely made, even though the feature points of the models are matched. (c) The normal vector of the occlusal plane in the maxillary dental model. (d) The normal vector of the occlusal plane in the mandibular dental model.

account.

Let  $\mathbf{n}_u$  and  $\mathbf{n}_v$  be the unit normal vectors of occlusal planes (defined in Section C.1) of the maxillary and mandibular models, shown in Fig. 14(c) and 14(d). The directions of the normal vectors are from tooth root toward tip. When  $-1 < \mathbf{n}_u^T \mathbf{n}_v \leq 0$ , the occlusal surfaces of the dental models tend to face each other. When  $0 < \mathbf{n}_u^T \mathbf{n}_v \leq 1$ , they exhibit a tendency toward the same direction. Once the rotation matrix  $\mathbf{R}$  and translation vector  $\mathbf{t}$  are calculated during the iteration, it is more likely to have the situation of Fig. 14(b) in the following executions of the iteration if  $\mathbf{n}_u^T \mathbf{n}'_v > 0$ , where  $\mathbf{n}'_v = \mathbf{R}\mathbf{n}_v$ . Therefore, one execute the following step immediately after the transformation  $\{\mathbf{R}, \mathbf{t}\}$  is calculated each time:

$$\mathbf{n}'_v \leftarrow \mathbf{R}\mathbf{n}_v$$

**if**  $\mathbf{n}_u^T \mathbf{n}'_v > 0$  **then**

$-\mathbf{R} \leftarrow \mathbf{R}$

**end if**

---

**Algorithm 1** Point matching algorithm for initial dental alignment

---

$\mathbf{t} \leftarrow \mathbf{0}, \mathbf{R} \leftarrow \mathbf{I}$

**for**  $\beta = \beta_{ini}$  to  $\beta_{max}$  **do**

**while**  $\epsilon_0 < \epsilon'_0$  or the number of executions  $< I_0$  **do**

$m_{ij} \leftarrow \exp[\beta(\alpha - \|\mathbf{p}_i - \mathbf{t} - \mathbf{R}\mathbf{q}_j\|^2)]$

$\tilde{m}_{ij} \leftarrow m_{ij}$ ; (Initialization of  $\tilde{m}_{ij}$ )

**while**  $\epsilon_1 < \epsilon'_1$  or the number of executions  $< I_1$  **do**

$\tilde{m}_{ij} \leftarrow \frac{\tilde{m}_{ij}}{\sum_{i=0}^N \tilde{m}_{ij}}, \forall j$ ; (Row normalization)

$\tilde{m}_{ij} \leftarrow \frac{\tilde{m}_{ij}}{\sum_{j=0}^K \tilde{m}_{ij}}, \forall i$ ; (Column normalization)

**end while**

$m_{ij} \leftarrow \tilde{m}_{ij}$

        Calculate  $\mathbf{R}$  and  $\mathbf{t}$  using  $m_{ij}$

$\mathbf{n}'_v \leftarrow \mathbf{R}\mathbf{n}_v$

**if**  $\mathbf{n}_u^T \mathbf{n}'_v > 0$  **then**

$-\mathbf{R} \leftarrow \mathbf{R}$

**end if**

**end while**

$\beta \leftarrow \beta_{incr}\beta$

**end for**

---

Finally, the algorithm is summarized in **Algorithm 1**.  $\epsilon_0$  is used for convergence criterion and defined as  $\sum_{i=0}^{N-1} \sum_{j=0}^{K-1} e_{ij}$  where  $e_{ij}$  is the absolute difference between  $m_{ij}$  at the beginning and upgraded  $m_{ij}$  at the end in the outer **while** loop.  $\epsilon'_0$  is a

threshold for convergence.  $\epsilon_1$  and  $\epsilon'_1$  are in the same way and used for the convergence criterion of  $\tilde{m}_{ij}$  in the Sinkhorn’s normalization loop (the inner **while** loop).  $\beta_{incr}$  is the rate at which control parameter  $\beta$  is increased in the deterministic annealing. A list of these variables and constants are in Table I.

The sign of rotation matrix  $\mathbf{R}$  in **Algorithm 1** is changed in order to guarantee  $-1 < \mathbf{n}_u^T \mathbf{n}'_v \leq 0$ . The purpose of applying deterministic annealing is to seek a good minimum. The execution of this step may increase the chances of being trapped in local minima since the changed transformation does not minimize the objective function given the current correspondence matrix. However, these steps will no longer be executed when  $\beta \rightarrow \infty$ , i.e., the objective function starts converging. Although robustness of the algorithm is influenced by this modification, the situation of Fig. 14(b) can be prevented.

#### D. Dental Alignment Using Iterative Surface-based Minimum Distance Mapping

After the dental models are aligned to an approximate occlusion, they are finally articulated digitally using an algorithm called iterative surface-based minimum distance mapping (ISMDM). The criterion based on maximal contact of the teeth at MI is the key to develop the ISMDM. The articulation of the dental models can be modeled by consecutive executions of translation and rotation and continuous changes of rotational origin on the dental model. In order to automatically achieve maximal contact between upper and lower teeth and reach the final occlusion in the MI, one models this movement by iteratively minimizing distance of surfaces between lower and upper teeth and updating the transformation. This method is based on the idea of the iterative closest point algorithm [29] that is generally used in shape matching, registration, and alignment of two similar datasets from the same object. In addition, an important component in this method is that constraints are added to prevent

Table I. A List of Symbols Appearing in the Point Matching Algorithm

Symbol(s)	Description
$\beta$	The control parameter in deterministic annealing
$\beta_{ini}$	The initial value of the control parameter $\beta$
$\beta_{max}$	The ending value of the control parameter $\beta$
$\beta_{incr}$	The incremental rate of control parameter $\beta$
$\epsilon'_0$	The threshold allowed for each value of control parameter $\beta$
$\epsilon'_1$	The threshold allowed for row and column normalization
$\epsilon_0$	The variable in the loop for each value of control parameter $\beta$
$\epsilon_1$	The variable in the loop of row and column normalization
$I_0$	The maximum number of executions of iteration allowed for each value of control parameter $\beta$
$I_1$	The maximum number of executions of iteration allowed for row and column normalization
$\tilde{m}_{ij}$	The variable in the loop of row and column normalization

the two opposite surfaces from overlap. The detailed computational algorithms are described as follows.

### 1. The Modelling of Dental Occlusion

Let  $\{\mathbf{u}_i\}_{i=0}^{M-1}$  and  $\{\mathbf{v}_j\}_{j=0}^{J-1}$  be two sets of  $M$  and  $J$  vertices of teeth in the digital maxillary and mandibular dental models, respectively. In the following, assume the maxillary model is in a static position. The transformation is performed on the mandibular model. The transformed  $\mathbf{v}_j$  is modeled as:

$$\mathbf{v}'_j(\tilde{\mathbf{R}}, \tilde{\mathbf{t}}) \equiv \tilde{\mathbf{R}}(\mathbf{v}_j - \tilde{\mathbf{o}}) + \tilde{\mathbf{o}} + \tilde{\mathbf{t}} \quad (2.7)$$

where  $\tilde{\mathbf{o}}$  is a rotational origin (the pivot point) of the rotation matrix  $\tilde{\mathbf{R}}$ , and  $\tilde{\mathbf{t}}$  is the translation vector. Under the assumption that the two digital dental models do not overlap, maximizing contact area is equivalent to maximizing the number of contacting vertices in  $\{\mathbf{v}_j\}$ . However, not every vertex in  $\{\mathbf{v}_j\}$  will make contact when the models are in the MI. Those contact areas are even more difficult to be predicted precisely. Therefore, the distance of surfaces between lower and upper teeth is modeled as:

$$d_S \equiv \sqrt{\frac{1}{J} \sum_{j=0}^{J-1} \|\mathbf{u}_{i_j} - \mathbf{v}_j\|^2}. \quad (2.8)$$

$\mathbf{u}_{i_j}$  is a point closest to  $\mathbf{v}_j$  and is given by

$$\mathbf{u}_{i_j} = \arg \max_{\mathbf{u} \in \{\mathbf{u}_i\}} \|\mathbf{u} - \mathbf{v}_j\| \quad (2.9)$$

where  $i_j \in \{0, 1, \dots, M-1\}$ . Instead of directly maximizing contact area, one increases the chances of making contact by minimizing  $d_S$ . The rotational origin  $\tilde{\mathbf{o}}$  is given by

$$\tilde{\mathbf{o}} = \arg \min_{\mathbf{v} \in \{\mathbf{v}_j\}} \left( \min_{\mathbf{u} \in \{\mathbf{u}_i\}} \|\mathbf{u} - \mathbf{v}\| \right). \quad (2.10)$$

Fig. 15(a) shows surfaces of upper and lower teeth are closer at one side than

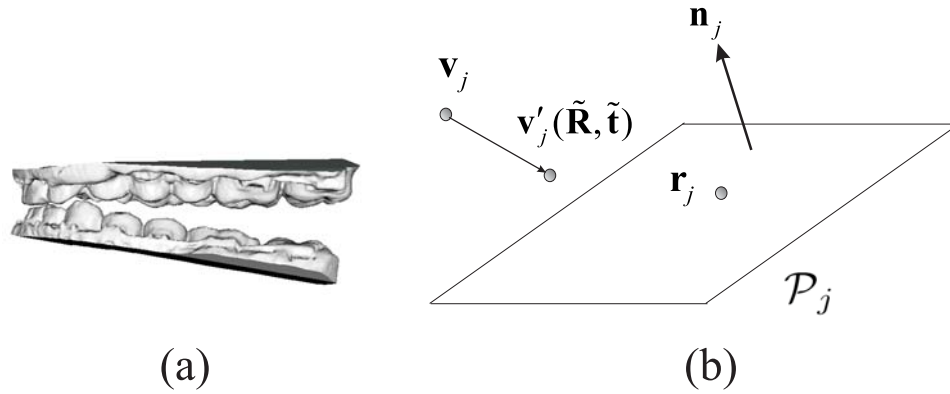


Fig. 15. The selection of origin and the constraints. (a) Surfaces of upper and lower teeth are closer at the anterior teeth than the posterior teeth. The rotational origin should be always updated and assigned near the anterior teeth of dental models in order to gain more freedom of articulation. (b) A constraint of (2.11) is a half-space defined by a plane  $\mathcal{P}_j$ . The transformed vertex  $\mathbf{v}'_j(\tilde{\mathbf{R}}, \tilde{\mathbf{t}})$  is not allowed to be in the other half-space, avoiding overlap of upper and lower teeth.

the other side. Intuitively, rotational origin will be set at the closer side so that the surface of the lower teeth at the contralateral<sup>14</sup> side can be swung closer towards the upper teeth. Because of the irregularity of teeth surfaces, dynamic change of the rotational origin by (2.10) will enable a better occlusion of lower and upper teeth surfaces.

Adding collision constraints is the most important step in digital dental occlusion. A mechanism of avoiding collision in 3D dental datasets is created. The avoidance of collision is formulated as constraints and will be incorporated into the optimization programming. Fig. 15(b) illustrates how a constraint is imposed. For each pair of points  $\mathbf{v}_j$  and  $\mathbf{u}_{i_j}$ , one creates a plane between them. Let  $\mathcal{P}_j$  be a plane with a unit normal vector  $\mathbf{n}_j$  and a point  $\mathbf{r}_j$  on it. When the transformed vertex  $\mathbf{v}'_j(\tilde{\mathbf{R}}, \tilde{\mathbf{t}})$  is not

<sup>14</sup>A term related to the opposite side.

allowed to be at the opposite side of the plane, the constraint can be expressed as

$$\left[ \mathbf{v}'_j(\tilde{\mathbf{R}}, \tilde{\mathbf{t}}) - \mathbf{r}_j \right]^T \mathbf{n}_j > 0. \quad (2.11)$$

$\mathbf{r}_j$  can be given by

$$\mathbf{r}_j = \mathbf{u}_{i_j} - \delta \mathbf{n}_j \quad (2.12)$$

where  $\delta$  is allowable penetration depth. The vertices of lower teeth are allowed to penetrate through the upper teeth surface with depth  $\delta$ . The calculation of the unit normal vector  $\mathbf{n}_j$  is demonstrated as follows. Since the datasets are triangulated surfaces, the vertex  $\mathbf{u}_{i_j}$  is shared with a number of adjacent facets. Let the unit normal vector of the  $k$ th facet sharing the vertex  $\mathbf{u}_{i_j}$  be  $\mathbf{n}_j^{(k)}$ . The  $\mathbf{n}_j$  is determined by

$$\mathbf{n}_j = \frac{\sum_k \mathbf{n}_j^{(k)}}{\|\sum_k \mathbf{n}_j^{(k)}\|} \quad (2.13)$$

which is Mean Weighted Equally computation of normal. Since most of the areas between upper and lower teeth will never make contact during the MI, a large number of constraints added to the algorithm may be redundant. In order to reduce the number of constraints, it is not necessary to add a constraint to a point pair  $\mathbf{v}_j$  and  $\mathbf{u}_{i_j}$  if the distance between them is beyond a threshold  $\rho$

## 2. Minimization of the Distance of Occlusal Surfaces and the Algorithm

Given a rotational origin  $\tilde{\mathbf{o}}$ , one calculates the rotation matrix  $\tilde{\mathbf{R}}$  and the translation vector  $\tilde{\mathbf{t}}$  which minimize

$$d_S^2(\tilde{\mathbf{R}}, \tilde{\mathbf{t}}) \equiv \frac{1}{J} \sum_{j=0}^{J-1} \|\mathbf{u}_{i_j} - \mathbf{v}'_j(\tilde{\mathbf{R}}, \tilde{\mathbf{t}})\|^2$$

subject to  $\left[ \mathbf{v}'_j(\tilde{\mathbf{R}}, \tilde{\mathbf{t}}) - \mathbf{r}_j \right]^T \mathbf{n}_j > 0.$  (2.14)

The rotation matrix consists of non-linear terms which can be linearized by small-angle approximation [30], [31]. When the two dental models are getting occluded, the increment needed to seat the dental occlusion will gradually become smaller. Therefore, errors caused by this approximation will become less significant. Approximate the rotational matrix  $\tilde{\mathbf{R}}$  by linearizing it as

$$\tilde{\mathbf{R}} = \begin{pmatrix} 1 & -\theta_z & -\theta_y \\ \theta_z & 1 & -\theta_x \\ \theta_y & \theta_x & 1 \end{pmatrix} \quad (2.15)$$

where  $\theta_x$ ,  $\theta_y$ , and  $\theta_z$  are rotational angles with respect to  $x$ -,  $y$ -, and  $z$ -axes. Define  $\theta = (\theta_x, \theta_y, \theta_z)^T$  and  $\mathbf{L}_j$  as

$$\mathbf{L}_j = \begin{pmatrix} 0 & -v_{j,z} + \tilde{o}_z & -v_{j,y} + \tilde{o}_y \\ -v_{j,z} + \tilde{o}_z & 0 & v_{j,x} - \tilde{o}_x \\ v_{j,y} - \tilde{o}_y & v_{j,x} - \tilde{o}_x & 0 \end{pmatrix}. \quad (2.16)$$

$(\tilde{\mathbf{R}} - \mathbf{I})(\mathbf{v}_j - \tilde{\mathbf{o}})$  can be rewritten as

$$(\tilde{\mathbf{R}} - \mathbf{I})(\mathbf{v}_j - \tilde{\mathbf{o}}) = \mathbf{L}_j \theta. \quad (2.17)$$

The objective function in (2.14) becomes

$$d_S^2(\tilde{\mathbf{R}}, \tilde{\mathbf{t}}) = \frac{1}{J} \sum_{j=0}^{J-1} \|\mathbf{L}_j \theta + \tilde{\mathbf{t}} + \mathbf{b}_j\|^2 \quad (2.18)$$

where  $\mathbf{b}_j = \mathbf{v}_j - \mathbf{u}_{i_j}$ . Let  $\mathbf{x} \equiv (\tilde{\mathbf{t}}^T, \theta^T) = (\tilde{t}_x, \tilde{t}_y, \tilde{t}_z, \theta_x, \theta_y, \theta_z)^T$  and  $\tilde{\mathbf{L}}_j \equiv [\mathbf{L}_j \ \mathbf{I}]$ .

Equation (2.18) becomes (without the scaling  $\frac{1}{J}$ )

$$\mathbf{x}^T \left( \sum_{j=0}^{J-1} \tilde{\mathbf{L}}_j^T \tilde{\mathbf{L}}_j \right) \mathbf{x} + 2 \left( \sum_{j=0}^{J-1} \mathbf{b}_j^T \tilde{\mathbf{L}}_j \right) \mathbf{x} + \sum_{j=0}^{J-1} \|\mathbf{b}_j\|^2. \quad (2.19)$$

With the linearization of rotation matrix, the objective function  $d_S^2$  becomes a quadratic form, and (2.11) becomes a linear constraint. The minimization of (2.14) can be solved by quadratic programming. The algorithm is summarized in **Algorithm 2**.  $S$  the total number of executions in the iteration.  $\rho$  is the threshold for limiting the number

of linear constraints.

---

**Algorithm 2** ISMDM algorithm

---

```

for  $k = 0$  to  $S - 1$  do
  for  $j = 0$  to  $J - 1$  do
     $\mathbf{u}_{i_j} \leftarrow \arg \max_{\mathbf{u} \in \{\mathbf{u}_i\}} \|\mathbf{u} - \mathbf{v}_j\|$ 
  end for
   $\tilde{\mathbf{o}} \leftarrow \arg \min_{\mathbf{v} \in \{\mathbf{v}_j\}} (\min_{\mathbf{u} \in \{\mathbf{u}_i\}} \|\mathbf{u} - \mathbf{v}\|)$ 
  for  $j = 0$  to  $J - 1$  do
    if  $\|\mathbf{u}_{i_j} - \mathbf{v}_j\| < \rho$  then
      Add the linear constraint  $\left[ \mathbf{v}'_j(\tilde{\mathbf{R}}, \tilde{\mathbf{t}}) - \mathbf{r}_j \right]^T \mathbf{n}_j > 0$ 
    end if
  end for
  Minimize (2.14) by quadratic programming
  Update  $\mathbf{v}_j$  using (2.7)
end for

```

---

## E. Validations and Results

12 sets of the digital dental models are used in the simulation. They are randomly selected from the clinical archive database using a random number table. The selection criteria include:

1. No early contact;
2. The patients underwent a single-piece maxillary surgery;
3. The models have a stable occlusion.

All the dental models have relatively normal dentition except two pairs of dental models are partial edentulous (Fig. 16) and two pairs of models have first premolar

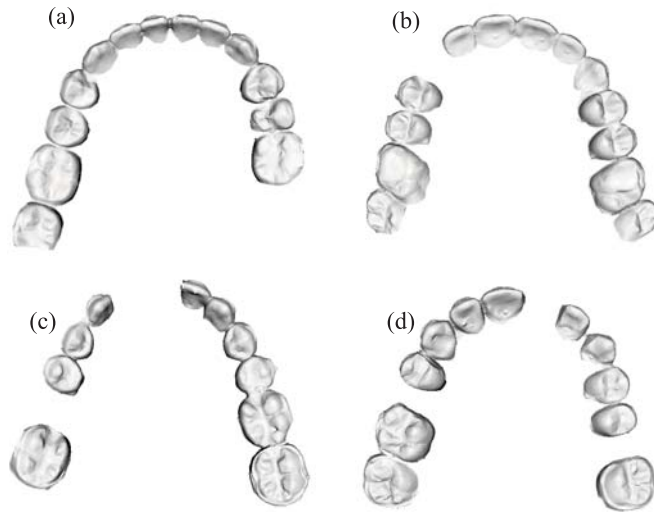


Fig. 16. Two sets of partial edentulous dental models. (a) and (b) are the first set of the mandibular and maxillary models, and (c) and (d) are the second set of the mandibular and maxillary models.

extractions for orthodontic treatment. The occlusion at the MI is established by an experienced CMF surgeon (J. J. X.). The models are scanned at MI position using a laser scanner as a part of the clinical routine (described in Section B). The surface datasets of the maxillary and mandibular models are saved in .STL format with a resolution of 0.1mm. In this simulation, they are decimated to a resolution of 0.2mm. The teeth, which are involved in occlusion, are segmented from the rest of the model. These originally scanned digital models at MI position serve as a control group during the validation processes.

The origin  $O$  of the *Cartesian* coordinate system is the centroid of the boundary box of the mandibular model in the control group [Fig. 17(a)], which is determined by the maximum and minimum of the range in the  $x$ - (mediolaterally),  $y$ - (antero-posteriorly) and  $z$ - (superoinferiorly) directions. Three landmarks that are commonly used in clinical practice are selected on the occlusal surface on the mandibular model.

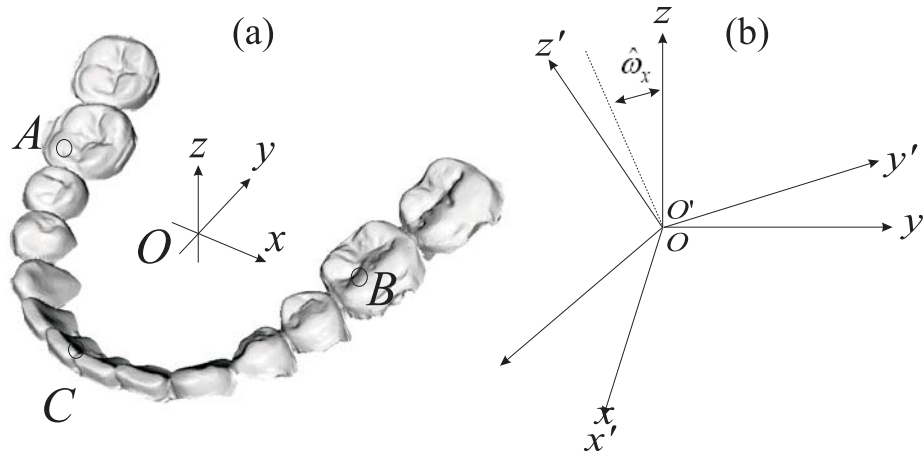


Fig. 17. The *Cartesian* coordinates used for validations. (a) The *Cartesian* coordinate system is defined to represent the sagittal, coronal, and axial planes in the control model. The results are validated in Section F.1 at mesiobuccal cusps (Point *A* and *B*) of the first molar, the mandibular central dental midline (Point *C*), and the centroid (Point *O*) in the control model. (b) In Section F.2, the sagittal angular deviation  $\hat{\omega}_x$  is defined by the angle between the dashed line and the *z*-axis. The dashed line is calculated by projecting the *z'*-axis onto the *y*-*O*-*z* plane.

They are the mesiobuccal<sup>15</sup> cusp of the first right molar (*A*), the mesiobuccal cusp of the first left molar (*B*), and the central dental midline (*C*). The coordinates of these landmarks are used later to compare with the same landmarks in the experimental group.

In order to test the proposed approach, it is necessary to first disrupt this relationship because the maxillary and mandibular digital dental models are scanned in MI. To this end, one first duplicates the scanned mandibular teeth model and its landmarks, and then systematically generate rigid transformations to disarticulate the mandibular teeth model while the maxillary teeth model is kept constant. A total of 80 disarticulations are generated in each set of the models by choosing five

<sup>15</sup>”Mesial” is opposite to ”distal.”

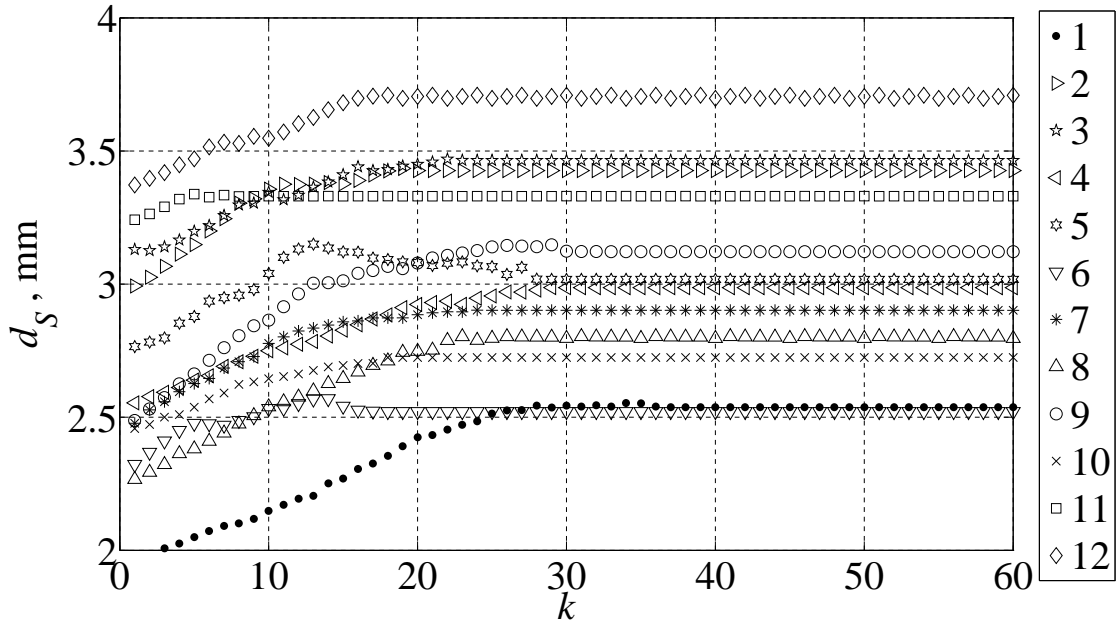


Fig. 18. The plots of  $d_S$  (mm) versus iteration  $k$  in the simulation of ISMDM for 12 sets of the models. The initial positions of the mandibular models for ISMDM algorithm is calculated as follows: the mandibular models are disarticulated from gold standard using rotational axis  $\left(-\frac{\sqrt{2}}{2}, \frac{\sqrt{2}}{2}, 0\right)$ , rotational angle  $\theta$ , and translation  $(-20\text{mm}, -20\text{mm}, -10\text{mm})$  and then aligned by initial alignment algorithm.

rotational matrices and 16 translations of rigid transformation. The rotational origin corresponds to the centroid of the mandibular teeth model. Among five rotational matrices, one rotation matrix is identity, and the other four rotation matrices are calculated by choosing a normalized rotational axis and a rotational angle. Two normalized rotational axes are  $\left(\frac{\sqrt{2}}{2}, \frac{\sqrt{2}}{2}, 0\right)$  and  $\left(-\frac{\sqrt{2}}{2}, \frac{\sqrt{2}}{2}, 0\right)$ . Two rotational angles of  $-\frac{1}{3}\pi$  and  $\frac{1}{3}\pi$  are applied with respect to each of the rotational axes. The translation in  $z$ -coordinate is chosen as  $-10\text{mm}$  to vertically disarticulate the mandibular model (separate the mandibular model apart from the maxillary model). Then, the translations in  $x$ - and  $y$ - coordinate are incrementally chosen from  $-20\text{mm}$ ,  $-7\text{mm}$ ,  $7\text{mm}$ , to  $20\text{mm}$ . These systematically disarticulated models are enough to represent a pa-

tient's malocclusion caused by CMF deformities. These disarticulated models serve as an experimental group. The landmarks  $A$ ,  $B$  and  $C$ , and the centroid  $O$  and the  $x$ -,  $y$ -, and  $z$ -coordinates in the control model become  $A'$ ,  $B'$  and  $C'$ , and the centroid  $O'$  and the  $x'$ -,  $y'$ -, and  $z'$ -coordinates in the experimental model.

Once the models are systematically disarticulated, the maxillary and mandibular models in the experimental group are initially articulated using the proposed initial alignment algorithm described in Section C. The parameters used in point matching algorithm are summarized in Table II. They are then finally aligned using the ISMDM algorithm described in Section D. The following parameters are applied in the ISMDM algorithm:  $S = 60$ ,  $\rho = 0.2\text{mm}$ , and  $\delta = 0.1\text{mm}$ . Fig. 18 shows an example of the plots of average distance of surface  $d_S$  versus iteration  $k$  for 12 sets of the models in the simulation of the ISMDM algorithm selected from 80 repeated experiments. During the validation process, the maxillary model remains static while the mandibular model seeks its MI position. Finally, validation is completed by calculating the translational and rotational deviations of the mandibular models between the control and the experimental groups. Based on the clinical experience and published literature [32], there would be no clinical significance if the translational deviation of the mandibular models between the control the experimental groups is less than 0.5mm and the angular deviation is less than  $1^\circ$  on sagittal, coronal, and axial planes respectively.

#### 1. Validation 1: Translational Deviations on Mesiobuccal Cusps, Central Dental Midline, and Centroid

In the first validation, one computes the translational deviations (deltas) of the articulated experimental models relative to the control model at the landmarks of mesiobuccal cusps of the first molar, the central dental midline, and the centroid in  $x$ -,  $y$ -, and

Table II. The Parameter in the Simulation of Initial Alignment

$\epsilon'_0$	$\epsilon'_1$	$\beta_{ini}$	$\beta_{max}$	$\beta_{incr}$	$I_0$	$I_1$	$\alpha$
0.5	0.05	0.009	50	1.2	30	7	2

$z$ -axis. It generates a total of 11,520 sets of deltas, 960 for each pair of the models. The data is first screened and its distribution is normally shaped. In each pair of the models, then the 80 repeated deltas resulted from 80 systematic disarticulations for a given landmark at a given direction are averaged. Furthermore, Analysis of Variance (ANOVA) for repeated measures is used to detect whether the delta is statistically different from "0", a hypothetical ideal number of the delta. It is also used to detect whether there is a statistically significant difference among the three directions ( $x$ -,  $y$ -, and  $z$ -), and the four landmarks [( $A'$ ,  $A$ ), ( $B'$ ,  $B$ ), ( $C'$ ,  $C$ ), and ( $O'$ ,  $O$ )] in final results calculated by the ISMDM algorithm. The result shows the delta is not statistically significantly diverged from "0" [F(1,11)=2.58, P=0.14] in Fig. 19(a). The results also show there is no statistically significant difference among three directions [F(2,22)=0.77, P=0.48], or four landmarks [F(3,33)=0.13, P=0.94]. Finally, the mean translational deltas, the standard deviations (SDs) and the 95% of confidence intervals (CIs) for the results calculated by the initial alignment algorithm ("Initial alignment") and for the final results calculated by the ISMDM algorithm ("ISMDM") are presented in Table III. They indicate that the models are articulated successfully with a small degree of translational deviation.

Table III. The Translational Deviations in the Simulation of Initial Alignment and ISMDM

		Initial alignment			ISMDM		
		Mean	SD	95% of CI	Mean	SD	95% of CI
	$x$	-0.068	0.536	(-0.409 , 0.272)	-0.086	0.318	(-0.288 , 0.116)
$(A', A)$	$y$	0.548	1.224	(-0.230 , 1.325)	-0.144	0.636	(-0.548 , 0.260)
	$z$	1.436	0.682	(1.002 , 1.870)	-0.065	0.169	(-0.172 , 0.042)
	$x$	-0.128	0.539	(-0.471 , 0.214)	-0.098	0.327	(-0.306 , 0.110)
$(B', B)$	$y$	0.535	0.979	(-0.087 , 1.157)	-0.131	0.440	(-0.410 , 0.149)
	$z$	1.443	0.538	(1.101 , 1.786)	0.003	0.100	(-0.060 , 0.065)
	$x$	-0.116	0.747	(-0.951 , 0.358)	-0.090	0.378	(-0.331, 0.150)
$(C', C)$	$y$	0.583	0.681	(0.150 , 1.015)	-0.130	0.220	(-0.269 , 0.010)
	$z$	0.334	0.697	(-0.108 , 0.777)	-0.108	0.332	(-0.320 , 0.103)
	$x$	-0.087	0.387	(-0.333 , 0.159)	-0.082	0.225	(-0.226 , 0.060)
$(O', O)$	$y$	0.626	0.637	(0.221 , 1.031)	-0.132	0.180	(-0.246 , -0.018)
	$z$	1.175	0.429	(0.902 , 1.447)	-0.050	0.105	( -0.114 , 0.020)

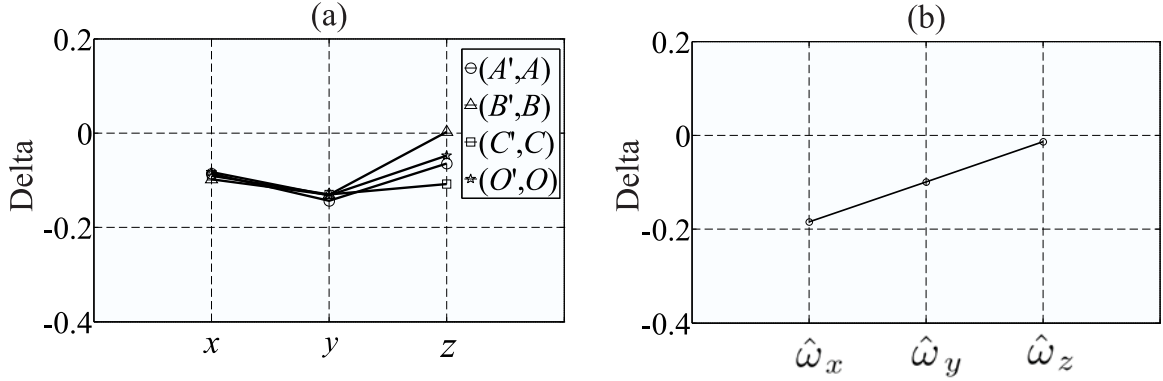


Fig. 19. Mean deviations. (a) Mean translational deviations (deltas) for each landmark between the experimental and control groups in  $x$ -,  $y$ -, and  $z$ -directions. (b) Mean rotational deviations (deltas) between the experimental and control groups in angular deviations  $\hat{\omega}_x$ ,  $\hat{\omega}_y$ , and  $\hat{\omega}_z$ .

## 2. Validation 2: Angular Deviations

In the second validation, angular deviations are computed in view of sagittal ( $y$ - $O$ - $z$  plane), coronal ( $x$ - $O$ - $z$  plane), and axial planes ( $x$ - $O$ - $y$  plane) of the control model. The experimental models are moved translationally so that the centroid  $O'$  is matched to the centroid  $O$  in the control group. The sagittally angular deviation is then calculated as follows.  $z'$ -axis is projected onto the  $y$ - $O$ - $z$  plane. One defines an angular deviation  $\hat{\omega}_x$  by calculating the angle between the projected  $z'$ -axis and the  $z$ -axis. Fig. 17(b) illustrates the projected  $z'$ -axis (the dashed line) and a sagittal angular deviation  $\hat{\omega}_x$ . Similarly, one projects the  $z'$ -axis onto the  $x$ - $O$ - $z$  plane, and the coronal angular deviation  $\hat{\omega}_y$  is determined by the angle between the projected  $z'$ -axis and  $z$ -axis. By projecting the  $y'$ -axis onto the  $x$ - $O$ - $y$  plane, the axial angular deviation  $\hat{\omega}_z$  is defined by the angle between the projected  $y'$ -axis and  $y$ -axis. It generates a total of 2,880 sets of deltas, 240 for each pair of the models. The data is first screened and its distribution is normally shaped. In each pair of the models, one then averages the 80 repeated deltas resulted from 80 systematic disarticulations for

Table IV. The Angular Deviations in the Simulation of Initial Alignment and ISMDM

	Initial alignment			ISMDM		
	Mean	SD	95% of CI	Mean	SD	95% of CI
$\hat{\omega}_x$	-2.324	2.13	(-3.677 , -0.971)	-0.185	0.792	(-0.688 , 0.319)
$\hat{\omega}_y$	0.006	0.474	(-0.295 , 0.307)	-0.100	0.162	(-0.203 , 0.004)
$\hat{\omega}_z$	0.022	2.112	(-1.319 , 1.364)	-0.014	1.234	(-0.799 , 0.77)

a given landmark at a given direction. Furthermore, ANOVA for repeated measures is used to detect whether the delta is statistically different from "0", a hypothetical ideal number of the delta. It is also used to detected whether there is a statistically significant difference among the three directions ( $\hat{\omega}_x$ ,  $\hat{\omega}_y$ , and  $\hat{\omega}_z$ ) in final results calculated by the ISMDM algorithm. The results show the delta is not statistically significantly diverged from "0" [F(1,11)=0.32, P=0.58] in Fig. 19(b). The results also show there is no statistically significantly difference among the three directions [F(2,22)=0.16, P=0.84]. Finally, the mean angular deltas, the SDs and the 95% of CIs for the results calculated by the initial alignment algorithm ("Initial alignment") and for the final results calculated by the ISMDM algorithm ("ISMDM") are presented in Table IV. They also indicate that the models are articulated successfully with a small degree of rotational deviation.

## F. Discussion

An automatic and robust approach to digitally articulating dental models has been developed. This approach consists of two major steps. The first step is the initial

alignment, in which the point match algorithm is used to match the feature points of dental curves in order to bring the models relatively close to each other. The second step is the final alignment, in which one develops the ISMDM algorithm to minimize the average distance of surfaces of the models in order to articulate the maxillary and mandibular models to the MI without overlapping each other. This approach has been validated using 12 pairs of the dental models. The results of validation shows the models are successfully articulated with a small degree of deviation. The accurate results can be attributed to the intuitive assumption that maximizing contact areas of upper and lower teeth is equivalent to minimizing the average distance defined in (2.8).

The results of the validation show the robustness of the proposed approach. First, the initial alignment algorithm can bring the models to proper positions even before performing the ISMDM. Shown in Tables III and IV, the models aligned by the initial alignment algorithm are close enough to successfully complete final articulation by the ISMDM. Second, each mandibular model is docked to a final occlusion since the average distance of surface  $d_S$  converges at  $k < 30$  (illustrated in Fig. 18) using ISMDM algorithm. Shown in Tables III and IV, the deviations are small enough to satisfy clinical requirements. They demonstrate the feasibility of the proposed approach towards fully automatic digital dental articulation. In addition, the proposed validation includes the models with special conditions: partial edentulous dentition and first premolar extraction due to orthodontic treatment. One initially expects these models may result in a larger deviation. However, even with the models with special conditions, the models in experimental group still achieve a same small degree of deviation. This further proves the robustness of the proposed approach. Of the note a small portion of results of the  $y$ -axis (under "ISMDM" in Table III) shows the standard deviations of Point  $A$  and  $B$  are slightly larger (close to 0.5mm) than

the others. This contributes to a larger range of angular deviation  $\hat{\omega}_z$  on the axial plane (under "ISMDM" in Table IV). During the dental articulation, the mandibular models have more rotational freedom on the axial plane in comparison to the sagittal and coronal planes. A possible solution to reduce the rotational freedom on the axial plane is to add more constraints, i.e., coincidence between maxillary and mandibular dental midlines.

The proposed initial alignment algorithm plays an important role in reducing the number of executions of nearest point searching of ISMDM. The high-quality dataset of digital dental models may drastically increase the computational time in ISMDM since the calculation of nearest point searching is tremendous. The initial alignment algorithm is designed to bring the high-resolution digital dental models used in clinic to an approximate MI position and orientation, without considering whether there is a collision between the upper and the lower teeth. The advantage of using initial alignment is to tremendously increase the computational speed of convergence in final alignment using ISMDM algorithm and significantly reduce the computational time in planning the CMF surgeries. As illustrated in Fig. 18, all the models can be quickly articulated in only 30 executions of iteration in ISMDM without intensively searching for the position at MI. In the simulation, the computational time of both initial alignment algorithm and the ISMDM for each set of the models is only several minutes.

The final alignment is to bring the dental models from the position achieved by initial alignment to their final occlusion at the MI and free of collision using the ISMDM algorithm. In this algorithm, the convergence in average distance of surface between the models can be used to decide whether the models have been articulated. The correspondence of vertices in upper and lower teeth and linear constraints are dynamically updated in each iteration, resulting in different parameters of quadratic

programming in (2.19). In this algorithm, the optimal transformation is solved by quadratic programming in each iteration. When the maxillary and mandibular models are getting closer to be articulated, the optimal transformation approximates a null since these linear constraints prevent the models from overlap and stop the models. Once this is achieved, the null transformation will not further update the correspondence and constraints in following iterations. Thus, the average distance will converge.

The final alignment should be completed without overlapping between the upper and the lower models. Another advantage of the ISMDM algorithm is that it has successfully overcome the notorious problem of uncontrollable overlap by applying linear constraints and allowable penetration depth  $\delta$ . Each of the constraints is determined by one vertex in the upper teeth and its corresponding vertex in the lower teeth. Therefore, the number of constraints depends on the parameter  $\rho$  and resolution of datasets. However, the models may not be able to entirely articulate if too many constraints are incorporated in quadratic programming. It is observed that an appropriate value of the parameter  $\rho$  is approximate to the resolution of dataset. Theoretically, the penetration depth is zero, leading to no overlap of upper and lower teeth. However, since the surfaces of the digital models are slightly expanded outward [Fig 10(b)] due to the process of triangulation, the articulated digital models must have little overlap at the contact areas. Therefore, the choice of the allowable penetration depth relies on the extent of overlap in the dataset. In this experiment, one sets the penetration depth was 0.1mm.

Finally, the approach is different from others. The ultimate goal of the approach is to digitally articulate dental models for patient treatment. Hiew *et al.* [32] used the right and posterior surfaces of the model bases to perform the dental model alignment. They first trimmed the right and posterior surfaces of the upper and lower

plaster model bases so they would be perfectly in the same plane with the teeth in the correct occlusion. After the models were separately digitized, the centroids and normal vectors of these surfaces were calculated by using a  $K$ -means plane detection algorithm. This initial step was to align the digital models in anteroposterior ( $y$ -axis) and transverse ( $x$ -axis) directions. The final alignment was then completed by adjusting one of the models in superoinferior ( $z$ -axis) direction. Finally, the vertical alignment was optimized by collision detection, and the transformation was applied to the lower model. However, this approach is not designed based on the occlusal criteria. Thus it is impossible to incorporate their method into the actual surgical planning procedure clinically. Zhang *et al.* [33] designed a two-stage occlusal analysis algorithm. In the first stage, each vertex of the teeth models is checked whether it is considered as a penetration. In the second stage, the distance of each vertex to the opposing model was calculated, and the color ranges of distance were shown on the 3D teeth models. The color ranges are useful for manual alignment in the computer, but it still needs iterative process of collision detection and manual transformation of the models. Finally, DeLong *et al.* [34] utilized a "3-point alignment" method. Three pairs of contacting points on both the upper and lower teeth models were initially identified on the plaster models and then digitized onto the digital models. The points on the lower teeth were aligned using a fitting algorithm to the points on the upper teeth model, and the transformation was applied to the lower model. The established occlusion was then visually checked, and the 3-point alignment method was repeated by selecting different pairs of points until the visual outcome was satisfactory and overlap of the models is free. One had independently developed and tested this method before DeLong *et al.* published their results. Although this method could bring the upper and lower teeth close to MI, it is almost impossible to be certain that what is seen in the computer truly represents the best possible alignment. Since

even a small deviation in the occlusion causes a significant clinical problem, this 3-point alignment may be used as an initial alignment but one should not rely on this method of dental alignment to treat real patients. Comparing to the above methods, the proposed method is more practical and can be immediately used in the patient surgical planning process.

## CHAPTER III

3D SEGMENTATION OF MAXILLA IN CONE-BEAM COMPUTED  
TOMOGRAPHY IMAGING USING BASE INVARIANT WAVELET SHAPE  
MODEL

## A. Introduction

The field of craniomaxillofacial (CMF) surgery involves the correction of congenital and acquired deformities of the skull and face. It includes dentofacial deformities, congenital deformities, combat injuries, post-traumatic defects, defects after tumor ablation, and deformities of the temporomandibular joint. Due to the complex nature of the craniomaxillofacial skeleton, the surgical correction of CMF deformities is among the most challenging. These types of the surgeries usually require extensive surgical planning. The success of these surgeries depends not only on the technical aspects of the operation, but to a larger extent on the formulation of a precise surgical plan. During the past 50 years, there have been significant improvements in the technical aspects of surgery (e.g., rigid fixation, resorbable materials, distraction osteogenesis, minimally invasive approaches, etc). However, the planning methods remain mostly unchanged [1–4]. At present, in CMF surgery, it is clear that many unwanted surgical outcomes are the result of deficient planning.

The advent of computed tomography (CT) and its 3D reconstruction have brought about a revolution in diagnostic radiology since cross-sectional imaging becomes available [5–7]. 3D rendered visualization provides a surgeon with readily recognizable images of complex anatomic structures. It can exactly record and represent the life-size and the shape of soft tissue and bone for precise surgical planning and simulation. In conjunction with appropriate computer software and hardware, computer-aided surgical simulation (CASS) has been developed and has created a number of options



Fig. 20. A skull model reconstructed by Marching Cube Algorithm after thresholding segmentation is performed on a 3D CBCT volumetric image.

for CMF surgeries [3, 8–12].

Cone-beam computed tomography (CBCT) has been adopted rapidly in the past decades and widely used in dentomaxillofacial imaging and orthodontic practices [35–37]. The most important reason is that currently, the effective dose of CBCT for a head scan (from several dozens up to several hundreds  $\mu\text{Sv}$ ) is significantly lower than that of CT for a head scan (from several hundreds up to several thousands  $\mu\text{Sv}$ ) [35, 38, 39]. Furthermore, reported spatial resolution (voxel resolution) varies from 0.076 to 0.4mm [35]. Although the spatial resolution of a slice in CT can be as small as 0.4mm, the thinnest axial thickness is 0.625mm. CBCT also offers particular accessibility for most of the medical units because of its low cost compared with CT. Commercially available CBCT allows patients to seat or stand vertically during scanning. Natural head position (NHP) can be acquired directly for 3D cephalometry. These advantages have created the possibilities of replacing CT with CBCT for 3D imaging and modeling of CASS [40–43].

Surgical planning and CASS require accurate contours of facial bones<sup>1</sup>. The acquisition of a skull model in traditional CT includes two steps: thresholding seg-

---

<sup>1</sup>Facial bones includes maxilla, zygomatic bone, lacrimal bone, nasal bone, and vomer in lower part of cranium, and temporal bone, sphenoid bone, parietal bone, and frontal bone in upper part of cranium

mentation and bone surface reconstruction. The thresholding segmentation can easily classify bone voxels because of the calibrated Hounsfield unit (HU) gray values and high contrast resolution (signal-to-noise ratio) of CT. These bone images are then fed to surface reconstruction algorithm such as Marching Cube Algorithm to obtain bone surface. Therefore, accurate segmentation of bone voxels is one of the most essential tasks for 3D rendering and CASS. However, poor image quality becomes its major limitation in establishing skull models in CBCT. Fig. 20 illustrates a skull model obtained by thresholding segmentation and Marching Cube Algorithm in CBCT imaging. The characteristics of degraded images in CBCT imaging can be summarized as follows. First, intensities of CBCT images cannot be accurately represented by standard HU because of no absolute HU calibration. It varies between scanners and between scans. In order to reconstruct bone surfaces with reasonable quality, deciding the threshold for segmenting bone images becomes an art (by guessing and trying). Second, when a unique global threshold is applied, some thin bony structures are usually not included. The sella turcia, orbital walls, nasal, surrounding thin bones of maxillary sinus, condyles, and ramus of the mandible are among the most affected bone structures. This is mainly because their image intensities are averaged with those of air during filter-backprojection reconstruction of CBCT. Third, the effect of low contrast resolution in CBCT creates randomly scattered noisy images and the bumpy surfaces of the skull model. It results from any combinations of beam-hardening effect, truncation effect, and Compton scattering. Finally, metal artifact can be the most detrimental in building skull models. It is mostly unavoidable since the dental fillings, implants, surgical plates, and orthodontic appliances are among the most common metallic materials existing inside patients' teeth and heads. Although metal artifacts are reduced in CBCT images compared with those in CT images, its effect is still considerable compared with the other effects described above.

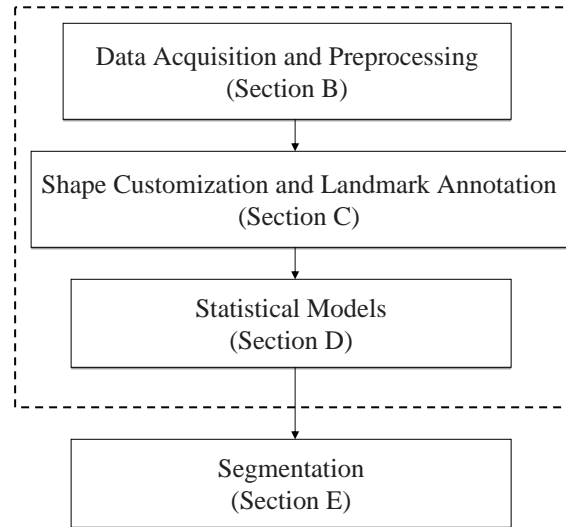


Fig. 21. The procedure of performing segmentation in the study. The statistical models are acquired off-line (enclosed by dashed lines) by using training CBCT datasets. Once the statistical models are built, a new CBCT image (other than the training datasets) is segmented based on the information of statistical models.

In order to solve the addressed problems above, there are a number of the studies in advanced segmentation and reconstruction approaches of facial bone images in CT and CBCT imaging. They are segmentations based on statistical shape model (SSM) in CT imaging [44–46] and in CBCT imaging [47] and histogram thresholding segmentation in CT imaging [48]. Loubele *et al.* [49] models local histogram as a mixture of Gaussian distributions and determines the thresholds of jawbones (mandible and part of maxilla) and soft tissues in CBCT imaging. However, studies on developing robust segmentation algorithms versatile for most of the facial bones in CBCT imaging are still limited. Facial bones are characterized by complex and inhomogeneous structures (e.g. soft tissues, sinuses, and pieces of soft bones). Voxel-based global and local segmentation based on assumption of homogeneous structures may not be appropriate. Only the trained specialists can manually identify the internal

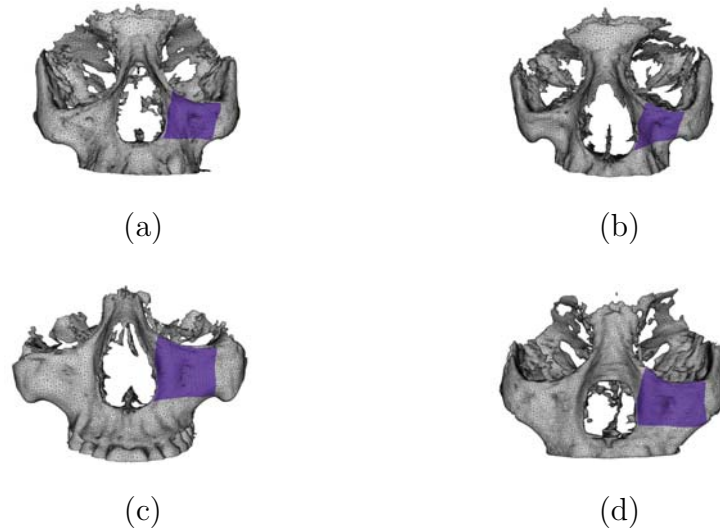


Fig. 22. Four different skull models are illustrated in (a), (b), (c), and (d). The marked regions are anterior maxilla in the left half of skull and will be the particular interest in the study.

structures of facial bones. This limitation makes it difficult to design segmentation algorithms for the bone voxels and bone surfaces of the internal structures of facial bones. In CASS, the visualization and measurement of simulation relies on the outer surfaces of facial bones. The requirement on accuracy of outer surface of facial bones is more critical than that on accuracy of internal structures of facial bones.

In this study, a new segmentation approach based on wavelet density model (WDM) for a particular interest on left half of anterior maxilla will be proposed. This region consists of thin bones around maxilla sinus and is most likely to be influenced by limitation of CBCT. The procedure of performing segmentation throughout this study is summarized step-by-step in Fig. 21. Table V lists all acronyms in the study. This model-based segmentation approach calculates the outer bone surface on left half of anterior wall of maxilla. Fig. 22 shows four different skulls. The marked regions on left half of anterior wall of maxilla represent four different shapes. It is obvious that the shape for SSM is a partial open-surface with closed boundary in a skull

Table V. List of Acronyms

ASM	Active Shape Model
BIWASM	Base Invariant Wavelet Active Shape Model
CASS	Computer-aided Surgical Simulation
CBCT	Cone-beam Computed Tomography
CMF	Craniofacial
CT	Computed Tomography
CWBI	Customized Wavelet Base Initialization
DSWT	Discrete Surface Wavelet Transform
DWT	Discrete Wavelet Transform
HU	Hounsfield Unit
IFM	Image Feature Model
RBI	Registration-based Initialization
SSM	Statistical Shape Model
PDM	Point Distribution Model
WASM	Wavelet Active Shape Model
WDM	Wavelet Distribution Model

model. The outline of this manuscript is listed as follows. First of all, the acquisition and preprocessing of CBCT images will be presented in Section B. Then, a practical procedure to creating training shapes with regularized landmarks will be proposed in Section C. It includes extraction and customization of training shapes and landmark digitalization on training shapes. In Section D, we will describe two statistical models. The first statistical model is wavelet-based SSM called WDM. The second statistical model is IFM. Based on those two statistical models, a new model-based segmentation algorithm BIWASM with a new initialization method CWBI will be proposed in Section E. Next, BIWASM with CWBI will be validated and compared with three different approaches in Section F. Finally, Section G will discuss these approaches, results, and the feasibility of BIWASM in CASS.

The notation used in this paper is described as follows. Bold symbols  $\mathbf{A}$  and  $\mathbf{a}$  are represented as a matrix and a column vector, respectively.  $\mathbf{a}^T$  defines matrix transpose of  $\mathbf{a}$ .  $\|\mathbf{a}\| \equiv \sqrt{\mathbf{a}^T \mathbf{a}}$  is the Euclidean norm of a column vector  $\mathbf{a}$ . A 3D point  $\mathbf{a}$  is represented as a 3-tuple column vector  $(a_x, a_y, a_z)^T$  in a *Cartesian* coordinate system. The symbol  $\mathcal{T}(\bullet)$  with any kinds of subscripts and superscripts denotes spatial transformation of 3D points.  $\mathcal{W}$  and  $\mathcal{W}^{-1}$  denote wavelet transform and inverse wavelet transform.

## B. Data Acquisition and Preprocessing

Nineteen patients were scanned using CBCT (Sirona, Bensheim, Germany) with a voxel resolution of  $0.287\text{mm} \times 0.287\text{mm} \times 0.287\text{mm}$ ,  $512 \times 512 \times 512$  voxels,  $0^\circ$  gantry tilt, and 1:1 pitch. Nineteen CBCT volumetric images were acquired. Thresholding segmentation was first applied to each of these volumetric images to obtain bone images. Due to limitation in CBCT imaging, these bone images were recovered by manually editing images slice by slice. Then, Marching Cube Algorithm was applied

to each of the recovered bone images to calculate surfaces (meshes) of bone images. Finally, the surfaces of bone images were smoothed using the software (Amira, San Diego, CA) to remove the bumpy surfaces. These bone surfaces are the ground truths for surfaces of physical skeleton. We will use these 19 ground truths of bone surfaces: 1) to customize the shapes and generate landmarks in Section C; and 2) to validate the proposed segmentation approach in Section F.

### C. Shape Customization and Surface Wavelet Transform

The shape information of a target in a subject is characterized by a dense set of points and mesh structures. A SSM of the target is based on shape statistics of customized points on a set of the training datasets. These customized points are called landmarks. Before constructing a SSM, each training shape is remeshed into a new shape with the same number of landmarks and same mesh structures by digitalizing the shape either manually or automatically. Landmarks must be placed at topologically and structurally corresponding positions over all training shapes.

In this section, we will describe approaches to extracting and customizing a shape from the ground truth of bone surface and generating its landmarks for SSM. The shape (the target) in our study is the marked region on the skull (the subject) illustrated in Fig. 22. In the following, we will use the shape in Fig. 22 (a) to illustrate results calculated by each of the steps in the approaches. These steps are summarized in Fig. 23.

#### 1. Training Shape Extraction and Patch Decomposition

The training shape of the target is identified by first manually pinpointing anatomical control landmarks on ground truth of bone surface and then determining the boundaries of the training shape. The training shape is the regions defined by these enclosed

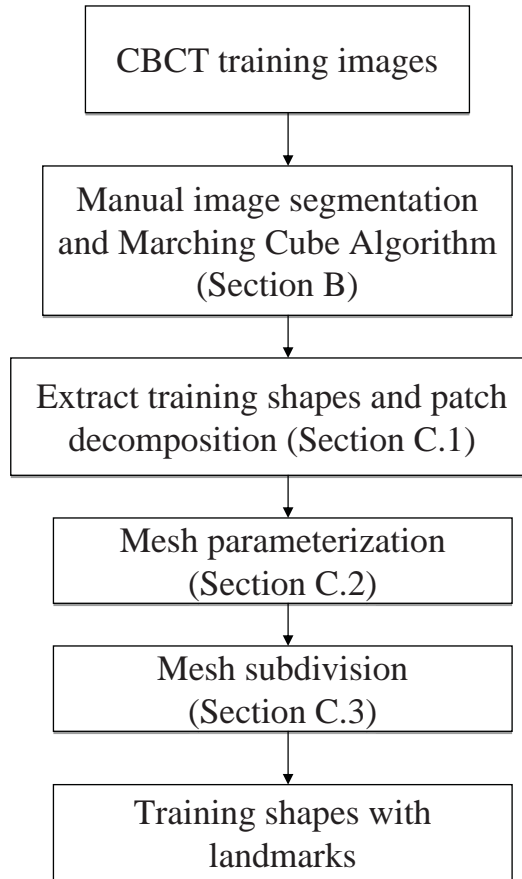


Fig. 23. The procedure of generating training shapes with digitalized landmarks. These training shapes will be used to build SSM in Section D.

boundaries. Patch decomposition is performed by dividing the training shape into several patches. It can be implemented similarly by manually pinpointing anatomical control landmarks on the training shape and then determining the boundaries of patches. Each of the boundaries is obtained by calculating a shortest path or a path<sup>2</sup> composed of several connected shortest paths on the ground truth of bone surface between the anatomical control landmarks. Fig. 24 (a) shows that 8 anatomical control

---

<sup>2</sup>When the shortest path cannot be found, several auxiliary points can be placed in-between and connected by shortest paths form a path.

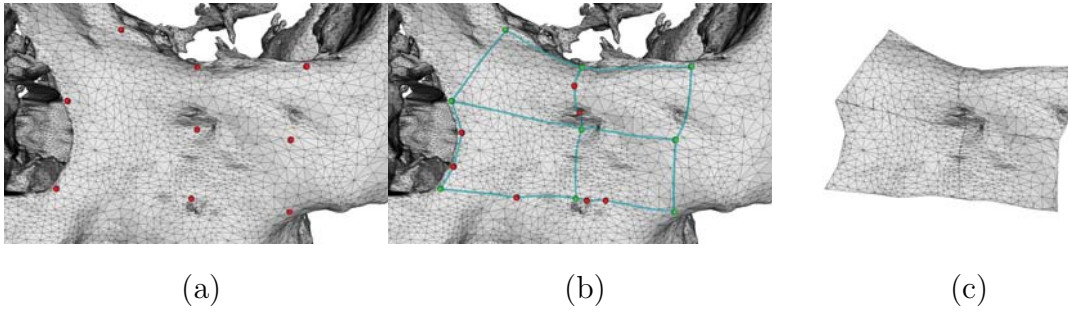


Fig. 24. Training shape extraction and patch decomposition. (a) 9 anatomical control landmarks. (b) Patch decomposition using shortest paths as boundaries. (c) Extraction of the training shape and its patches.

landmarks are used to define the training shape, and one anatomical control landmark is used to define four patches. Fig. 24 (b) illustrates the boundaries. Finally, these patches are extracted from the bone surfaces to form a customized training shape shown in Fig. 24 (c).

The shortest path on a mesh is defined and calculated as follows. Assume  $A$  and  $B$  are two points on the mesh. When the mesh is unfolded onto a plane (by breaking the connection of cells and rotating the cells),  $A$  and  $B$  are also translated onto the plane accordingly. Let  $A'$  and  $B'$  be the points corresponding to  $A$  and  $B$  on the plane, respectively. It is possible to draw a straight line between  $A'$  and  $B'$  on the plane so that the line passes through cells of this unfolded mesh. This line on the unfolded mesh corresponds to a path on the original mesh. Of the note that this path passes through the valid cells on the mesh instead of only vertices and edges. The shortest path on the mesh is the one with minimum distance (distance of straight line) among all existing paths of that kind. Since calculating shortest paths without any simplifications is computationally expensive, we use Chen & Han's efficient algorithm to calculate shortest paths [50]. Since this searching algorithm uses all the cells in the mesh to find the shortest path, it is necessary to reduce the searching region [51].

It can be done by two steps of precalculation to determine this searching region. The first step of precalculation is that Dijkstra's shortest path algorithm [52] is used to calculate the Dijkstra's shortest path between  $A$  and  $B$ . This algorithm can quickly find the shortest path of connecting edges. The second step of precalculation is that the searching region can be determined by searching all the neighboring cells in a specific distance to the Dijkstra path. We use 0.2 times of the Dijkstra's shortest path as this specific distance.

## 2. Parameterization

Once the patches of the training shape are obtained, we will define their corresponding planar parameterization domains and the mappings. We use one of the patches (denoting  $\mathcal{P}$ ) shown in Fig. 2(a) to illustrate its planar parameterization domain and mapping shown in Fig. 25(b).

First, the planar parameterization domain of  $\mathcal{P}$  is determined as follows. Since  $\mathcal{P}$  is defined by anatomical control landmarks, the planar parameterization domain can be defined as a polygon by those anatomical control landmarks. Assume  $\{\mathbf{l}_k\}_{k=0}^{K_p-1}$  denotes the  $K_p$  anatomical control landmarks forming  $\mathcal{P}$ , and  $\mathbf{l}_k$  and  $\mathbf{l}_{(k+1)_{K_p}}$  are the anatomical control landmarks connected by a boundary path of  $\mathcal{P}$ , where  $(k)_{K_p}$  means  $k$  modulo  $K_p$ . Let  $\{T_i\}_{i=0}^{K_p-3}$ ,  $T_i \equiv \triangle(\mathbf{l}_0, \mathbf{l}_{i+1}, \mathbf{l}_{i+2})$  be the planar triangles for patch  $\mathcal{P}$ . Since  $\{T_i\}_{i=0}^{K_p-3}$  are usually not coplanar, we can "unfold" these planar triangles  $\{T_i\}$  onto a common plane create a planar  $K_p$ -polygon. This new planar  $K_p$ -polygon will become the parameterization domain for  $\mathcal{P}$ . The edges of the planar  $K_p$ -polygon are composed of line segments between  $\mathbf{l}_k$  and  $\mathbf{l}_{(k+1)_{K_p}}$  (distance between two points in 3D space) while the boundaries of  $\mathcal{P}$  are formed by the shortest pathes on the mesh between  $\mathbf{l}_k$  and  $\mathbf{l}_{(k+1)_{K_p}}$ . Therefore, it can be claimed that  $\mathcal{P}$  resembles the planar  $K_p$ -polygon.



Fig. 25. Illustration of parameterization. (a) One of four patches in Fig. 24(c). (b) The polygonal domain and its parameterization mapping.

Second, the parameterization mapping of  $\mathcal{P}$  will be calculated using barycentric mapping [53]. Mean Value Coordinate will be used to calculate the spring constants. The planar  $K_p$ -polygon is assumed to be convex in order to guarantee the bijectivity of parameterization [53]. The convexity of the  $K$ -planar polygon can be achieved by carefully configuring  $\{\mathbf{l}_k\}_{k=0}^{K-1}$  when performing patch decomposition. Moreover, before calculating barycentric mapping, the mapping of boundaries between  $\mathcal{P}$  and its planar  $K_p$ -polygon has to be defined. A simple approach can be done by proportionally projecting the boundary vertices of  $\mathcal{P}$  onto the edges of its planar  $K_p$ -polygon domain to obtain the boundary mapping.

### 3. 3D Landmarks Digitalization Using Catmull-Clark Subdivision

The landmarks of each training shape will be digitalized by the Catmull-Clark subdivision proposed by Catmull *et al.* [54] in several steps. The first step is to use the Catmull-Clark subdivision algorithm to generate new points on the parameterization domain (i.e. planar  $K_p$ -polygon) of  $\mathcal{P}$ . This planar  $K_p$ -polygon is a base mesh at 0-th subdivision. Fig. 26(a) illustrates base meshes of a triangle and a quadrilateral. The vertices of the base meshes denote  $\mathbf{v}^0$ . After performing one subdivision on the base meshes, it creates new points  $\mathbf{f}^1$ , and  $\mathbf{e}^1$  and the updated vertices  $\mathbf{v}_1$  shown in Fig. 26(b).  $\mathbf{f}^1$  is called face point corresponding to the cells at the base meshes.  $\mathbf{e}^1$  is

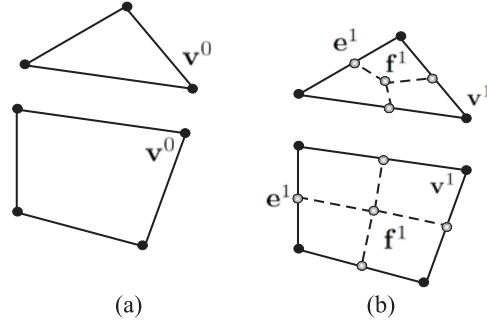


Fig. 26. Catmull-Clark subdivision. (a) Triangle base mesh and quadrilateral-like base mesh. (b) The supermeshes generated by one subdivision of the base meshes.

called edge point corresponding to the edges at the base meshes.  $\mathbf{v}^1$  corresponds to the original vertex  $\mathbf{v}^0$  at the base meshes. New edges of the supermesh are formed by connecting  $\mathbf{f}^1$  and  $\mathbf{e}^1$  and by connecting  $\mathbf{v}^1$  and  $\mathbf{e}^1$ . Before performing the next subdivision, all  $\mathbf{f}^1$ ,  $\mathbf{e}^1$ , and  $\mathbf{v}^1$  are relabeled to  $\mathbf{v}^1$  as the input of the second subdivision.

Similarly, after the  $j$ th subdivision is performed,  $\mathbf{v}^j$  (vertex),  $\mathbf{f}^j$  (face point), and  $\mathbf{e}^j$  (edge point) can be acquired in the same way. The  $j$ -th Catmull-Clark subdivision operated on  $\mathbf{v}^{j-1}$  is summarized in **Algorithm 3**.  $n_v$  is called the valence of vertex  $\mathbf{v}^j$  (the number of edges connecting  $\mathbf{v}^j$ ). The average operator  $\bar{\mathbf{k}}_{\mathbf{m}}$  means the vertex of type  $\mathbf{m}$  is obtained by using the neighboring vertices of  $\mathbf{k}$  and calculating the average of them. Fig. 27 summarizes all possible average operators.  $\mathbf{m}$  represents one of the corresponding averaged vertex, face point, and edge point. Of the note that type  $\mathbf{m}$  in  $\bar{\mathbf{k}}_{\mathbf{m}}^{j-1}$  is calculated by averaging centroid of face ( $\mathbf{f}$ ), midpoint of edge ( $\mathbf{e}$ ), or original vertex ( $\mathbf{v}$ ) in the submesh [the mesh before performing subdivision] instead. On the other hand, type  $\mathbf{m}$  in  $\bar{\mathbf{k}}_{\mathbf{m}}^j$  is calculated by averaging  $\mathbf{v}^j$ ,  $\mathbf{f}^j$ , or  $\mathbf{e}^j$  in the supermesh (the mesh after performing subdivision).

At the second step, the patch  $\mathcal{P}$  with landmarks are remeshed by inverse mapping the points (generated by subdivision) on the parameterization domains (planar  $K_p$ -polygon) onto  $\mathcal{P}$ . The same number of the subdivisions is applied to each of

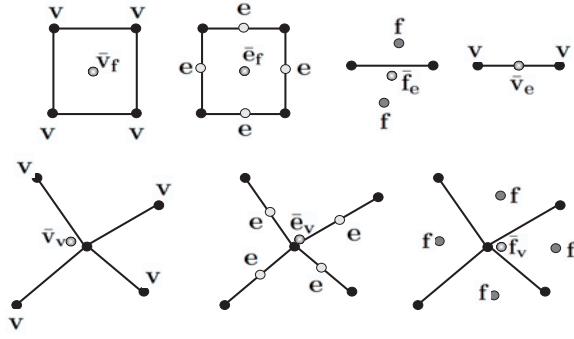


Fig. 27. The average operators  $\bar{\mathbf{k}}_m^j$  without superscript index  $j$ .

the patches in each training shape. Finally, the remeshed shape with regularized landmarks can be obtained by stitching these remeshed patches. Since two patches sharing a boundary have the same parameterization mapping on the shared boundary, both the patches will result in the same subdivision on this boundary. Hence, the remeshed patches can be stitched by merging the vertices at boundaries. Fig. (28) illustrates the remeshed and stitched training shape calculated after 0-th, first, third, and fifth subdivision of four base meshes. The training shape corresponding to 0-th subdivision is the mesh formed by anatomical control landmarks. In our study, the number of the subdivisions is 5.

---

**Algorithm 3** Catmull-Clark subdivision algorithm

---

$$\mathbf{f}^j \leftarrow \bar{\mathbf{v}}_f^{j-1}$$

$$\mathbf{e}^j \leftarrow \frac{1}{2}(\bar{\mathbf{v}}_e^{j-1} + \bar{\mathbf{f}}_e^j)$$

$$\mathbf{v}^j \leftarrow \frac{1}{n_v}(\bar{\mathbf{f}}_v^j + \bar{\mathbf{v}}_v^{j-1} + (n_v - 2)\mathbf{v}^{j-1})$$

$$\mathbf{v}^j \leftarrow \{\mathbf{f}^j, \mathbf{e}^j, \mathbf{v}^j\}$$


---

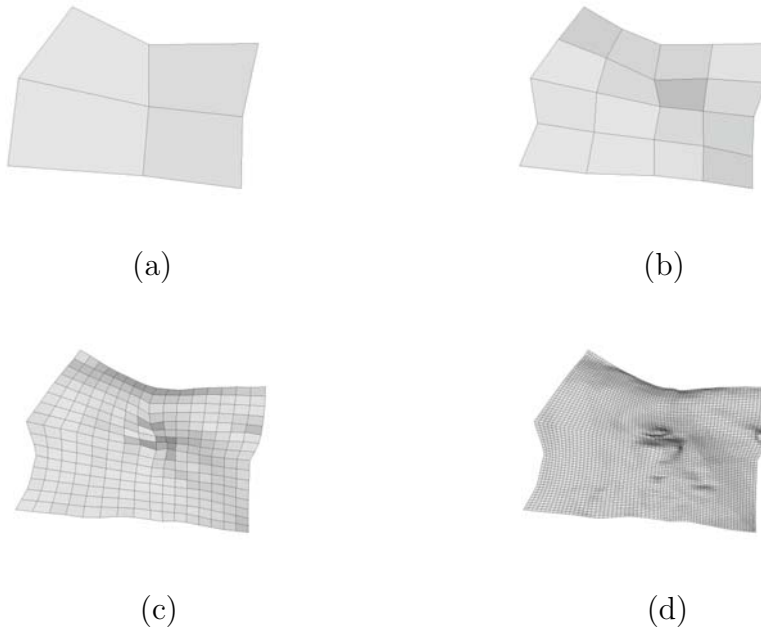


Fig. 28. The remeshed shape with landmarks after different number of Catmull-Clark subdivisions. (a) 0-th subdivision. (b) First subdivision. (c) Third subdivision. (d) Fifth subdivision.

#### D. Wavelet Active Shape Model

Two statistical models summarized in Fig. 29 will be built by using  $N$  training images and their corresponding  $N$  training shapes with regularized landmarks (calculated in Section C). The first statistical model is WDM using training shapes. It is the multiscale statistical shape model based on PDM (Section D.1) by using DSWT (Section D.2). The second statistical model is IFM created by using both training shapes and training images.

##### 1. Point Distribution Model

Point distribution model (PDM) is introduced by Taylor *et al.* [55]. Let  $S_i$  be the set of  $n$  landmarks [illustrated in Fig. 28(d)] in  $i$ th training shape. We say  $S_i$  consists

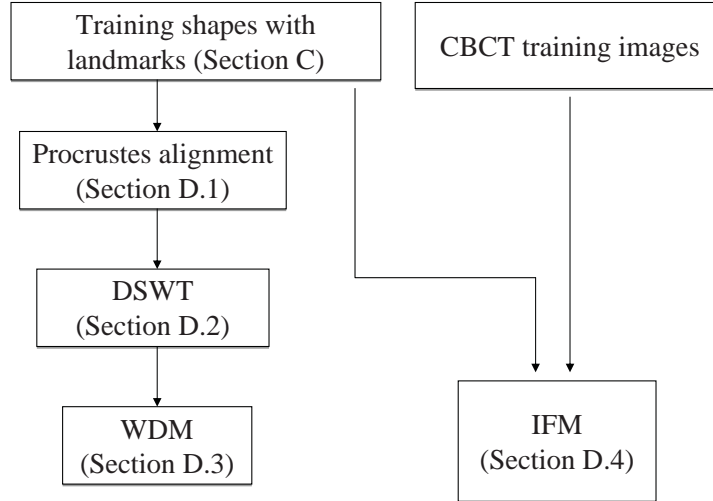


Fig. 29. The flowchart of creating WDM and IFM.

of landmarks in the image space. All the training shapes are transformed (rotation, translation, and scaling) to a common coordinate of model space using Procrustes Analysis [56] to minimize their squares of distance. Let  $\tilde{S}_i$  be the transformed training shape. We say  $\tilde{S}_i$  is the  $i$ th training shape in the model space. Assume  $\mathbf{x}_i$  is the  $3n$ -dimensional shape vectors formed by concatenation of the coordinates of all transformed landmarks in  $\tilde{S}_i$ .  $\mathbf{x}_i$  can be expressed by the mean vector  $\bar{\mathbf{x}} \equiv \frac{1}{N} \sum_{i=0}^{N-1} \mathbf{x}_i$  and shape variation vectors  $\Delta \mathbf{x}_i \equiv \mathbf{x}_i - \bar{\mathbf{x}}$ . The distribution of SSM can be characterized by the covariance matrix of shape variation vectors given by

$$\mathbf{C}_x \equiv \frac{1}{N-1} \sum_{i=0}^{N-1} \Delta \mathbf{x}_i \Delta \mathbf{x}_i^T. \quad (3.1)$$

In order to capture the dominant shape variations, Principle Component Analysis is applied to the set of shape variation vectors. A set of orthogonal principle axes (also called principle modes) of shape variations can be found by calculating the orthogonal eigenvectors of  $\mathbf{C}_x$ , and the corresponding eigenvalues are the variances

of the distribution in the direction of principle axes. Assume the columns of  $\mathbf{P}$  are the orthogonal eigenvectors with the corresponding nonzero eigenvalues  $\lambda_k$  in the descending order. A shape vector  $\tilde{\mathbf{x}}$  in the model space can be generated by a shape parameter  $\tilde{\mathbf{b}}$ :

$$\tilde{\mathbf{x}} = \bar{\mathbf{x}} + \mathbf{P}\tilde{\mathbf{b}}. \quad (3.2)$$

Any shape vector  $\mathbf{x}$  in the model space can be approximated by projecting the shape variation vector  $\Delta\mathbf{x} \equiv \mathbf{x} - \bar{\mathbf{x}}$  onto the subspace (spanned by  $\mathbf{P}$ ) of the model

$$\mathbf{x} \approx \bar{\mathbf{x}} + \mathbf{P}\mathbf{b}. \quad (3.3)$$

Its shape parameter  $\mathbf{b}$  can be calculated by the least square solution of minimizing  $\|\Delta\mathbf{x} - \mathbf{P}\mathbf{b}\|^2$

$$\mathbf{b} = \mathbf{P}^T \Delta\mathbf{x}. \quad (3.4)$$

A shape vector  $\mathbf{x}$  is said to be defined in the model space if it is expressed by (3.2) or approximated by (3.3). A shape vector  $\mathbf{y}$  is said to be defined in an image space if its landmark points are located under the coordinate of a volumetric image. Once the PDM is built, a shape vector in the image space can be represented or approximated by a shape vector in PDM. Assume a PDM with shape priors  $(\mathbf{P}, \lambda_k)$  is calculated from  $\{S_i\}$ . Let  $\mathbf{y}$  be a shape vector of an arbitrary shape  $S$  in the image space. Of the note that the shape  $S$  is not among any of the training shapes  $S_i$ . One of the approaches to calculating a shape vector in the model space to best represent  $\mathbf{y}$  is to find a transformation  $\mathcal{T}$  and a shape parameter  $\mathbf{b}$  to minimize mean squares:

$$\|\mathbf{y} - \mathcal{T}(\bar{\mathbf{x}} + \mathbf{P}\mathbf{b})\|^2. \quad (3.5)$$

$\mathcal{T}$  is transformation consisting of rotation, translation, and scaling of a shape.

The eigenvalues  $\lambda_k$  can be used to provide the bounds of the model in order to

ensure the shape is plausible. The values of  $\mathbf{b}$  are constrained between

$$-a\sqrt{\lambda_k} < b_k < a\sqrt{\lambda_k} \quad (3.6)$$

where  $2 \leq a \leq 3$  generally, and  $b_k$  is an element of  $\mathbf{b}$ . A simple algorithm of calculating suboptimal  $\mathcal{T}$  and  $\mathbf{b}$  by minimizing mean squares (3.5) and incorporating shape constraints is summarized in **Algorithm 4**.

---

**Algorithm 4** A simple algorithm of calculating suboptimal  $\mathcal{T}$  and  $\mathbf{b}$  by minimizing (3.5) and incorporating shape constraints.

---

$\mathbf{b} \leftarrow \mathbf{0}$

**while** Until convergence **do**

$\mathbf{x} \leftarrow \bar{\mathbf{x}} + \mathbf{P}\mathbf{b}$ ; generate a shape in the model space using (3.2).

    Calculate  $\mathcal{T}$  by minimizing  $\|\mathbf{y} - \mathcal{T}(\mathbf{x})\|^2$  using [57]

$\mathbf{x}' \leftarrow \mathcal{T}^{-1}(\mathbf{y})$ ; calculate inverse spatial transform of  $\mathbf{y}$ .

$\mathbf{b} \leftarrow \mathbf{P}^T(\mathbf{x}' - \bar{\mathbf{x}})$ ; calculate the shape parameters fitting  $\mathbf{x}'$  using (3.3).

    Apply shape constraints on  $\mathbf{b}$  using (3.6)

**end while**

---

## 2. Discrete Surface Wavelet Transform Based on Catmull-Clark Subdivision

In the following, we will perform multiscale analysis on each aligned training shape  $\tilde{S}_i$  in the model space. By properly choosing anatomical control landmarks and performing patch decomposition (such as Fig. 1), we can generate landmarks on the training shapes with a rectilinear structure at any level of Catmull-Clark subdivision. Since the rows and columns of the rectilinear training shapes can be well-defined, DSWT of the training shapes can be calculated by performing 2D DWT on rectilinear shapes

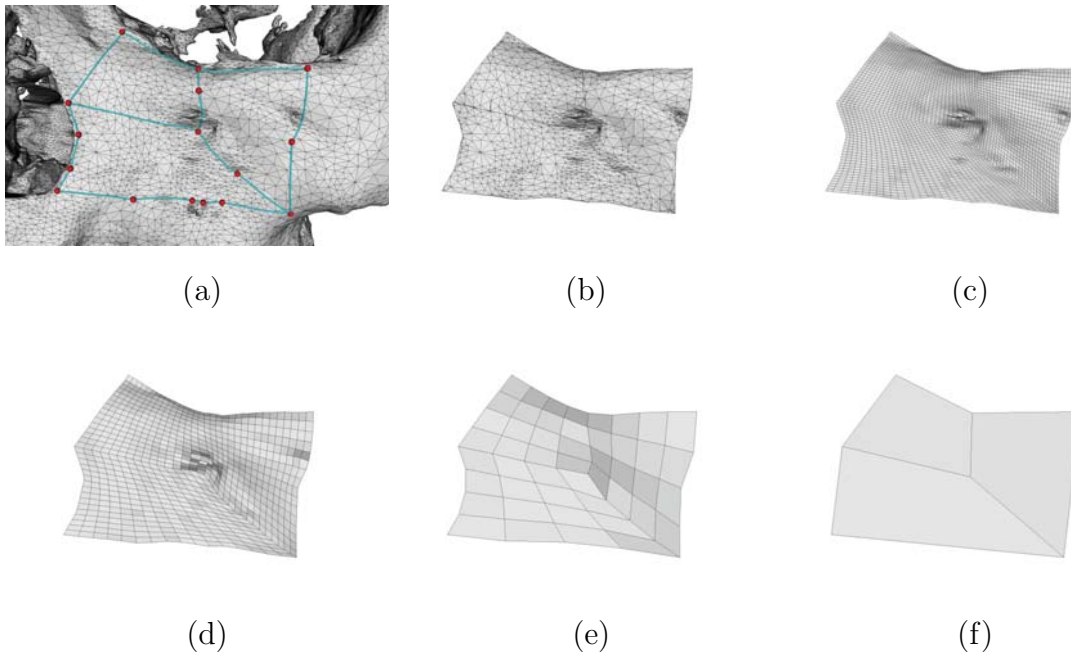


Fig. 30. Illustration of scaling coefficients for different patch decomposition of the shape. (a) Different patch decomposition applied to the same shape in Fig. 24. (b) The extracted shape (c) The shape at five Catmull-Clark subdivisions. (d) Scaling coefficients after one decomposition of DSWT. (e) Scaling coefficients after three decompositions of DSWT. (f) Scaling coefficients (base) after five decompositions of DSWT.

in  $x$ -,  $y$ -, and  $z$ -coordinate<sup>3</sup>.

However, there are exceptions. When the training shape is decomposed into patches such as the ones in Fig. 30(a) using the same set of anatomical control landmarks, there are two pentagon-like patches and one quadrilateral-like patch forming the training shape [Fig. 30(b)]. After any level of Catmull-Clark subdivision on the patches is performed and the remeshed patches are stitched, the resulting training shape always has an extraordinary landmark (except landmarks on the boundaries) with valence three [54]. Fig. 30(c) shows the remeshed shape with the fifth subdivi-

<sup>3</sup>It is equivalent to perform 2D DWT on a 2D image. The image intensity is each of the coordinates (e.g.  $x$ -coordinate) of landmarks.

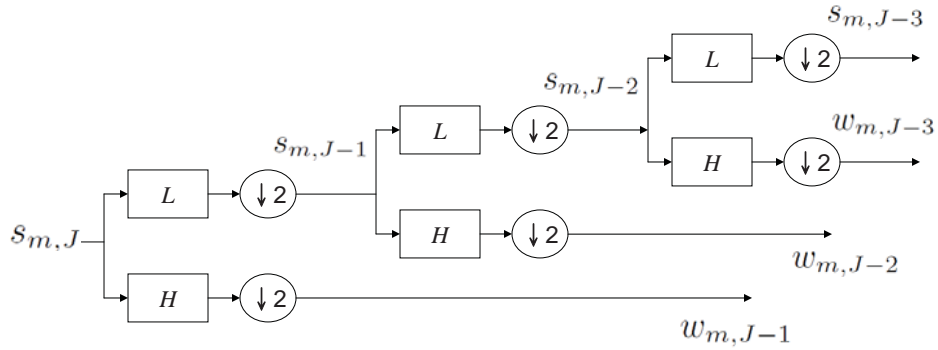


Fig. 31. The decompositions in 1D DWT.

sion. It is obvious that 2D DWT cannot be performed on this grid-like mesh since rows and columns of a rectilinear structure are not well-defined.

To overcome this problem, Bertram *et al.* [58] proposed a new construction of wavelet on Catmull-Clark subdivision surfaces of arbitrary two-manifold topology by designing a new lifting scheme of biorthogonal wavelet transform. The training shape and its patches can be customized, and its DSWT can be constructed accordingly. The lifting scheme of 2D DWT and Bertram *et al.*'s proposed lifting scheme will be first introduced based on the rectilinear grid. Then, we will discuss how this new lifting scheme can skillfully perform multiscale decomposition on the training shape with a non-rectilinear structure.

Fig. 31 shows the decompositions in 1D DWT. An input  $s_{m,J}$  at a resolution of  $J$ -scale can be decomposed into wavelet coefficients  $w_{m,J-1}$  and scaling coefficients  $s_{m,J}$  at  $(J-1)$ -scale by a high pass filter ( $H$ ) and a low pass filter ( $L$ ) followed by downsampling.  $w_{m,J-1}$  represents the signal details of  $s_{m,J}$  at  $(J-1)$ -scale, whereas  $s_{m,J-1}$  represents the content of coarser scale of  $s_{m,J}$ . It is shown that one decomposition of any classic DWT with finite filters in Fig. 31 can be implemented by starting from the Lazy wavelet transformation (splitting) and then performing a finite number

of alternating lifting steps [59]. The DWT using lifting scheme consists of two steps. At the first step of lifting scheme, the scaling coefficient  $s_{m,j}$  at  $j$ -th scale is split into  $s$ -set and  $w$ -set:

$$s_{m,j-1} \leftarrow s_{2m,j} \quad (3.7)$$

$$w_{m,j-1} \leftarrow s_{2m+1,j}. \quad (3.8)$$

At the second step of lifting scheme, a number of consecutive lifting steps are calculated. Only one of  $s$ -lifting (3.9) and  $w$ -lifting (3.10) steps is calculated at  $l$ -th lifting step:

$$s_{m,j-1} \leftarrow \alpha^{(l)} s_{m,j-1} + \sum_k \alpha_k^{(l)} w_{k,j-1} \quad (3.9)$$

$$w_{m,j-1} \leftarrow \beta^{(l)} w_{m,j-1} + \sum_k \beta_k^{(l)} s_{k,j-1} \quad (3.10)$$

The inverse DWT using lifting scheme is simply the analogous operations of (3.9) and (3.10) in the reverse order to satisfy perfect reconstruction:

$$s_{m,j-1} \leftarrow \frac{1}{\alpha} \left( s_{m,j-1} - \sum_k \alpha_k w_{k,j-1} \right) \quad (3.11)$$

$$w_{m,j-1} \leftarrow \frac{1}{\beta} \left( w_{m,j-1} - \sum_k \beta_k s_{k,j-1} \right) \quad (3.12)$$

Fig. 32(a) shows lifting steps of one decomposition of 2D DWT. 1D DWT is first performed on the rows and then performed on the columns by using lifting steps.

The new lifting scheme designed by Bertram *et al.* is shown in Fig. 32(b). Instead of performing the lifting steps first on the rows and then on the columns, each row lifting step and its corresponding column lifting step will be performed at the same time before moving on the next row and column lifting steps. Since lifting steps are linear operations, the resulting decomposition of 2D DWT in Fig. 32(b) is equivalent to the one in Fig. 32(a). This new lifting scheme also consists of two

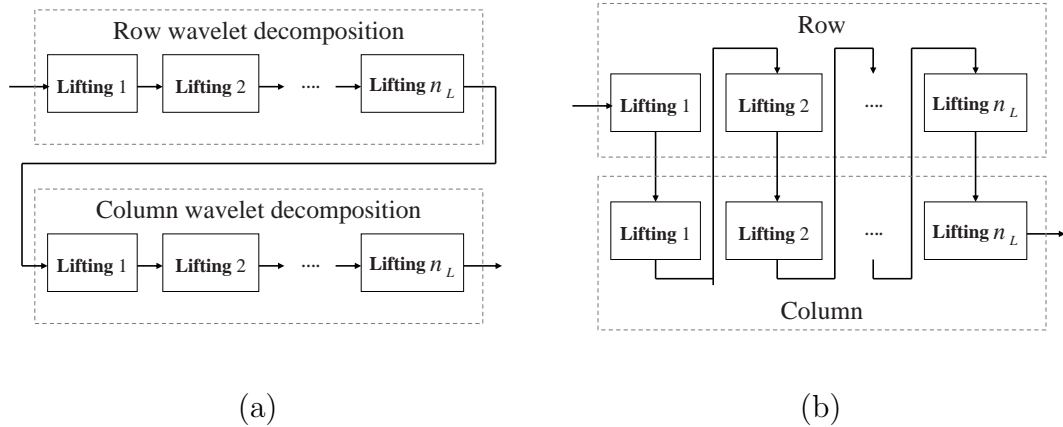


Fig. 32. (a) One decomposition of 2D DWT using lifting steps (b) One decomposition of 2D DWT using composite lifting steps.

steps. At the first step of the new lifting scheme, the splitting is performed on the landmarks of the training shape based on the structure of Catmull-Clark subdivision. As described in Section C.3, the landmarks of the training shape are obtained by Catmull-Clark subdivision and can be classified into vertex  $\mathbf{v}$ , face points  $\mathbf{f}$ , and edge points  $\mathbf{e}$  before relabeling in **Algorithm 3** (The superscript is ignored for simplicity).  $\mathbf{v}$  is split as scaling coefficients similar to (3.7).  $\mathbf{f}$  is split as wavelet coefficients similar to (3.8).  $\mathbf{e}$  can be split as scaling coefficients (when **s-lifting** is performed) or wavelet coefficients (when **w-lifting** is performed). At the second step of the new lifting scheme, the operations of lifting steps in each of row and column liftings) are defined as

$$s_{m,j-1} \leftarrow \alpha s_{m,j-1} + \tilde{\alpha}(w_{m,j-1} + w_{m-1,j-1}) \quad (3.13)$$

$$w_{m,j-1} \leftarrow \beta w_{m,j-1} + \tilde{\beta}(s_{m,j-1} + s_{m-1,j-1}) \quad (3.14)$$

The superscript  $l$  is ignored for simplicity. It can be shown in Appendix B that the composite **s-lifting** step for each of the vertex  $\mathbf{v}$  and each of the edge points  $\mathbf{e}$

can be determined by

$$\begin{aligned}\mathbf{v} &\leftarrow \alpha^2 \mathbf{v} + 4\tilde{\alpha}^2 \bar{\mathbf{f}}_{\mathbf{v}} + 4\alpha\tilde{\alpha} \bar{\mathbf{e}}_{\mathbf{v}} \\ \mathbf{e} &\leftarrow \alpha \mathbf{e} + 2\tilde{\alpha} \bar{\mathbf{f}}_{\mathbf{e}}\end{aligned}\tag{3.15}$$

It can be found that the composite **s-lifting** step is simply an expression of the generalized **s-lifting** step in (3.9). Similarly, the composite **w-lifting** step for each of the face points  $\mathbf{f}$  and each of the edge points  $\mathbf{e}$  has the following expression:

$$\begin{aligned}\mathbf{f} &\leftarrow \alpha^2 \mathbf{f} + 4\tilde{\alpha}^2 \bar{\mathbf{v}}_{\mathbf{f}} + 4\alpha\tilde{\alpha} \bar{\mathbf{e}}_{\mathbf{f}} \\ \mathbf{e} &\leftarrow \alpha \mathbf{e} + 2\tilde{\alpha} \bar{\mathbf{v}}_{\mathbf{e}}\end{aligned}\tag{3.16}$$

After one decomposition of 2D DWT is completed, the resulting  $\mathbf{v}$  is the scaling coefficients as the input of the next decomposition of 2D DWT. The resulting  $\mathbf{f}$  and  $\mathbf{e}$  are the wavelet coefficients of 2D DWT.

It can be found that (3.15) is involved with the average of four neighboring edge points and the average of four face points for all  $\mathbf{v}$ . If an extraordinary vertex exists with valence  $n_{\mathbf{v}}$ ,  $\bar{\mathbf{f}}_{\mathbf{v}}$  and  $\bar{\mathbf{e}}_{\mathbf{v}}$  of (3.15) can be generalized to the average of  $n_{\mathbf{v}}$  neighboring face points and the average of  $n_{\mathbf{v}}$  edge points, respectively. Therefore, the composite lifting steps in (3.15) and (3.16) can be performed no matter whether rows and columns are well-defined. It simply requires the structure of Catmull-Clark subdivision. The inverse lifting steps can be obtained similarly using (3.11) and (3.12).

In this study, the wavelet and scaling filters construction is based on dyadic refinement of linear B-spline scaling function. The lifting scheme of this wavelet construction based on linear B-spline scaling function is composed of only two composite lifting steps in each of 2D DWT decomposition: one composite **s-lifting** step followed by one composite **w-lifting** step. The parameters in (3.15) and (3.16) are  $\alpha = 1$ ,  $\tilde{\alpha} = -\frac{1}{2}$ ,  $\beta = 1$ , and  $\tilde{\beta} = \frac{1}{4}$ . Fig. 33 shows the scaling coefficients after one,

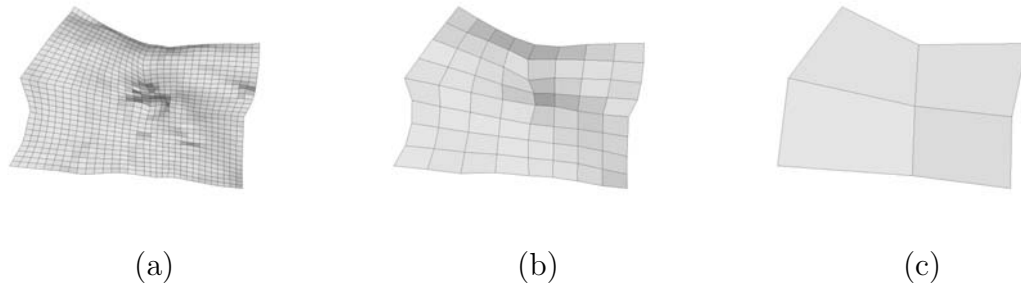


Fig. 33. DSWT of Fig. 28(d) (a) Scaling coefficients after one decomposition of DSWT. (b) Scaling coefficients after three decomposition of DSWT. (c) Scaling coefficients after five decompositions of DSWT

three, and five decompositions of Fig. 28(d) by using this new lifting scheme. Fig. 30(d)-(f) shows the scaling coefficients of another customized shape shown in Fig. 30(c), in which there is an extraordinary landmark with valence three. This example (shown in Fig. 30) demonstrates that DSWT of arbitrarily customized training shapes can be constructed accordingly.

### 3. Wavelet Distribution Model

Since the rank of covariance matrix  $\mathbf{C}_x$  in PDM is at most  $N - 1$ , the number of the valid principle axes corresponding nonzero eigenvalues is at most  $N - 1$ . Typically, it is the case that  $n \gg N$  in the 3D SSM. The number of the principle axes may not be sufficient enough to well-represent a shape with a large number of landmarks. Moreover, since each shape in PDM is a global linear combination of principle axes, PDM may not be able to capture fine shape details. Davatzikos *et al.* [60] first proposes multiscale SSM to solve this problem. Several studies applying different multiscale analysis to SSM are proposed such as spherical wavelet on spherical topology [61], subdivision based surface wavelet [62] on spherical topology, and diffusion wavelet on arbitrary surface topology [63].

In the following, DSWT will be incorporated with PDM to form a multiscale SSM. The training shapes in the model space are decomposed into multiscale representations, and a PDM is built in the subspace associated with each scale. This wavelet-based SSM is called wavelet density model (WDM). For simplicity of notation, all the scaling coefficients at 0-scale will be viewed as wavelet coefficients at  $(-1)$ -scale. Let  $\hat{\mathbf{w}}_{i,k,l}$  be DSWT of  $\tilde{S}_i$  at scale  $l$ , spatial location  $k$ , shape  $i$ . Define a collection of wavelet coefficients  $B_{i,l} = \{\hat{\mathbf{w}}_{i,k,l}, \forall k\}$  at each scale, and concatenate them to form  $\mathbf{w}_{i,l} \equiv (\hat{\mathbf{w}}_{i,0,l}^T, \hat{\mathbf{w}}_{i,1,l}^T, \dots)^T$ . Finally, PCA is performed on  $\mathbf{w}_{i,l}$  at each scale over all the training shapes to obtain the matrices  $\mathbf{P}_l$  of eigenvectors. A set of wavelet coefficients  $\tilde{\mathbf{w}}_l$  of a shape at specific scale  $l$  can be generated by a shape parameter  $\tilde{\mathbf{b}}_l$

$$\tilde{\mathbf{w}}_l = \bar{\mathbf{w}}_l + \mathbf{P}_l \tilde{\mathbf{b}}_l \quad (3.17)$$

Similarly, the wavelet coefficients  $\mathbf{w}_l$  of any shape at scale  $l$  can be approximated by projecting  $\mathbf{w}_l$  onto the subspace of  $\mathbf{P}_l$

$$\mathbf{w}_l \approx \bar{\mathbf{w}}_l + \mathbf{P}_l \mathbf{b}_l \quad (3.18)$$

with

$$\mathbf{b}_l = \mathbf{P}_l^T (\mathbf{w}_l - \bar{\mathbf{w}}_l) \quad (3.19)$$

It can be found that the total number of the eigenvectors in the model is increased by around  $J$  times. Similarly, the algorithm of minimizing (3.5) can be developed and is summarized in **Algorithm 5**.

#### 4. Image Feature Model

In addition to WDM, IMF is built by using training images and shapes (before performing Procrustes alignment) to describe the image features embedded on the landmarks in the image space. For each of the landmarks of  $S_i$  in the image space, a line

---

**Algorithm 5** A similar algorithm analogous to **Algorithm 4** when WDM is used.

---

$\mathbf{b}_l \leftarrow \mathbf{0}$

**while** Until convergence **do**

$\mathbf{w}_l \leftarrow \bar{\mathbf{w}}_l + \mathbf{P}\mathbf{b}_l$ ; generate wavelet coefficients in the model space using (3.17).

$\mathbf{x} \leftarrow \mathcal{W}^{-1}(\mathbf{w}_l)$ ; Calculate inverse DSWT of  $\mathbf{w}_l$ .

Calculate  $\mathcal{T}$  by minimizing  $\|\mathbf{y} - \mathcal{T}(\mathbf{x})\|^2$  using [57]

$\mathbf{x}' \leftarrow \mathcal{T}^{-1}(\mathbf{y})$ ; calculate inverse spatial transformation of  $\mathbf{y}$

$\mathbf{w}_l \leftarrow \mathcal{W}(\mathbf{x}')$ ; Calculate DSWT of  $\mathbf{x}'$

$\mathbf{b}_l \leftarrow \mathbf{P}_l^T(\mathbf{w}_l - \bar{\mathbf{w}}_l)$ ; calculate the shape parameters fitting  $\mathbf{w}_l$  using (3.19).

Apply shape constraints on  $\mathbf{b}_l$  analogous to (3.6)

**end while**

---

$\mathcal{L}$  passing through it and perpendicular to the shape is calculated [Fig. 34(a)]. Then  $\mathcal{L}$  is uniformly sampled to obtain a set of ordered  $2M + 1$  points  $\{z_m\}_{m=-M}^M$  ( $M$  points on each side). Image intensities along the line can be interpolated at each point  $z_m$ . Fig. 34(b) illustrates a set of the sampled points along  $\mathcal{L}$  and their image intensities. An image feature vector  $\mathbf{g}$  (such as first order derivative of image intensity) can be calculated using the interpolated image intensities. Let  $\bar{\mathbf{g}}$  and  $S_{\mathbf{g}}$  be the mean and covariance matrix of  $\mathbf{g}$  over all the training images. The IFM is characterized by  $\bar{\mathbf{g}}$  and  $S_{\mathbf{g}}$ .

In our study, three kinds of image features are calculated: zero order ( $\mathbf{g}^{(0)}$ ), first order ( $\mathbf{g}^{(1)}$ ), and second order ( $\mathbf{g}^{(2)}$ ) derivatives of image intensity.  $\mathbf{g}^{(i)}$  is normalized by  $\|\mathbf{g}^{(i)}\|$  in order to avoid the effect caused by non-calibration in CBCT imaging.

#### E. Base Invariant Wavelet Active Shape Model

Once the statistical models are built, we will calculate the outer surface of anterior wall of maxilla in a CBCT image by using statistical priors of the statistical models. In

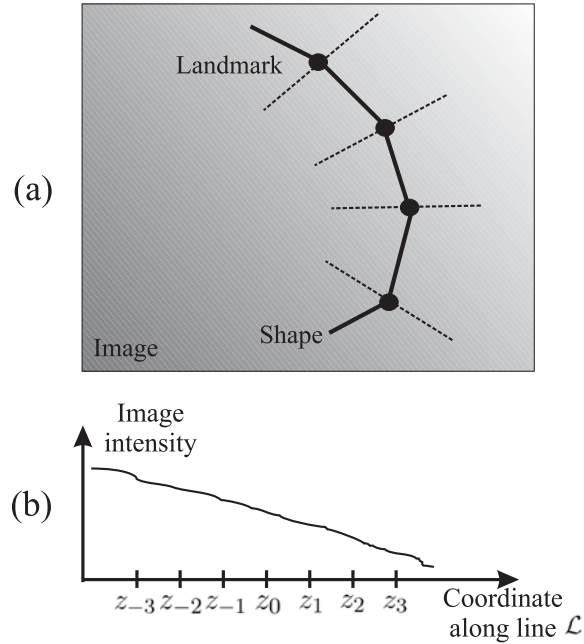


Fig. 34. The image profile in IFM. (a) At each of the landmarks, a line  $\mathcal{L}$  (dashed line) perpendicular to the training shape in the image space is defined for calculating the image feature. (b) The interpolated image profile on sample points along line  $\mathcal{L}$ . Without loss of generality,  $z_0$  is the landmark.

the following, we propose a novel model-based algorithm called base invariant wavelet active shape model (BIWASM) based on WDM with an initialization method called customized wavelet base initialization (CWBI) to calculate it. A brief flowchart is summarized in Fig. 35.

### 1. Preliminary Studies

In the following, we will introduce two model-based segmentation algorithms ASM and WASM and one of the most common initialization methods called RBI. ASM is introduced by Cootes *et al.* [64] and is an active contour iterative searching algorithm using PDM. WASM is the variation of ASM by applying multiscale analysis and is introduced in [60] using WDM. The final shape can be calculated by RBI followed by

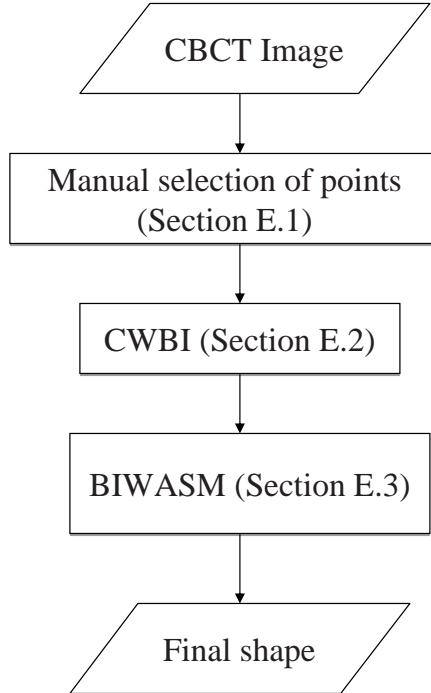


Fig. 35. The flowchart of performing the proposed CWBI and BIWASM.

two-step iterative shape searching of WASM (ASM) based on WDM (PDM).

RBI can be one of the most simple initializations for ASM and WASM. The mean shape  $\mathcal{W}^{-1}(\{\bar{\mathbf{w}}_l, \forall l\})^4$  [See (3.17)] in the model space can be viewed as the most probable shape for initialization. The initial shape can be obtained by transforming the mean shape from the model space to the image space. Therefore, RBI can be performed in two steps. The first step of RBI is to use user interaction to select a number of the points in the image space described in Appendix C. They correspond to control landmarks of the mean shape. The control landmarks of a shape are defined based on the construction of the training shape and are described as follows. In Fig.

---

<sup>4</sup>It can be shown that mean shapes of PDM and WDM are exactly the same given the same training shapes are used, i.e.  $\bar{\mathbf{x}}$  [See (3.2)] =  $\mathcal{W}^{-1}(\{\bar{\mathbf{w}}_l, \forall l\})$

28(a), 9 anatomical control landmarks of the training shape form a mesh at 0-th subdivision. After any level of subdivision is performed, new landmarks are added. It can be observed that these 9 landmarks exist in the remeshed training shape at each level of subdivision. We define these 9 landmarks as control landmarks of a shape. Fig. 36(a) shows these enumerated 9 control landmarks [they correspond to anatomical 9 control landmarks of the mesh at 0-th subdivision in Fig. 28(a)]. Therefore, there are 9 corresponding control landmarks in the mean shape. The selection of the points in RBI is based on the assumption: if we were able to know the true shape<sup>5</sup> (in the image space) composed of regularized landmarks with the same mesh structure as the shape in SSM, each of these selected points (in the image space) is assumed to be exactly one of the control landmarks on the true shape (in the image space). Furthermore, the selection criterion in RBI is the same as the configuration of anatomical control landmarks for training shapes demonstrated in Fig. 24(a). However, the datasets used for selection of the points are different: the points selected for calculation of initial shape are pinpointed on slices of the image using user interaction (Appendix C); and the points selected for patch decomposition and shape extraction in Section C.1 are pinpointed on the ground truth of bone surface. Two examples of point selection for calculation of initial shape in RBI are shown in Fig. 36(a) and Fig. 36(b). The first example is that we can select 4 points corresponding to 4 of the control landmarks (such as the corner control landmarks) of the mean shape (in the model space). The second example is that we can select 9 points corresponding to 9 control landmarks of the mean shape (in the model space). At the second step of RBI, a transformation from the model space to the image space can be calculated by registering these selected points (in the image space) and their corresponding control landmarks of the mean shape (in the model space). The initial

---

<sup>5</sup>The true shape means the most ideal shape

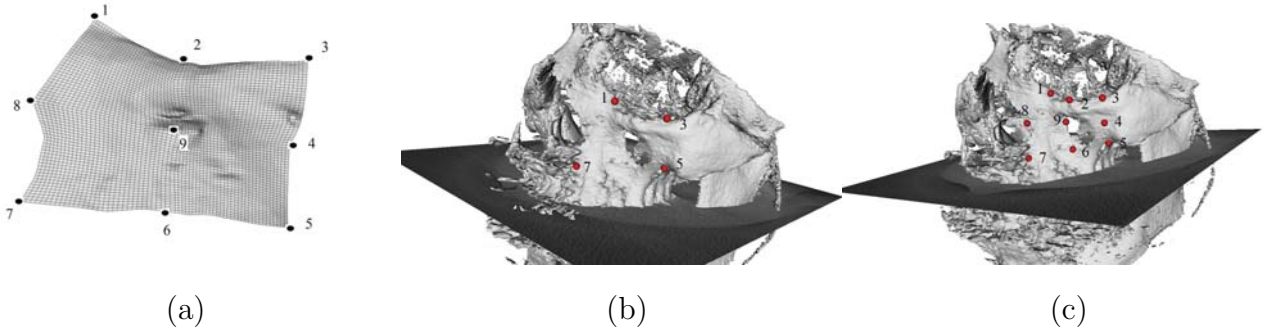


Fig. 36. Control landmarks of a shape. (a) Nine control landmarks of a shape are defined and derived from anatomical control landmarks of the mesh at 0-th subdivision in Fig. 28(a). (b) Four selected points using user interaction (Appendix C). These points with labeled numbers are assumed to be exactly the same as the corresponding (See the corresponding numbers) control landmarks of the true shape. (c) Nine selected points correspond to all the control landmarks of the true shape.

shape calculated by RBI using 9 selected points is illustrated in Fig. 37(a)

The first step of iterative shape searching of WASM (ASM) is that given a shape  $\tilde{\mathbf{y}}^{(k)}$  in the image space at the  $k$ th iteration, each candidate landmark is examined along the line passing through it and perpendicular to the evolving shape  $\tilde{\mathbf{y}}^{(k)}$  by using IFM. Similar to the notation in Section D.4, a set of ordered  $2K + 1$  points  $\{z_m\}_{m=-K}^K$  can be acquired along the line, where  $K > M$ . The image feature vector  $\tilde{\mathbf{g}} \equiv (g_{-K}, g_{-K+1}, \dots, g_K)$  with length  $2K + 1$  can be calculated. A searching window defining a temporary image feature vector  $\mathbf{g}_m \equiv (g_{-M+m}, g_{-M+m+1}, \dots, g_{M+m})$ ,  $m = -(K - M), \dots, (K - M)$  with length  $2M + 1$  scans the image feature vector  $\tilde{\mathbf{g}}$ . The candidate landmark  $z_{\hat{m}}$  can be selected among  $\{z_m\}_{m=-(K-M)}^{(K-M)}$  so that

$$\hat{m} = \arg \min_m f(\mathbf{g}_m) \quad (3.20)$$

Where  $f \equiv (\mathbf{g} - \bar{\mathbf{g}})^T S_{\mathbf{g}}^{-1} (\mathbf{g} - \bar{\mathbf{g}})$  is Mahalanobis distance evaluated at  $\mathbf{g}$ . The landmarks calculated by 3.20 form a new evolving shape  $\mathbf{y}^{(k)}$ .

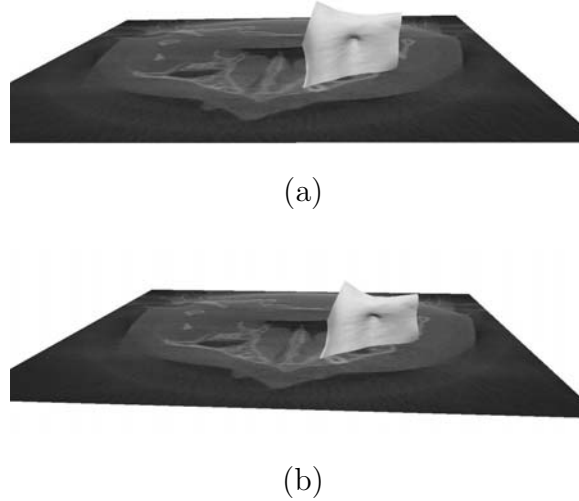


Fig. 37. The initial shapes. (a) The initial shape (accompanied with a slice in the image space) calculated by RBI using 9 selected points. (b) The initial shape (accompanied with a slice in the image space) calculated by CWBI using 9 selected points.

It can be observed that when the distribution of  $\mathbf{g}$  is assumed to be jointly Gaussian, (3.20) is equivalent to finding a image feature vector maximizing the probability of a joint Gaussian distribution and then assigning the center point of the optimal image feature vector  $\mathbf{g}$  to be the candidate point. However, this assumption is not appropriate in our study. Therefore, we set the covariance of image feature vector to be identity, i.e.  $S_{\mathbf{g}} = \mathbf{I}$ . Furthermore, a new evaluation function in (3.20) for candidate landmarks is defined as  $\tilde{f} \equiv f^{(0)} + f^{(1)} + f^{(2)}$  in our study, where  $f^{(i)}$  is Mahalanobis distance for image feature vector  $\mathbf{g}^{(i)}$

The second step of iterative shape searching of WASM (ASM) is to generate a shape in the model space and transform it to obtain a shape  $\tilde{\mathbf{y}}^{(k+1)}$  in the image space in order to fit  $\mathbf{y}^{(k)}$ .  $\tilde{\mathbf{y}}^{(k+1)}$  can be calculated by minimizing  $\|\tilde{\mathbf{y}}^{(k+1)} - \mathbf{y}^{(k)}\|^2$  using **Algorithm 5** (**Algorithm 4**). The algorithm of WASM (ASM) is summarized in **Algorithm 6**.

---

**Algorithm 6** WASM (ASM)

---

**while** Until convergence **do**

$\mathbf{y}^{(k)} \leftarrow \tilde{\mathbf{y}}^{(k)}$ ; calculate a candidate shape by examining the neighboring region of each of the landmark points.

$\tilde{\mathbf{y}}^{(k+1)} \leftarrow \mathbf{y}^{(k)}$  ; given  $\mathbf{y}^{(k)}$ , calculate  $\tilde{\mathbf{y}}^{(k+1)}$  by minimizing  $\|\tilde{\mathbf{y}}^{(k+1)} - \mathbf{y}^{(k)}\|$  using

**Algorithm 5** (for WASM) or **Algorithm 4** (for ASM).

**end while**

---

## 2. Customized Wavelet Base Initialization

Although RBI incorporated with user interaction can quickly generate an initial shape, this initial shape contains only information of the mean shape, i.e.  $\mathbf{b}_l = \mathbf{0}$  (in WASM) or  $\mathbf{b} = \mathbf{0}$  (in ASM). We will exploit the information of selected points to design a customized initial shape by using WDM.

Let  $S_b$  be the mesh formed by 9 selected points by using user interaction on slices of images illustrated in Fig. 36(c). Assume  $\mathbf{y}_b$  is the  $27 \times 1$  vector formed by concatenation of the coordinates of all the points in  $S_b$ . Define

$$f(\mathcal{T}, \mathbf{b}_l, \forall l) \equiv \|\mathbf{y}_b - \mathcal{T}(\tilde{\mathbf{x}}(\mathbf{b}_l, \forall l))\|^2 \quad (3.21)$$

where

$$\tilde{\mathbf{x}}(\mathbf{b}_l, \forall l) \equiv \mathcal{C}\left(\mathcal{W}^{-1}(\bar{\mathbf{w}}_l + \mathbf{P}_l \mathbf{b}_l, \forall l)\right). \quad (3.22)$$

$\mathcal{C}(\bullet)$  is the operator identifying the corresponding control landmarks from a shape in the model space and concatenating the coordinates of all the control landmarks to form a  $27 \times 1$  vector (same formation as  $\mathbf{y}_b$ ). Therefore,  $\tilde{\mathbf{x}}(\mathbf{b}_l, \forall l)$  is a  $27 \times 1$  vector.

To generate a better initial shape, we need to calculate optimal  $\mathcal{T}^*$  and  $\mathbf{b}_l^*, \forall l$  so

that (3.21) is minimized:

$$(\mathcal{T}^*, \mathbf{b}_l^*, \forall l) = \arg \min_{\mathcal{T}^*, \mathbf{b}_l^*, \forall l} f(\mathcal{T}, \mathbf{b}_l, \forall l) \quad (3.23)$$

The initial shape can be determined by

$$\tilde{\mathbf{y}}^{(0)} = \mathcal{T}^* \left( \mathcal{W}^{-1}(\bar{\mathbf{w}}_l + \mathbf{P}_l \mathbf{b}_l^*, \forall l) \right) \quad (3.24)$$

It can be observed that  $f(\mathcal{T}, \mathbf{b}_l, \forall l)$  is a non-linear function. We can use simulated annealing approach to solve it. However, this optimal searching approach is computationally expensive. Therefore, in this study, we propose a simple and efficient approach (CWBI) to estimate an initial shape as follows.

There are two observations for Catmull-Clark subdivision and DSWT of a training shape. The first observation is as follows. Each of the training shapes is remeshed using Catmull-Clark subdivision to generate landmarks [Fig. 28(d)]. To construct WDM, each of the remeshed shapes with regularized landmarks is aligned to the model space using Procrustes alignment and decomposed into scaling coefficients and wavelet coefficients by DSWT. Based on the construction of DSWT described in Section D.2, the scaling coefficients at each scale correspond to the landmarks at each level of subdivision (i.e. they have same mesh structure). For example, when the scale coefficients at coarsest scale [Fig. 33(c)] is reached, they correspond to the mesh at 0-th Catmull-Clark subdivision [Fig. 28(a)]. Although the mesh of the scaling coefficients at each scale and the remeshed training shape at its corresponding level of Catmull-Clark subdivision have the same mesh structure, they are defined in different ways: the former is in wavelet domain, and the latter is in the model space. The second observation is as follows. In each training shape, there are 8 vertices at the boundaries of the base mesh and one vertex at the central area of the base mesh [Fig. 28(a)]. Since the operation of Catmull-Clark subdivision on these 8 corresponding

vertices at the boundaries of the training shape cannot be well-defined using **Algorithm 3** at each level of subdivision, these vertices at the boundaries of the training shape are unchanged at each level of subdivision. Similarly, when the remeshed training shape is decomposed into wavelet coefficients and scaling coefficients, the corresponding 8 scaling coefficients at the boundaries of the scaling mesh cannot be well-defined using (3.15) at each scale. These 8 corresponding scaling coefficients at the boundaries of scaling meshes are kept unchanged during wavelet decomposition at each scale of DSWT. Therefore, the values of these 8 corresponding vertices at the boundaries of the training shape are unchanged at all levels of Catmull-Clark subdivision and the same as the values of the corresponding 8 scaling coefficients of scaling meshes at all scales of DSWT. For example, the values of 8 vertices at the boundaries of the mesh illustrated in Fig. 33(a) are exactly the same as the corresponding 8 scaling coefficients at the boundaries of the coarsest scaling mesh illustrated in Fig. 28(c). However, the values of the vertex at the central area of the mesh are usually not equal to the values of its corresponding scaling coefficient at the central areas of the coarsest scaling mesh.

Based on two observations above, we claim that there exists  $\mathbf{b}_l, l \geq 0$  so that the value of each element in  $\tilde{\mathbf{x}}(\mathbf{b}_l, \forall l)$  [see (3.22)] can be approximated by the value of each element in  $\bar{\mathbf{w}}_{-1} + \mathbf{P}_{-1}\mathbf{b}_{-1}$  given  $\mathbf{b}_{-1}$ :

$$\tilde{\mathbf{x}}(\mathbf{b}_l, \forall l) \approx \bar{\mathbf{w}}_{-1} + \mathbf{P}_{-1}\mathbf{b}_{-1} \quad (3.25)$$

Based on the assumption in (3.25), we reduce complexity of the problem in (3.23) by calculating

$$(\mathcal{T}^*, \mathbf{b}_{-1}^*) = \arg \min_{\mathcal{T}, \mathbf{b}_{-1}} \|\mathbf{y}_b - \mathcal{T}(\bar{\mathbf{w}}_{-1} + \mathbf{P}_{-1}\mathbf{b}_{-1})\| \quad (3.26)$$

(3.26) can be solved (approximately) using **Algorithm 4** without applying shape constraints. Let  $\mathcal{T}_b$  be the suboptimal transformation of (3.26). It will be used to

define a transformation between the model space and image space and will play an essential role in the proposed BIWASM. A new base in the model space is defined by

$$\tilde{\mathbf{x}}_b \equiv \mathcal{T}_b^{-1}(\mathbf{y}_b) \quad (3.27)$$

We define a new scaling coefficient  $\mathbf{w}_{-1,b}$  at the coarsest scale by assigning the values of  $\mathbf{w}_{-1,b}$  to be  $\tilde{\mathbf{x}}_b$ . Based on the similar assumption in (3.25), we claim that there exists  $\mathbf{b}_l, l \geq 0$  so that

$$\tilde{\mathbf{x}}_b \approx \mathcal{C}\left(\mathcal{W}^{-1}(\mathbf{w}_{-1,b} \cup \{\bar{\mathbf{w}}_l + \mathbf{P}_l \mathbf{b}_l, \forall l \geq 0\})\right) \quad (3.28)$$

By combining local details using the mean wavelet coefficients  $\{\bar{\mathbf{w}}_l, l \geq 0\}$  of WDM, the initial shape can be constructed by

$$\tilde{\mathbf{y}}^{(0)} = \mathcal{T}_b\left(\mathcal{W}^{-1}(\mathbf{w}_{-1,b} \cup \{\bar{\mathbf{w}}_l, l \geq 0\})\right) \quad (3.29)$$

**Algorithm 7** summarizes CWBI. Fig. 36(b) illustrates the initial shape generated by the proposed CWBI.

---

**Algorithm 7** Customized Wavelet Base Initialization (CWBI)

---

$\mathcal{T}_b \leftarrow (\mathbf{y}_b, \mathbf{P}_{-1}, \bar{\mathbf{w}}_{-1})$ ; use **Algorithm 4** to calculate the suboptimal transformation  $\mathcal{T}_b$  of (3.26) without shape constraints.

$$\tilde{\mathbf{x}}_b \leftarrow \mathcal{T}_b^{-1}(S_b)$$

$\mathbf{w}_{-1,b} \leftarrow \tilde{\mathbf{x}}_b$ ; define a new scaling coefficients  $\mathbf{w}_{-1,b}$  at the coarsest scale based on the assumption of (3.28) and set it equal to  $\tilde{\mathbf{x}}_b$ .

$$\mathbf{x} \leftarrow \mathcal{W}^{-1}(\mathbf{w}_{-1,b} \cup \{\bar{\mathbf{w}}_l, l \geq 0\})$$

$$\tilde{\mathbf{y}}^{(0)} \leftarrow \mathcal{T}_b(\mathbf{x})$$


---

### 3. Base-Invariant Wavelet Active Shape Model

In most of the studies, the shapes of subjects are closed surfaces such as spherical topology [45, 61, 65–68], open surfaces representing most of the whole subject [63, 69], and tubular topology [70]. The shape in our study is different. It is a partial surface in skull model and is a shape-customized open surface with closed boundary. We observe that WASM and ASM may become unreliable in order to recognize the corresponding partial surface in the skull model. At the first step of WASM and ASM, they recognize the topology of the true partial shape by searching for the topology of neighboring candidate landmarks. The candidate landmarks at the boundary of this open surface are most likely to be out of the true shape (such as the parts of maxilla near nasal bones and orbits). Once the candidate landmarks out of the true shape, the evolving shape at the second step of WASM and ASM will erroneously fit these candidate landmarks. This is because WASM and ASM are involved with update of  $\mathcal{T}$  from the model space to the image space. Therefore, it is necessary to incorporate selected points  $S_b$  defined in Section E.2 to constrain the evolving shape.

Based on the concept in Section E.2, we design a new model-based algorithm (BIWASM) based on WDM to overcome this problem. It is similar to WASM, but the differences are described as follows. First, the transformation between model space and image space is no longer be calculated during the iterative steps.  $\mathcal{T}_b$  in (3.27) is used to define this invariant transformation. Second, the coarsest scaling coefficients  $\mathbf{w}_{-1,b}$  will be used instead of generating a new coarsest scaling coefficients  $\mathbf{w}_{-1}$  using (3.17). Third, to keep the evolving shape constrained by the selected points  $S_b$ , the control landmarks of the evolving shape corresponding to  $S_b$  in the image space will be unchanged during the iteration of BIWASM. The proposed BIWASM is summarized in **Algorithm 8**.

---

**Algorithm 8** Base Invariant Wavelet Active Shape Model (BIWASM)
 

---

$(\tilde{\mathbf{y}}^{(0)}, \mathcal{T}_b, \mathbf{w}_{-1,b}) \leftarrow (\mathbf{y}_b, \mathbf{P}_{-1}, \bar{\mathbf{w}}_{-1})$ ; use **Algorithm 7** to calculate the initial shape, the transformation, and scaling coefficients at the coarsest scale.

**while** Until convergence **do**

$\mathbf{y}^{(k)} \leftarrow \tilde{\mathbf{y}}^{(k)}$ ; calculate a candidate shape by examining the neighboring region of each of the landmark points, and the corresponding control landmark points in  $\mathbf{y}^{(k)}$  are replaced with  $S_b$ .

$\mathbf{x}' \leftarrow \mathcal{T}_b^{-1}(\mathbf{y}^{(k)})$ ; calculate inverse transformation of  $\mathbf{y}^{(k)}$

$\mathbf{w}_l \leftarrow \mathcal{W}(\mathbf{x}')$ ; DSWT.

$\mathbf{b}_l \leftarrow \mathbf{P}_l^T(\mathbf{w}_l - \bar{\mathbf{w}}_l), l \geq 0$ ; calculate the shape parameter fitting  $\mathbf{w}_l$  using (3.19).

Apply the constraints on  $\mathbf{b}_l, l \geq 0$  using (3.6)

$\mathbf{w}_l \leftarrow \bar{\mathbf{w}}_l + \mathbf{P}\mathbf{b}_l, l \geq 0$ ; generate wavelet coefficients using (3.17)

$\mathbf{x} \leftarrow \mathcal{W}^{-1}(\mathbf{w}_{-1,b} \cup \{\mathbf{w}_l, l \geq 0\})$ ; inverse DSWT.

$\tilde{\mathbf{y}}^{(k+1)} \leftarrow \mathcal{T}_b(\mathbf{x})$ ;

**end while**

---

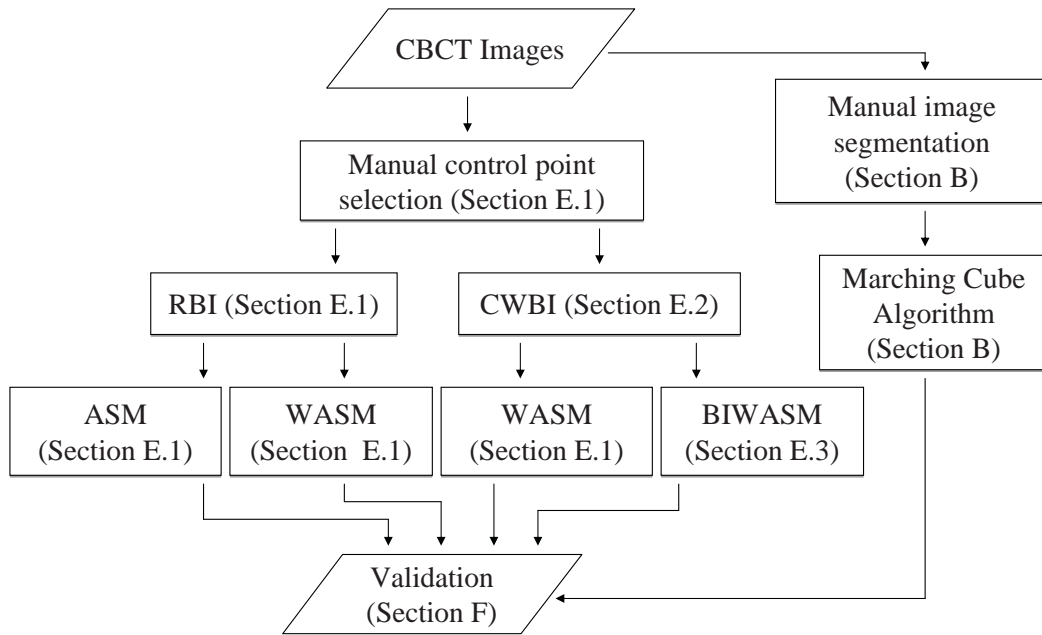


Fig. 38. The flowchart of data preparations.

## F. Validations and Results

Nineteen sets of CBCT images were used for the validation. Their ground truths of bone surface were manually established as described in Section B. They served as a control group. The outer surfaces of anterior wall of maxilla, illustrated in Fig. 22, were segmented using our BIWASM with CBWI. The same images were also segmented using ASM with Registration-Based Initialization (RBI), WASM with RBI, and WASM with CWBI, respectively. They all served as an experimental group.

## 1. Data Preparation

The segmentation dataset, referred as the datasets to test segmentation approaches, were labeled  $D_i, i = 1, 2, \dots, 19$ . Each of the segmentation datasets  $D_i$  consisted of a set of CBCT volumetric images (target datasets) and its corresponding ground truth of bone surface. The model datasets, referred as the training datasets in the base invariant active shape model, were defined by 19 shapes and 19 sets of CBCT volumetric images. They were labeled  $M_i, i = 1, 2, \dots, 19$  in the same order. Those 19 shapes were extracted from 19 ground truths of bone surface and were decomposed into patches using the approaches described in Section C.1. Nine anatomical control landmark points were pinpointed to form four patches in each of the shapes as illustrated in Fig. 24(a) and (b). The patches in each of the shapes were parameterized (Section C.2), subdivided five times, remeshed, and stitched to form a remeshed shape (Section C.3) with 4225 regularized landmarks (illustrated in Fig. 28(d)).

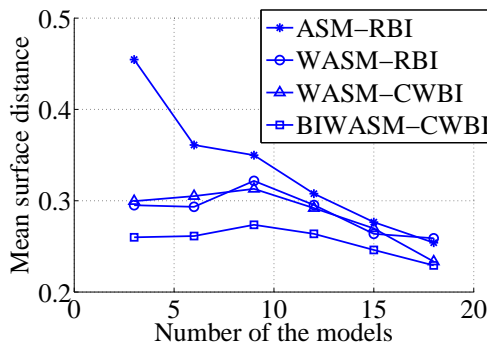
Once  $N$  model datasets were built as training datasets, one segmentation (target) dataset, other than  $N$  model datasets, was used to compare our developed approaches to the three traditional approaches. The preparation of target dataset was completed in the following four steps and summarized in Fig. 38. *Step 1* was landmark digitization. Nine control landmarks were digitized interactively as described in Section E.1 for initialization. They were selected based on the same criterion as control landmarks illustrated in Fig. 24(a). A set of 9 landmarks was digitized in each segmentation dataset. Once digitized, these landmarks were used for all the experiments. *Step 2* was initialization. The digitized control landmarks were used to create two initial shapes using two initialization methods: RBI and our newly developed CWBI. RBI was used to register these selected control landmarks of the shapes in the image space and their corresponding control landmarks of mean shape in the model space, and to transform the mean shape in the model space into the image space. The resulted

initial shape served as the input of ASM and WASM. CWBI was used to calculate a transformation between the image space and the model space by using those 9 selected points. It was also used to add the mean local details using WDM to obtain an initial shape. The resulted initial shape served as the input of WASM and BIWASM. *Step 3* was to calculate the final shapes. The shapes initialized by RBI were fed into ASM and WASM approaches respectively, resulting in ASM-RBI and WASM-RBI final shapes. They represented the final shapes calculated by the traditional approaches. In addition, the shapes initialized by CWBI were fed into WASM approach and our newly developed BIWASM approaches respectively, resulting in WASM-CWBI and BIWASM-CWBI final shapes. While WASM-CWBI shape represented the outcome generated using our initialization and the traditional segmentation approaches, the latter represented the outcome generated using both our developed initialization and final segmentation approaches. During the computation, the number of the iterations in ASM and WASM approaches (**Algorithm 6**) is 20. The number of the iterations in BIWASM (**Algorithm 6**) is 20. The maximum number of the iterations in **Algorithm 4** is 40, and 10 in **Algorithm 5**. We intentionally reduce the maximum iterative number in **Algorithm 5** to 10 instead of 40. This was because DSWT was computationally expensive. In all of ASM, WASM, and BIWASM approaches, 23 points ( $K = 12$ ) were sampled along a line perpendicular to landmarks in order to exam neighboring region and find candidate landmarks. The sample distance was 0.2mm. In addition, the shape constraints were  $a = 3$  for both  $\mathbf{b}$  in PDM and  $\mathbf{b}_l$  in WDM. This step produced four kinds of final shapes: ASM-RBI, WASM-RBI, WASM-CWBI, and BIWASM-CWBI. *Step 4* was to compare the ground truth to the final shapes generated by different approaches. It was done by calculating surface deviations, the closest distances, and Hausdorff distance between the ground truths and the final shapes generated in step 3. Surface deviation was a set of the closest

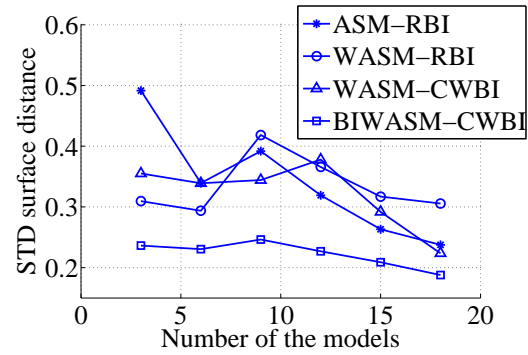
distances between the landmarks of the ground truth and the final shape. Hausdorff distance was also calculated. Therefore, there were 4225 surface distances and one Hausdorff distance produced from each target dataset. The validation was achieved by two sets of comparisons. In the following, the first set of the comparisons was to detect the variabilities amongst 4 approaches when the number of training datasets was static. The second set of comparisons was to detect the variabilities amongst 4 approaches when the number of training datasets was dynamic. In addition, the computational times were also compared amongst the 4 approaches.

The first set of comparisons was conducted using leave-one-out arrangement (cross validation). Six groups (total of 69) leave-one-out experiments were conducted:  $i = 1, 2, \dots, 19$  (19 experiments),  $i = 1, 2, \dots, 16$  (16 experiments),  $i = 1, 2, \dots, 13$  (13 experiments),  $i = 1, 2, \dots, 10$  (10 experiments),  $i = 1, 2, \dots, 7$  (7 experiments),  $i = 1, 2, \dots, 4$  (4 experiments). The dataset was randomly selected using SPSS software. In each experiment, the target dataset was excluded from the training datasets. For example, in the second group, the experiment of the datasets  $i = 1, 2, \dots, 16$  was conducted using  $M_i, i = 1, 2, \dots, 11, 13, \dots, 16$ , and the target  $D_{12}$  dataset was excluded from the training dataset. After final shapes were generated by four approaches (ASM-RBI, WASM-RBI, WASM-CWBI, BIWASM-CWBI), they were compared to their ground truths. In each of the six groups of experiments, the mean and standard deviation of surface distances were calculated over 80275 ( $19 \times 4225$ ), 67600 ( $16 \times 4225$ ), 54925 ( $13 \times 4225$ ), 42250 ( $10 \times 4225$ ), 29575 ( $7 \times 4225$ ), and 16900 ( $4 \times 4225$ ) surface distances, respectively. The mean Hausdorff distances was also calculated over the 19, 16, 13, 10, 7 and 4 final shapes, respectively. The results are shown in Fig. 39 (a)-(c).

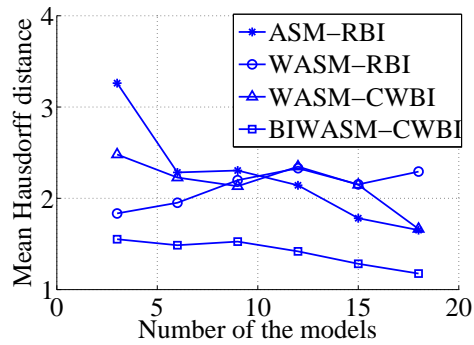
The second set of comparisons was conducted by using 13 segmentation datasets  $D_i, i = 1, 2, \dots, 13$  and varying the number of model datasets by 12, 15, and 18.



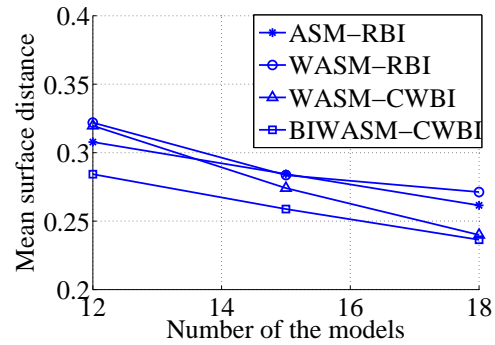
(a)



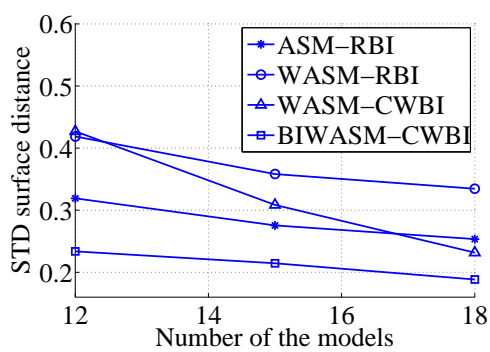
(b)



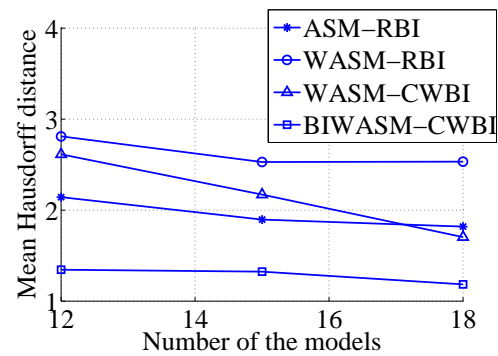
(c)



(d)



(e)



(f)

Fig. 39. (a), (b), and (c) are mean surface distances, standard deviation of surface distances, and mean Hausdorff distances in the first set of the experiments. (d), (e), and (f) are mean surface distances, standard deviation of surface distances, and mean Hausdorff distances in the second set of the experiments.

The dataset was also randomly selected using SPSS software. Three groups of the datasets were used to conduct 39 experiments. Again, the target dataset was excluded from the training datasets. The first group of the datasets were  $D_i, i = 1, 2, \dots, 13$  and  $M_i, i = 1, 2, \dots, 13$ . Each experiment was conducted by choosing one segmentation dataset from  $D_i, i = 1, 2, \dots, 13$ , and the rest 12 model datasets from  $M_i, i = 1, 2, \dots, 13$ . The second group of the datasets were  $D_i, i = 1, 2, \dots, 13$  and  $M_i, i = 1, 2, \dots, 16$ . Each experiment was conducted by choosing one segmentation dataset from  $D_i, i = 1, 2, \dots, 13$ , and the rest 15 model datasets from  $M_i, i = 1, 2, \dots, 16$ . The third group of the datasets were  $D_i, i = 1, 2, \dots, 13$  and  $M_i, i = 1, 2, \dots, 19$ . Each experiment was conducted by choosing one segmentation dataset from  $D_i, i = 1, 2, \dots, 13$ , and the rest 18 model datasets from  $M_i, i = 1, 2, \dots, 18$ . In each group, 13 experiments were conducted using each segmentation approach, respectively. Means and standard deviations of surface distances were calculated over 54925 ( $13 \times 4225$ ) surface distances, respectively. The mean Hausdorff distances were also calculated over the 13, 13, and 13 final shapes, respectively. The results are shown in Fig. 39 (d)-(f).

## 2. Results

The results (Fig. 39) showed that our BIWASM-CWBI approach outperformed the others in each of six groups (the first set of comparisons) and in each of three groups (the second set of comparisons). It also indicated that the more accurate result was achieved with more training dataset. The results indicated that our BIWASM-CWBI approach was capable of capture the outer surface of thin bones (1mm) in the skull model. Fig. 40 shows the visualization of the evolving shapes and the ground truth in a single experiment. This single experiment was in the first set of experiment based on  $D_i$  and  $M_i, i = 1, 2, \dots, 16, 18, 19$ .

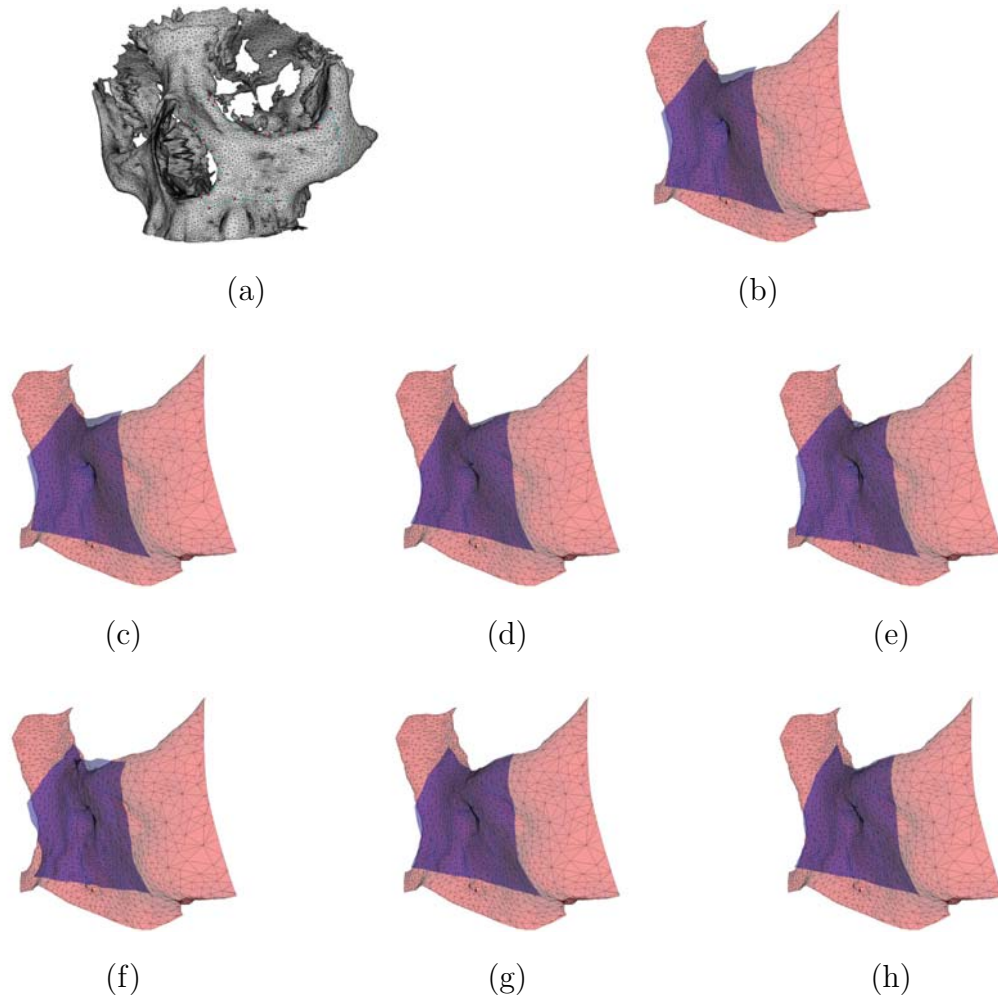


Fig. 40. The initial and final shapes (blue meshes) calculated by four approaches using the segmentation dataset ( $D_{17}$ ) and 18 model datasets. (a) The left half of the anterior surface of the skull is segmented and extracted manually from the ground truth of bone surfaces to validate the results. It is visualized as the red mesh in the rest of the subfigures. (b) and (e) are the initial and final shapes in ASM-RBI, respectively. (c) and (f) are the initial and final shapes in WASM-RBI, respectively. It can be found (b) and (c) are the same when they are calculated using RBI under PDM and WDM. (d) is the initial shape in both WASM-CWBI and BIWASM-CWBI. The final shapes in WASM-CWBI and BIWASM-CWBI are shown in (g) and (h), respectively.

Table VI. The Computation Times in the First Experiment

ASM-RBI	WASM-RBI	WASM-CWBI	BIWASM-CWBI
164s	575s	618s	205s

Finally, the computational times of the 4 approaches are presented in Table VI. This was calculated in the first set of experiment based on  $D_i$  and  $M_i, i = 1, 2, \dots, 16, 18, 19$ . The computer was Intel i7 2.8Hz with 4G RAM. The result revealed that the computational time of our approach was comparable with that of ASM-RBI and significantly shorter than WASM-RBI and WASM-CWBI.

#### G. Discussion

The correspondence of landmarks over all the training shapes can be properly constructed structurally and geometrically by using patch decomposition and mesh subdivision. In Section C, the training shapes are extracted from ground truths of bone surfaces. Each of the training shapes is partitioned into several polygon-like patches. These patches can be customized according to anatomical structures of the training shapes. When the boundaries of patches are chosen along high curvature ridges and edges of the training shapes, structural shape correspondence is created. When each of the patches is characterized by smooth surface and barely has prominent features, the correspondence of landmarks among the corresponding patches can be constructed geometrically by regular subdivision. The shape correspondence constructed by patch decomposition and regular subdivision can be done in a short time compared to the description length approach for model building in [68]. This approach may take hours to days to build a 3D SSM.

The shortest path used to create boundaries of patches is different from other studies. In [65, 71–73], they use Dijkstra’s algorithm to define patches. It will lead to zigzag boundaries along the patches. Barycentric mapping used to calculate parameterization of patches is simple and fast. It requires the boundary of a patch to be fixed onto a convex topology. However, if the boundary of the convex topology cannot reflect the 3D boundary of the patch, high distortion on parameterization mapping will occur near the boundary [74]. Therefore, the shortest path calculation we apply in the study can prevent it since the patch boundary resembles straight lines on the mesh. Regarding the computational time of shortest path calculation in our study, the calculation of each shortest path in Fig. 24 (b) requires from 2s to 5s. Hence, patch decomposition on each of the training shapes used in our study can be completed in less a minute.

WDM provides more dimensions and captures more local features to model a shape than PDM. However, it does not mean WASM can always outperform ASM. We will have two observations from the results to demonstrate it. First, it can be found in the studies of Davatzikos *et al.* [60] and Nain *et al.* [61] that there are no significant differences of mean distance between ASM and WASM in occasional circumstances when the number of the models are increased. Our results also demonstrate the point. The mean distances in ASM-RBI and WASM-RBI have no significant differences when at least 15 models are used [shown in Fig. 39 (a) and (d)]. Second, the STD distance and Hausdorff distance in WASM-RBI are larger than that in ASM-RBI. By visualizing the results on a single case in Fig. 40, the shape at the boundary is distorted in both WASM-RBI and ASM-RBI. WASM-RBI has higher dimensions to capture this distortion while ASM-RBI has fewer dimensions to capture it (instead, ASM-RBI constrains it). Therefore, ASM-RBI has smaller Hausdorff distance than WASM-RBI. Since WASM-RBI still captures local details better than ASM-RBI, it

is explained that the range (STD) of surface distance in WASM-RBI can be larger than that in ASM-RBI.

According to the results shown in Fig. 39, our approach BIWASM-CWBI can achieve mean surface distance as low as  $0.25mm$  and standard deviation of surface distance less than  $0.2mm$ . Due to the limitation of CBCT, transition of image intensities from soft tissues to bone is very smooth. The thinnest visible anterior wall in CBCT image can be as small as  $1mm$ <sup>6</sup>. It means that our approach can capture the outer surface of maxillary thin bones without significant loss of the shapes in the skull model. Quantitatively, we can expect our BIWASM-CWBI incurs  $0.25 \pm 0.2$  surface errors when performing any kinds of surgical planning and simulations in CASS system. Based on our clinical experience and published literature [15, 75–77], there would be no clinical significance if the surface error is less than  $0.5mm$ . Therefore, we demonstrate that our approach BIWASM-CWBI is robust in building CBCT skull model for CASS.

---

<sup>6</sup>This measurement is based on our experiences on CBCT datasets. The real bone thickness of anterior maxillary walls can be smaller than  $1mm$ .

## CHAPTER IV

REGION OF INTEREST RECONSTRUCTION AND DOSE REDUCTION  
ESTIMATION IN COLLIMATED CONE-BEAM COMPUTED TOMOGRAPHY  
IMAGING\*

## A. Introduction

Circular scanning cone-beam computerized tomography (CBCT) with C-arm flat panel detectors (FPD) has become a prevalent 3-dimensional (3D) imaging system for clinical application. Its fast acquisition of 2-dimensional (2D) projections and reconstruction of 3D volumetric image allow the feasibility of interventional radiology procedures [78]. The mobile C-arm system provides full access to patient without detrimentally repositioning in the operating room. Advanced post-processing such as scatter correction, beam hardening correction, truncation correction, and ring correction has been developed for achieving low contrast imaging of CBCT instead of increasing radiation dose for the same contrast resolution [79].

Because the x-ray tube in CBCT generates rays in all directions, collimators are used for eliminating unnecessary x-ray beams outside the field of view (FOV) where imaging is not necessary and reducing scatter effect; the last proved to degrade image quality [80]. They restrict the x-ray beams such that the FOV exactly fits the whole area of FPD. When imaging a large object such as the body core, this may cause mild truncation on projection data. The object is entirely visible at several views of the x-ray tube, but truncation occurs at the other views. The reconstruction leads

---

\*Part of the content described in this chapter is reprinted with permission from "Dynamically collimated c-arm flat panel detector CT imaging for focused region-of-interest reconstruction and radiation dose reduction" by S. Fung, Y. B. Chang, R. Pino, E. Hui, X. Zhou, M. Alvarado, G. Benndorf, M. diaz, R. Klucznik, Z. Xiong, S. Wong, and K. Li, 2011, *Proc. of ASNR 49th Annual Meeting*, Seattle, WA, Copyright 2011 by ASNR

to bright band artifacts extending inside scan FOV and incorrect image intensity around the edges of scan FOV while part of reconstructed image is not distorted [81]. A number of truncation correction techniques have been proposed in [82–86].

Collimators can be designed as variable diaphragms including two movable pieces of lead in the longitudinal direction (perpendicular to the plane of the circular trajectory) and two in the transverse direction (tangential to the circular trajectory). This design makes region of interest (ROI) imaging available in CBCT, and imaging a desired region of the patient becomes on demand in order to reduce the radiation dose exposure to both patients and surgeons. As the collimators customize a FOV to fit a ROI completely encompassed in the patient, projection images at all views contain truncations. This situation is well-known as the interior problem and is not solvable by general analytical reconstruction approaches. Although some studies have discussed the capability of other reconstruction algorithms on this problem [87–89], the truncation correction technique may be an alternative and practical approach to help reconstruct ROI image if the image quality remains acceptable. The purpose of this prospective study was to investigate the feasibility of imaging as a small ROI as possible using collimators and to estimate the amount of reduction on radiation dose for CBCT system.

## B. Materials and Methods

### 1. CBCT Imaging System and Collimators

The CBCT imaging was based on the C-arm FPD system (Siemens Medical Solutions, Forchheim, Germany), and the physical specifications of the CBCT system are shown in Table VII. Fig. 41 illustrates the geometry of the CBCT system with collimators. The collimators are between the object and the x-ray source and are made of lead with a thickness of 5mm. They can be adjusted transversely and longitudinally to

Table VII. Physical Specifications of the CBCT System.

Source-to-detector distance	1200mm
Source-to-isocenter distance	750mm
Size of the detector	$300 \times 400\text{mm}^2$
Size and resolution of projection images	$1240 \times 960$ ( $0.308\text{mm} \times 0.308\text{mm}$ )
Number of projections	543
Scan angle	$220^\circ$
Scan time	20s

customize an open rectangular area according to the ROI. Since the lead shield with a thickness of 1.1 mm can attenuate 100 kV x-ray beams to 0.1% [90], these lead-made collimators are enough to reduce the intensity of x-ray beams close to zero. The full field imaging is expressed as "without collimation" when the open area is large enough to allow the x-ray beams to be projected onto the full field of the detector. In contrast, "with collimation" means the collimators are adjusted to customize a smaller open area such that only the ROI is imaged. The transverse length and longitudinal width of rectangular projection images customized by collimators are defined as  $C_t$  and  $C_l$ , respectively. The projection images were stored in integers with a range of [32,4096].

## 2. ROI Reconstruction Using Truncation Correction

Cylindrical polystyrene phantom with 30mm diameter and 25mm height is used as the object in the ROI and water as the background. The cylindrical polystyrene was

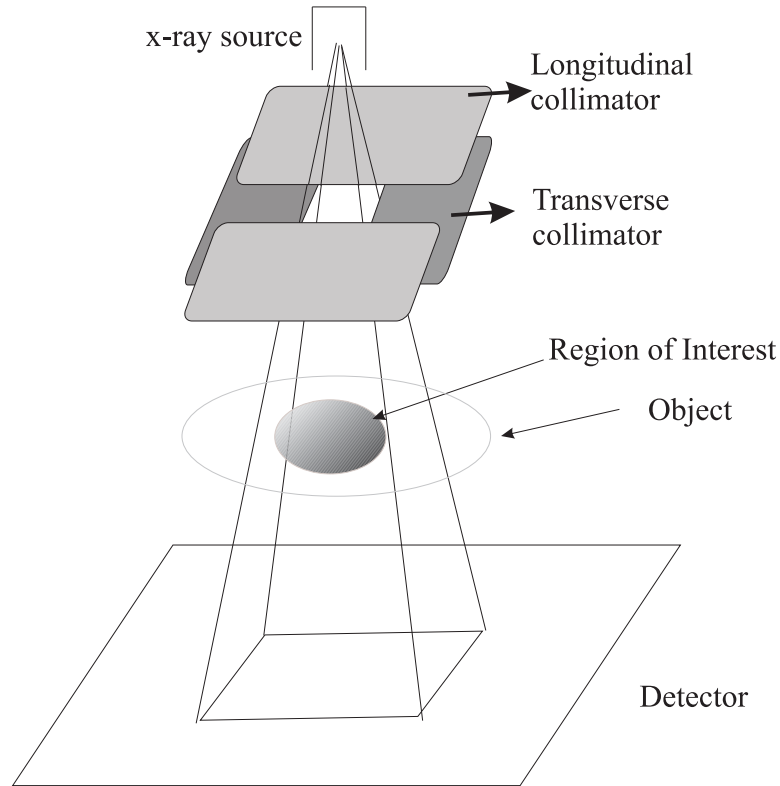


Fig. 41. ROI imaging with movable collimators. The longitudinal collimators can be adjusted in the longitudinal direction, and the transverse collimators in the transverse direction. The open area is customized according to the size of ROI.

stack above a cylindrical plastic water phantom with the same size inside a water tank. These materials and background provide constant attenuation coefficients which can clearly show the variation of ROI images. The projection of the cylindrical polystyrene was in the isocenter of the detector at all views. Three experiments were done: the first was "without collimation", and the other two were "with collimation"; they are with  $C_t = 150\text{mm}$ ,  $C_l = 83\text{mm}$ , and with  $C_t = 110\text{mm}$ ,  $C_l = 77\text{mm}$ . The last experiment "with collimation" was conducted with the smallest ROI such that the projection of the cylindrical polystyrene exactly fits FOV at all views. First, the projection data was exported from the CBCT system for truncation compensation.

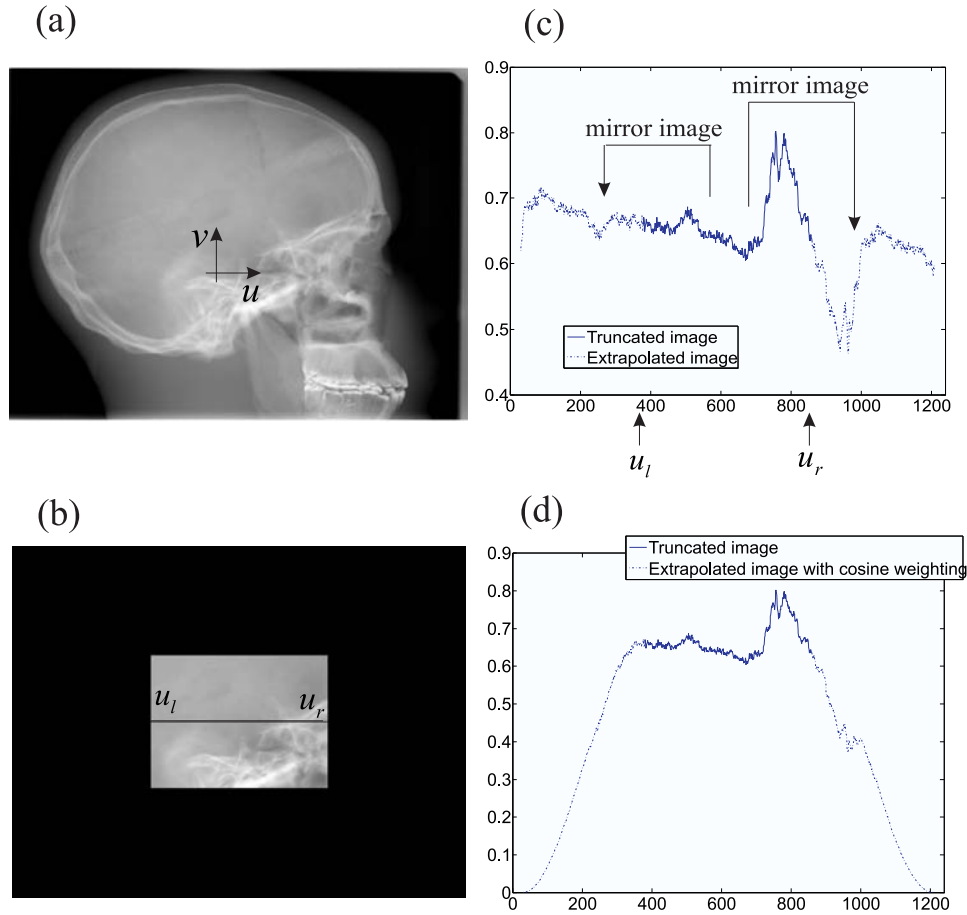


Fig. 42. Illustration of truncation correction. (a) The projection image without truncation and the coordinate definition. (b)  $u_r$  and  $u_l$  are the edges of the truncated projection. (c) Extrapolation with mirror symmetry. (d) Cosine weighting.

The intensity of the truncated part of projections is assumed to be 3300 in a range of [32,4096]. The truncation correction technique is designed as following. Let  $P_k(u, v)$  be the  $k$ -th projection image with  $u-v$  coordinate, as shown in Fig. 42(a), and assume it has been converted to an accumulated attenuation projection from intensity-based on the detector. For simplicity, the index  $k$  of  $P_k(u, v)$  is ignored. The projection truncated due to reduced FOV [as illustrated in Fig. 42(b)] is expressed as

$$P_{FOV}(u, v) = \begin{cases} 0 & u > u_r \\ 0 & u < u_l \\ P(u, v) & u_l \leq u \leq u_r \end{cases} \quad (4.1)$$

where  $u_r$  and  $u_l$  are determined by the right and left edges of the truncated projection  $P_{FOV}(u, v)$ . The lengths for extrapolations at the both sides are  $N_r$  and  $N_l$ , where  $0 < N_l, N_r < u_r - u_l$ . Based on the symmetric mirroring extrapolation technique [83], the extrapolated projection (Fig. 42(c)) is

$$P_{ex}(u, v) = \begin{cases} (2P_{FOV}(u_r, v) - P_{FOV}(-u + 2u_r, v)) & N_r + u_r \geq u > u_r \\ (2P_{FOV}(u_l, v) - P_{FOV}(-u + 2u_l, v)) & u_l - N_l \leq u < u_l \\ P_{FOV}(u, v) & u_l \leq u \leq u_r \\ 0 & \text{otherwise.} \end{cases} \quad (4.2)$$

Assume the image variation in ROI is small compared with the magnitudes of  $P_{FOV}(u_r, v)$  and  $P_{FOV}(u_l, v)$ . This assumption, in general, is held for a small ROI imaging of a body or head. Therefore, the extrapolated projection  $P_{ex}(u, v)$  is positive under this assumption:

$$P_{FOV}(u_r, v) > |P_{FOV}(u_r, v) - P_{FOV}(-u + 2u_r, v)| \quad (4.3)$$

$$P_{FOV}(u_l, v) > |P_{FOV}(u_l, v) - P_{FOV}(-u + 2u_l, v)| \quad (4.4)$$

To obtain smooth transition of the extrapolated data to zero,  $P_{ex}(u, v)$  is weighted by

$$w(u, v) = \begin{cases} \frac{1}{2} \left( 1 + \cos \left( \frac{\pi(u-u_r)}{N_r} \right) \right) & u > u_r \\ 1 & u_l \leq u \leq u_r \\ \frac{1}{2} \left( 1 + \cos \left( \frac{\pi(u-u_l)}{N_l} \right) \right) & u < u_l \end{cases} \quad (4.5)$$

The weighted extrapolation is illustrated in Fig 42(d). The extrapolation lengths  $N_r$  and  $N_l$  are assumed to be half of  $C_t$ . Secondly, the processed projection data was imported back to the CBCT system. Finally, the Feldkamp, Davis, Kress (FDK) reconstruction algorithm [91] with ring correction, scatter correction, and overexposure correction was performed in the CBCT system.

### 3. Analytical Reconstruction in Collimated ROI Imaging

The imaged object was a head phantom (Phantom Laboratory) with tissue-like material and bones. Two experiments were conducted. One was "without collimation" imaging, and the other was "with collimation" imaging with  $C_t = 130\text{mm}$  and  $C_l = 130\text{ mm}$ , respectively. The projection images were scaled to  $[0,1]$ . The correction of the noncircular C-arm imaging gantry is not calculated before the reconstruction. Two reconstruction algorithms were performed in the computer simulation. The one is the FDK reconstruction algorithm of filtered-backprojection (FBP), the other is  $\pi$ -line backprojection-filtration (BPF) algorithm [92]. The details implementing the  $\pi$ -line BPF algorithm are provided in Appendix D.

### 4. Evaluation of Radiation Dose Reduction

An "entrance dose" of x-rays is the dose absorbed at the skin surface, where x-ray beams enter. When x-ray beams enter the body, a small number of beams exit the body on the opposite side, where the detector is exposed. The rest of beams that never exit from the body are absorbed as extra energy by the body's internal organs and bones. In Fig. 43(a), there is a virtual plane between the collimators and the patient. This virtual plane is parallel to the detector and close to the top of the patient. It could be viewed as a virtual entrance of x-ray beams when they are about to enter the patient body. The entrance dose is defined as energy of x-ray beams

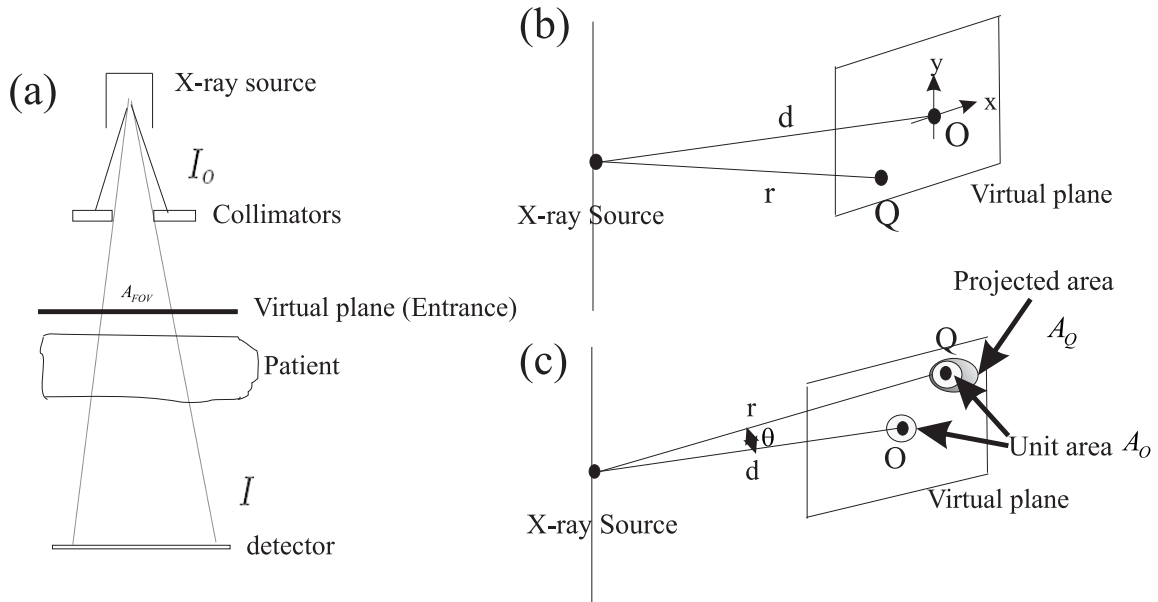


Fig. 43. Entrance dose calculation. (a) The virtual entrance plane is defined at the top of the patients. (b) The geometry of projection onto the virtual plane. (c) The illustration of obliquity effect.

passing through the virtual plane. Let the x-ray intensity be a unit of energy per unit area, and  $E_s$  the energy obtained by integrating the x-ray beam intensity with a small sphere surrounding the x-ray source. In Fig. 43(b),  $d$  is the source-to-virtual-plane distance,  $O$  is the origin of the coordinate system of the virtual plane,  $r$  is the distance between the source, and  $Q$  is an arbitrary point on the virtual plane. The intensity  $I_O$  at the point  $O$  is given by

$$I_O = \frac{E_s}{4\pi d^2} \quad (4.6)$$

where  $4\pi d^2$  is the surface area of a sphere with radius  $d$ . Assume that the coordinate of the point  $Q$  is  $(x, y)$ . The intensity  $I_Q$  at  $Q$  is

$$I_Q = \frac{E_s}{4\pi(d^2 + x^2 + y^2)}. \quad (4.7)$$

From (4.6) and (4.7),  $I_Q$  becomes

$$I_Q = I_O \frac{d^2}{4\pi(d^2 + x^2 + y^2)}. \quad (4.8)$$

The obliquity effect takes place because the surface of the detector is not perpendicular to the direction of x-ray beams propagation. In Fig. 43(c), the x-ray beams perpendicularly pass through the origin  $O$  of the virtual plane.  $A_O$  denotes the cross-section unit area of the x-ray beams. The cross-section area of the x-ray beams on the virtual plane becomes  $A_Q = \frac{A_O}{\cos(\theta)}$  when the same x-ray beams with cross-section unit area  $A_O$  are projected onto the point  $Q$  with an angle  $\theta$ . The measured intensity  $I_Q$  caused by obliquity alone is

$$I'_Q = I_Q \cos(\theta) \quad (4.9)$$

where  $\cos(\theta) = \frac{d}{r}$ .

The combination of inverse square law and obliquity effect is multiplicative. From (4.8) and (4.9), the overall intensity at the point  $Q$  is given by

$$I'_Q = I_O \frac{d^3}{(d^2 + x^2 + y^2)^{\frac{3}{2}}}. \quad (4.10)$$

Let the area projected on the virtual plane within FOV be  $A_{FOV}$ , shown in Fig. 43(a). The entrance dose  $D_E$  is calculated by integrating  $I'_Q$  over the area  $A_{FOV}$  as follows:

$$D_E = \iint_{A_{FOV}} I'_Q \, dA. \quad (4.11)$$

Let  $A_{FOV,m}$  be the maximal area on the virtual plane when the full field imaging is applied, and  $D_{E,m}$  denotes the corresponding entrance dose. Define entrance dose relative to that in the full field imaging as

$$D_{\%} = \frac{D_E}{D_{E,m}} \times 100\% \quad (4.12)$$

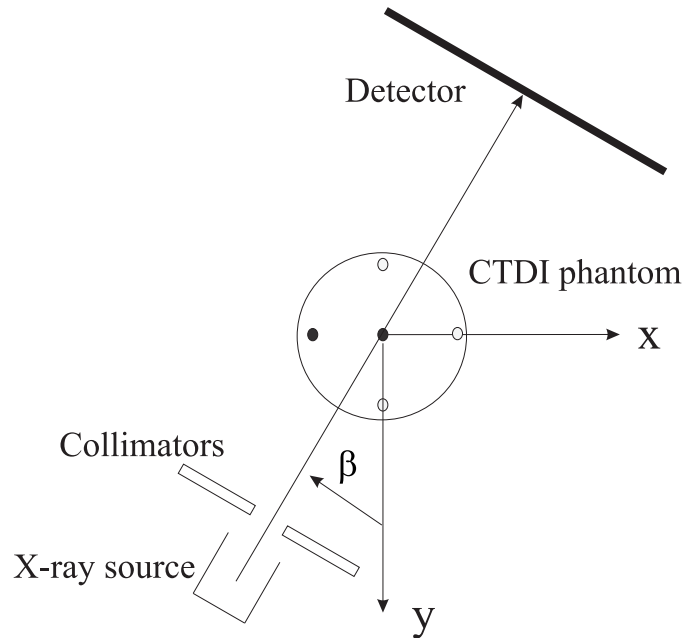


Fig. 44. The CTDI head phantom was placed in the center of the trajectory with an ion chamber inserted alternately at the center and periphery (the solid points).

where  $D_{\%}$  is the entrance dose relative to the maximal entrance dose  $D_{E,m}$ .

Dose measurement was made using a cylindrical CT dose index (CTDI) phantom (ImPACT) with a diameter of 160mm. This is the standard PerspexR CTDI head phantom with a central hole and four peripheral holes of 10 mm diameter below the surface. Fig. 44 shows the CTDI head phantom during CBCT scans from the longitudinal view and the two locations at which an ion chamber (10X5-3T, Radcal Corporation) in conjunction with the radiation monitor (1015C, Radcal Corporation) was inserted. The ion chamber was inserted in either the center or the peripheral position during each scan. The gantry rotation was over  $\beta = -90^{\circ} \sim 130^{\circ}$ . The measured doses  $R$  are in a unit of roentgen. The relationship between measured doses  $R$  and  $CTDI_{100}$  is

$$CTDI_{100} = 0.876 \times 2 \times R \quad (4.13)$$

where 2 is a correction factor for the specific ion chamber, and 0.876 is a factor converting roentgen into rad in the air. The weighted dose  $CTDI_w$  was calculated by

$$CTDI_w = \frac{1}{3}CTDI_{100,c} + \frac{1}{3}CTDI_{100,p} \quad (4.14)$$

where  $CTDI_{100,c}$  and  $CTDI_{100,p}$  are the measured doses of the center and the peripheral positions, respectively. The radiation doses were measured with different open areas of transverse and longitudinal collimators. A radiologist watched the numerical values of the monitor and confirmed the results. Two experiments were conducted. In the first, the length  $C_t$  was varying with a fixed  $C_l = 295\text{mm}$ , and in the second, both the length  $C_t$  and width  $C_l$  were varying. The dose of full field ("Without collimation") was normalized to 100%.

## C. Results

### 1. ROI Reconstruction Using Truncation Correction

Fig. 45 shows the reconstruction of these three experiments on the midplane ( $z = 0$ ), on which the circular trajectory of CT scan lies. Most of the parts in the ROI are recovered except for slightly nonuniform gray values close to the peripheral of the ROI. This distortion becomes obvious in Fig. 45(c). The intensity of Fig. 45(b) and (c) is slightly biased compared to that of the "without collimation" imaging. The intensity of x-ray beams varied because of automatic exposure control, and, therefore, the background of projection images (the part that x-ray beams pass through the air) is not always kept the same. This information is lost when the projections are truncated.

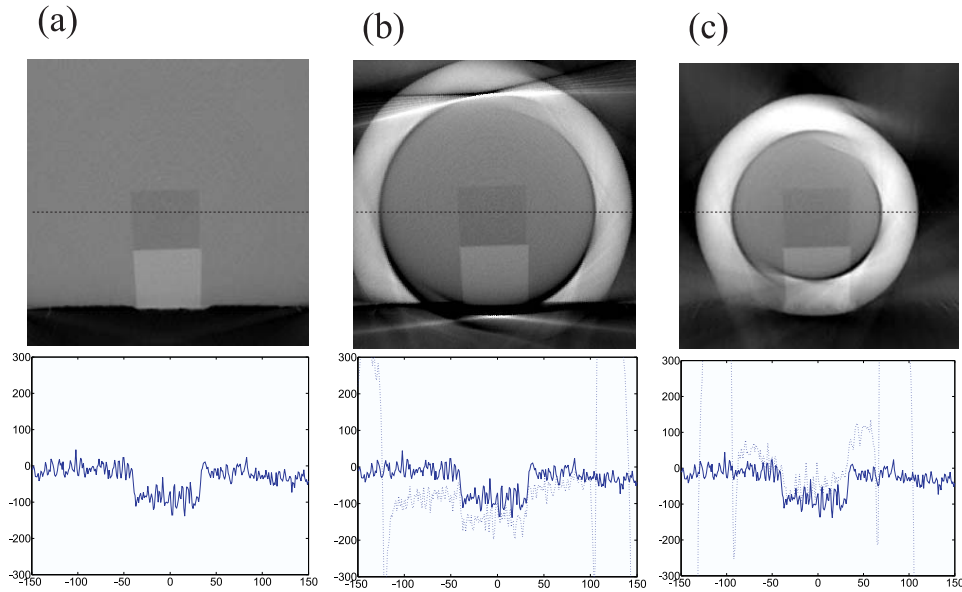


Fig. 45. The reconstruction of "without collimation" (a),  $C_t = 150\text{mm}$ ,  $C_l = 83\text{mm}$  (b), and  $C_t = 110\text{mm}$ ,  $C_l = 77\text{mm}$  (c). The images at the top were displayed in Hounsfield units of a range of  $[-1000\ 1000]$ . The intensity of the dashed lines of the top images was shown at the bottom. The solid lines of the bottom represent the intensity of "without collimation imaging" while the dotted lines of the bottom are that of "with collimation".

## 2. FDK and $\Pi$ -line Reconstruction under Severe Truncation

Fig. 46 shows the reconstructed images by the FDK (Fig. 46(a) and (b)) and by the  $\pi$ -line algorithm in the midplane ( $z = 0$ ). In Fig. 46(b) and (d), only the ROI within FOV was displayed. The bright artifacts exist not only around the ROI but in the middle. Compared to the reconstruction from truncation projections in [83], [93], when ROI is small enough, the artifacts will be too prominent to ruin the whole images.

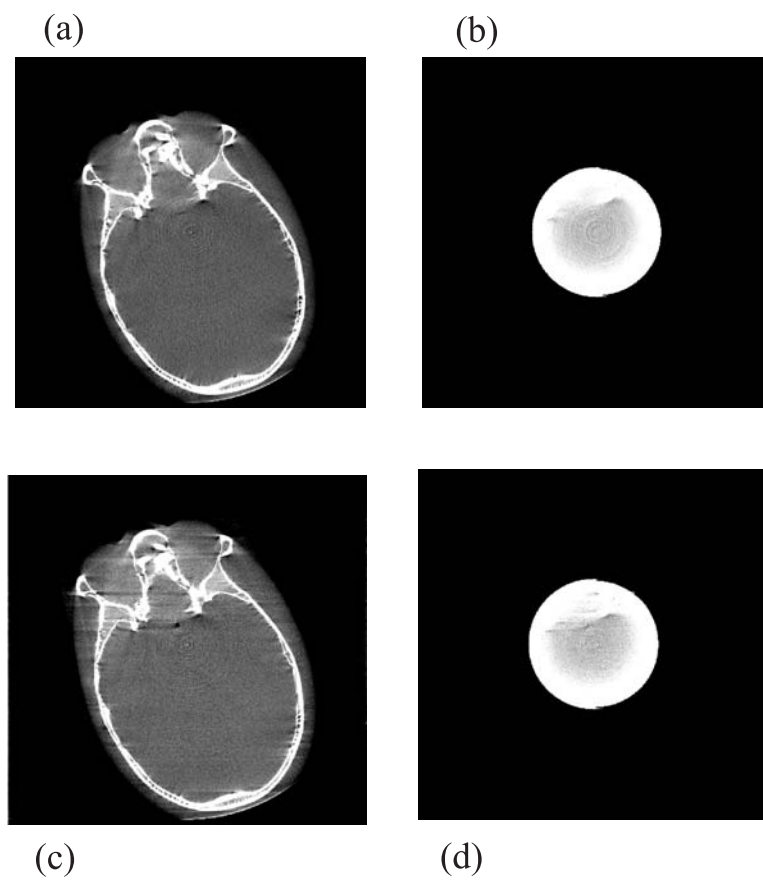


Fig. 46. The images are shown in the display window [0.002 0.007] (a) The FDK reconstruction of "without collimation" imaging. (b) The  $\pi$ -line reconstruction of "without collimation" imaging. (c) The FDK reconstruction of "with collimation" imaging with  $C_t = 130\text{mm}$  and  $C_l = 130\text{mm}$ . (d) The  $\pi$ -line reconstruction of "with collimation" imaging with  $C_t = 130\text{mm}$  and  $C_l = 130\text{mm}$ .

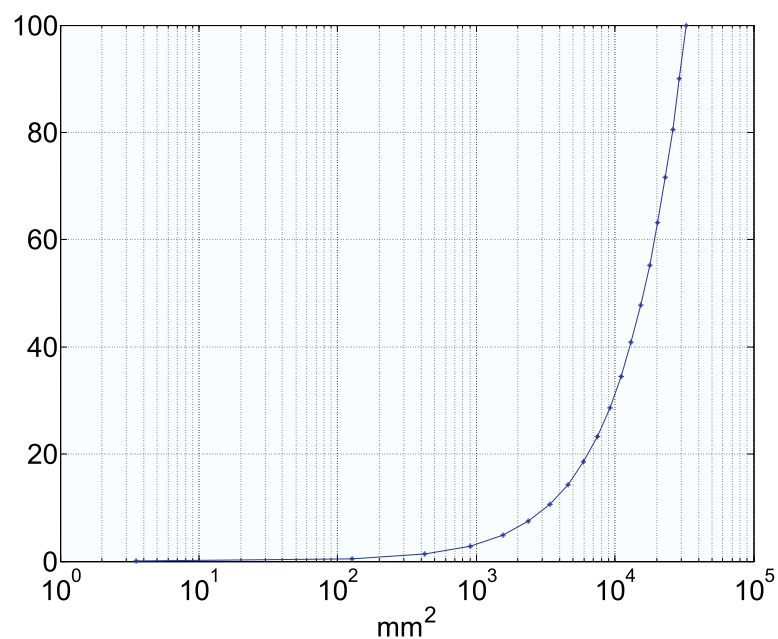


Fig. 47. The graph shows the entrance dosage  $D$  relative to full field in % versus the  $A_{FOV}$

Table VIII. Dose, Tube Voltages, and Tube Currents with Fixed  $C_l = 295mm$

$C_t$	Center			Peripheral		
	Dose	KV	mA	Dose	KV	mA
25mm	1.82	92	216	0.74	92	217
85mm	1.75	78	257	1.10	78	256
145mm	2.18	80	249	1.71	80	249
205mm	2.21	80	251	1.85	80	250
265mm	2.23	80	250	1.95	79	251
325mm	2.23	80	250	1.96	79	251

### 3. Reduction of Radiation Dose

The calculation of entrance dose was based on specifications in Table VII. The estimated source-to-virtual-plane distance was 650mm, and the estimated  $A_{FOV,m}$  35213.75mm<sup>2</sup> (162.5 × 216.7mm), which was the  $A_{FOV}$  when the "without collimation" imaging was applied. Fig. 47 shows the  $D_{\%}$  versus  $A_{FOV}$  with fixed ratio of width to length 3:4, and a logarithmic (base 10) scale was used for the axis of  $A_{FOV}$ .

In the dose measurement, the size  $C_t \times C_l$  of full field ("without collimation") was 385 × 295mm<sup>2</sup>, and its measured doses, tube voltages, and tube current at the center and at the peripheral were 2.35 roentgen, 79 kV, 251 mA, 2.03 roentgen, 79kV, and 251mA, respectively. The doses, tube voltages, and tube currents at the center and periphery were measured in these two experiments, as shown in Table VIII and Table IX. Fig. 48 shows the dose relative to full field ("Without collimation") versus varying areas of FOV. A logarithmic (base 10) scale was used for the axis of areas. The doses for  $C_l = 25$ mm in Fig. 48 should be lower and below those for  $C_l = 85$ mm. It is worth noticing that the doses at the smallest open areas ( $C_l = 25$ mm) of the collimators were not the lowest among those of  $C_l \neq 25$ mm in Table VIII and Table IX. The tube voltages and currents for  $C_l = 25$ mm in Table VIII and Table VIII were above 90 kV and below 220mA compared with those for  $C_l = 25$ mm at about 80 kV and 250mA. This could be explained by automatic exposure control in the CBCT system. The tube voltage of x-ray beams would be automatically increased for fewer photons detected on the detector. Due to the exposure control mechanism, the same tube voltage and current are not able to be used for all the measurements. It is not possible to scale the doses to those with fixed tube voltage and current due to the lack of relationship with dose and tube parameters of collimated imaging. For the other measurements, the variation of tube voltages and currents was within 5% relative to 80kV and 250mA, and this measured dose was still reliable in this study.

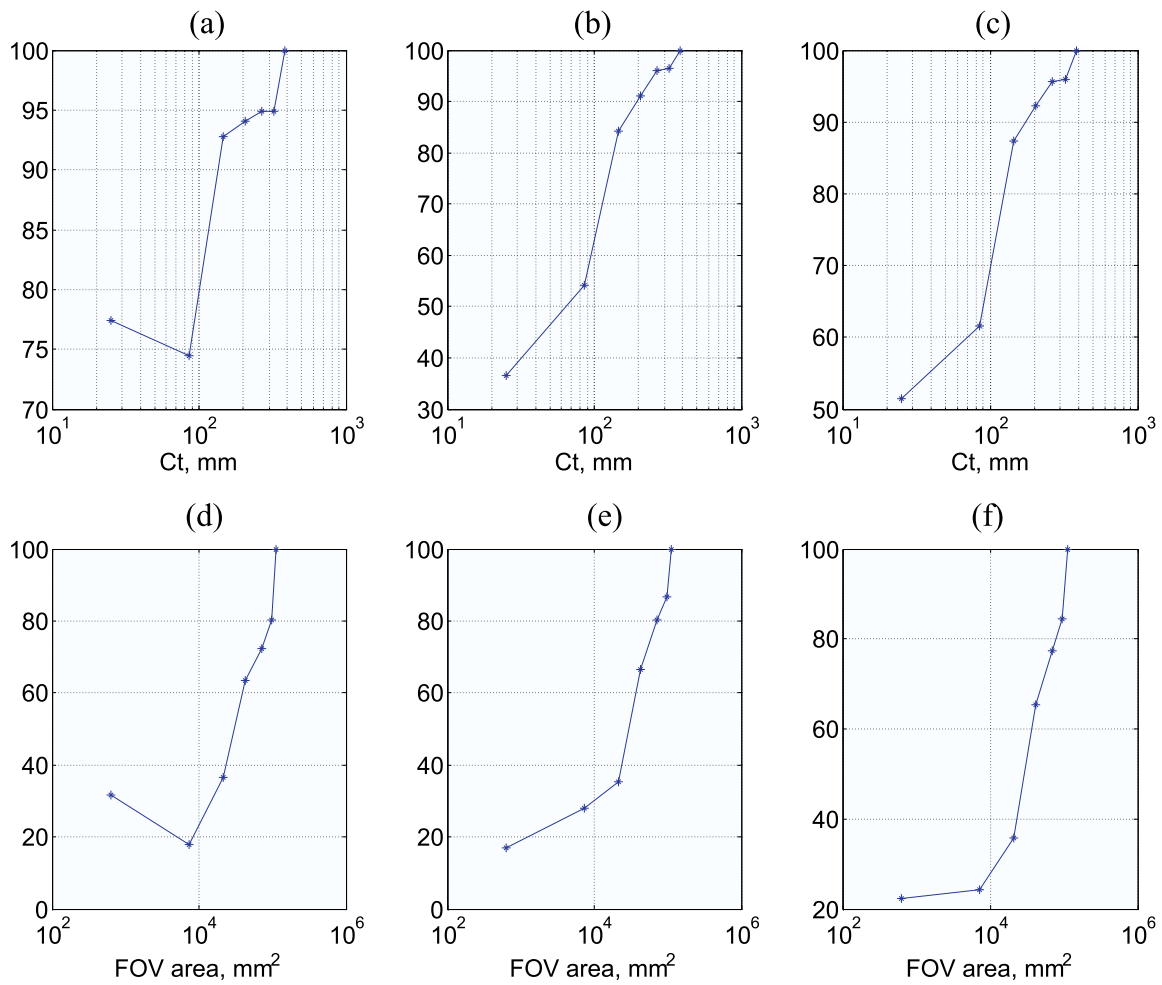


Fig. 48. Relative central and peripheral dose. (a) and (b) are the relative central and peripheral dose according to the Table VIII, and (c) is its relative weighted dose. (d) and (e) are the relative central and peripheral dose according to the Table IX, and (f) is its relative weighted dose.

Table IX. Dose, Tube Voltages, and Tube Currents with Varying FOV

$C_t \times C_l$	Center			Peripheral		
	Dose	KV	mA	Dose	KV	mA
$25 \times 25\text{mm}^2$	0.743	98	203	0.343	97	204
$85 \times 85\text{mm}^2$	0.422	80	250	0.571	83	240
$145 \times 145\text{mm}^2$	0.861	77	260	0.72	81	247
$205 \times 205\text{mm}^2$	1.49	80	248	1.35	80	249
$265 \times 265\text{mm}^2$	1.70	80	250	1.63	76	261
$325 \times 295\text{mm}^2$	1.89	79	251	1.76	79	251

#### D. Discussion

The ROI imaging is necessary when only a target inside the body of the patient is needed for 3D image visualization. During the interventional procedures, the whole body of the patient is imaged before and after the surgery in order to see the change in the region where the surgery is performed. A head phantom or body phantom was not used in the experiments of ROI reconstruction since these phantoms do not reflect constant density. Instead, cylindrical polystyrene was the target, and the water was used to emulate the background. The results imply that the contrast information is still kept in the ROI though a small bias of the image exists. The intensity of the object is not distorted compared to the nontruncation case. The different kernel filters in the FDK algorithms are derived from the ramp filter which is formed by Sinc function [94]. These filters have an impulse response with fast decay in both

sides. Since the FDK reconstruction is involved with convolution of the filter and projections, the reconstructed images towards the isocenter do not undergo much distortion. If one properly extend the truncated projections by extrapolation, it will mitigate the variation of reconstructed images caused by filtering truncated projections. The distortion in gray values becomes more obvious for reconstructed images distant from the isocenter. In the study [93], the discontinuity around the peripheral of the ROI could be largely removed using the prior knowledge which is the projection data of the first scan before the surgery. The results showed that the images around the peripheral of the ROI are still recognizable and enough to identify the structure around the object. The limit of ROI is exploited, and it can be discovered that the extrapolation technique in truncation correction with the FDK reconstruction can largely recover ROI image with an extremely small size of ROI. This size is small enough to demonstrate the possibility of ROI reconstruction with the smallest FOV. Until now, this is the most efficient implementation to reduce a large amount of radiation dose and to provide tolerable image quality.

The main purpose of simulating the two analytical reconstruction algorithms is to explain the impossibility of ROI reconstruction under severe truncation. Fig. 49(a) is the illustration of an object under ROI imaging with two  $\pi$ -line segments  $L_1$  and  $L_2$ . It can be observed that  $L_1$  passes through the support set of the object in ROI, but part of intersection  $L_2$  with the object is not inside the ROI. During the  $\pi$ -line reconstruction, each projection contains sufficient information for back projection onto the  $L_1$  regardless the partial truncation, but this is not true for the  $L_2$ . Correct reconstruction along  $L_2$  is not able to be obtained when performing filtering on incompletely backprojected images. That explains why the artifacts appear only when there is missing data in the filtered images. When ROI is entirely within the object as in Fig. 49(b), every  $\pi$ -line segment such as  $L_3$  contains part of the object

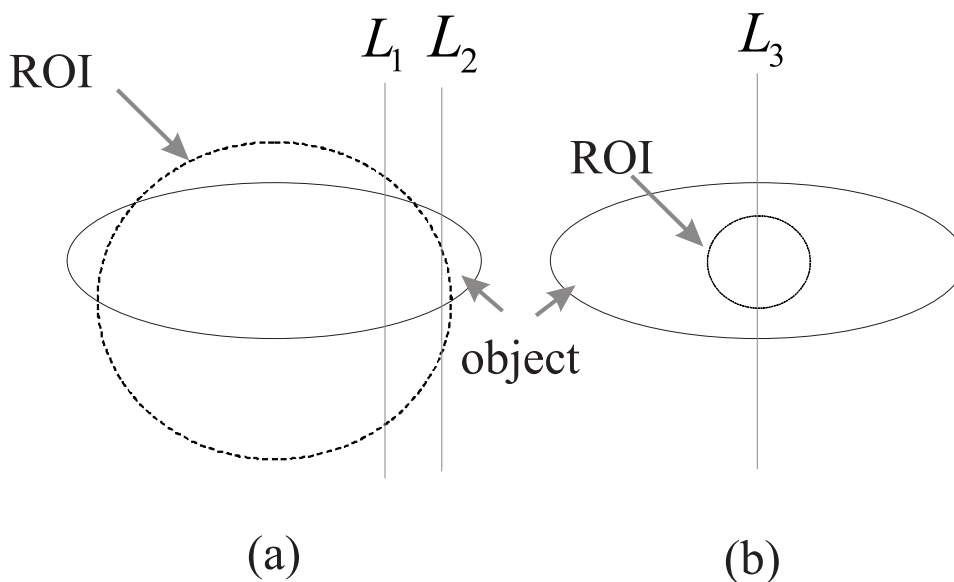


Fig. 49. The intersection of  $L_1$  with the object is entirely inside the ROI, but  $L_2$  and  $L_3$  are not.

outside the ROI. Like FBP analytical reconstruction algorithms, it is impossible for BPF reconstruction algorithms to avoid filtering insufficient data when the ROI is inside the object.

The experimental results showed that the use of collimators can reduce patient exposure by up to 70%. Because the measurement was done using the standard CTDI head phantom, the radiation dose reported herein should reasonably fit the actual circumstances for real patients. Since the collimators block x-ray beams such that exposure control mechanism increased the x-ray intensity during the scan, the results of dose measurement may be biased. The results showed the dose increased by automatic exposure control is generally less than that reduced by collimators. This dose reduction is more obvious at the peripheral of CTDI dose phantom; the collimators effectively absorb the unnecessary dose. Since scatter of x-ray beams is more severe in CBCT than traditional fan-beam CT, the dose applied to the patient will be different from patient to patient. The calculation of entrance dose provides a good way

to estimate the reduction in radiation dose of the collimated CT imaging irregardless of patients. The amount of entrance dose could be served as an appropriate indicator of how much radiation dose the patient would be potentially exposed to. Since it does not need to take scatter of x-ray beams into account, the computation is not as complicated as Monte Carlo dose simulation [95–97]. Furthermore, entrance dose computed in percentage is not affected by intensity of x-ray tube.

The limitation of this study is that the tube current and voltage could not be fixed all the time. This gives less reliable evaluation of image quality such as contrast-to-noise ratio. In the study [98], the contrast-to-noise ratio was calculated to prove it was improved since the collimators alleviated scatter of x-ray beams from the peripheral. However, the transverse collimators were not applied; the influence of truncation did not exit. In this study, the distortion caused by truncation instead of the contrast-to-noise ratio is mainly concerned.

## CHAPTER V

## CONCLUSION

In the first project, a two-step approach was developed to automatically and digitally articulate the maxillary and mandibular teeth. The first step was the initial procedure that aligned the mandibular dental model relatively closer to the maxillary model in an approximate MI. Two set of the feature points of dental curves were extracted. One was the feature points for the curve of central groove and pits of the maxillary dental model, and the other was the feature points for the curve of the cusps and incisal edges of the mandibular dental model. By matching these two set of the feature points using the point matching algorithm, an initial occlusion can be achieved by intentionally ignoring any possible collision between digital dental models. The second step was the final procedure. The initially-aligned models were aligned and fine-tuned to their final occlusion that was collision-free using the ISMDM algorithm. Two controlling mechanisms were designed. The first was the collision constraints to detect and prevent the penetration between the maxillary and the mandibular dental models. The second was the minimization of average distance of surface between the models in order to articulate the models. These two mechanisms were incorporated into an optimization problem and can be solved by quadratic programming. The proposed approach was validated by using 12 sets of the dental models. Using proposed approach, the maxillary and mandibular models can be successfully articulated. There was only a small degree of deviation between the digitally articulated occlusion established with proposed approach and the scanned occlusion established using the current gold standard. This small degree of deviation did not have clinical significance.

In the second project, a segmentation approach BIWASM and an initialization approach CWBI were developed to calculate the outer surface of anterior wall in

maxilla. This segmentation approach was based on customized WDM. The training shape was customized, extracted, decomposed into patches. Then, these patches are parameterized, subdivided, and stitched to form a remeshed training shape with regularized landmarks. The WDM can be built by aligning the training shapes to the model space and applying Principle Component Analysis to wavelet coefficients of the training shapes. By selecting several control landmarks to form a base in the image space, CWBI calculated a customized initial shape and a transformation between the base formed by selected control landmarks and a base in the model space. This transformation was fixed during each iteration of BIWASM. Only the shape parameters were changed in order to search for the candidate shape. Two sets of the experiments were designed to validate the proposed segmentation approach by using 19 CBCT datasets. Three other model-based segmentation approaches were also applied in the experiments to compare their results. The proposed approach outperformed the other three approaches in both sets of the experiments. It achieved  $0.25 \pm 0.2$  surface errors.

In the third project, a method to performing small ROI imaging was presented using lead collimators. Two experiments were conducted. In the first experiment, an imaged cylinder made of polystyrene was within ROI of diameters 70mm and 94mm in a water tank as background, and the truncation correction technique with FDK was applied. The concept of entrance dose for estimating the radiation dose absorbed in the body was used, and dose measurement was conducted with ROI imaging. It was found at least 60% and 70% of radiation dose was reduced for ROI of diameters 70mm and 94mm, respectively, according to the radiation dose measurement. Furthermore, the image quality was still acceptable with little variation of gray values. In the second experiment, a fixed area of ROI within a head phantom was imaged and reconstructed by both FDK and  $\pi$ -line reconstruction algorithm. It can be demon-

strated that it was not possible to reconstruct a ROI which was totally encompassed by the object by analytical reconstruction algorithms. Although the ROI imaging using the collimators caused the notorious truncation artifacts, the variation of gray values was mild enough for recognition of the ROI image after applying the truncation correction technique. The small ROI imaging enabled us to visualize the ROI with almost no loss of image quality and benefit from considerable reduction in radiation dose.

## REFERENCES

- [1] J. Gateno, J. J. Xia, J. F. Teichgraeber, A. M. Christensen, J. J. Lemoine, M. A. Liebschner, M. J. Gliddon, and M. E. Briggs, “Clinical feasibility of computer-aided surgical simulation (CASS) in the treatment of complex cranio-maxillofacial deformities,” *J. Oral Maxillofac. Surg.*, vol. 65, pp. 728–34, Apr. 2007.
- [2] G. R. Swennen, E. L. Barth, C. Eulzer, and F. Schutyser, “The use of a new 3D splint and double CT scan procedure to obtain an accurate anatomic virtual augmented model of the skull,” *Int. J. Oral Maxillofac. Surg.*, vol. 36, no. 2, pp. 146–52, Feb. 2007.
- [3] J. J. Xia, J. Gateno, and J. F. Teichgraeber, “Three-dimensional computer-aided surgical simulation for maxillofacial surgery,” *Atlas Oral Maxillofac. Surg. Clin. North Am.*, vol. 13, no. 1, pp. 25–39, Mar. 2005.
- [4] W. H. Bell and C. A. Guerrero, *Distraction Osteogenesis of the Facial Skeleton*. Hamilton, Ontario: BC Decker, 2006.
- [5] C. Ferencz and J. Greco, “A method for the three-dimensional study of pulmonary arteries,” *Chest*, vol. 57, no. 5, pp. 428–434, May 1970.
- [6] G. T. Herman and H. K. Liu, “Three-dimensional display of human organs from computed tomograms,” *Computer Graphics and Images Processing*, vol. 9, no. 1, pp. 1–21, 1979.
- [7] R. S. Pickering, R. R. Hattery, G. W. Hartman, and K. E. Holley, “Computed tomography of the excised kidney,” *Radiology*, vol. 113, pp. 643–647, 1974.

- [8] D. E. Altobelli, R. Kikinis, J. B. Mulliken, H. Cline, W. Lorensen, and F. Jolesz, "Computer-assisted three-dimensional planning in craniosurgical planning," *Plast. Reconstr. Surg.*, vol. 92, no. 4, pp. 576–85, Sep. 1993.
- [9] J. Bill, J. F. Reuther, T. Betz, W. Dittmann, and G. Wittenberg, "Rapid prototyping in head and neck surgery planning," *J. Craniomaxillofac. Surg.*, vol. 24, pp. 20–29, 1996.
- [10] J. Xia, H. H. S. Ip, N. Samman, D. Wang, C. S. B. Kot, R. W. K. Yeung, and H. Tideman, "Computer-assisted three-dimensional surgical planning and simulation: 3D virtual osteotomy," *International Journal of Oral & Maxillofacial Surgery*, vol. 29, no. 1, pp. 11–17, 2000.
- [11] J. J. Xia, H. H. S. Ip, N. Samman, H. T. F. Wong, J. Gateno, D. Wang, R. W. K. Yeung, C. S. B. Kot, and H. Tideman, "Three-dimensional virtual-reality surgical planning and soft-tissue prediction for orthognathic surgery," *IEEE Trans. Inf. Technol. Biomed.*, vol. 5, no. 2, pp. 97–107, Jun. 2001.
- [12] S. Zachow, H. C. Hege, and P. Deuffhard, "Computer-assisted planning in cranio-maxillofacial surgery," *J. Computing. and Inf. Technol.*, vol. 14, no. 1, pp. 53–64, 2006.
- [13] L. A. Feldkamp, L. C. Davis, and J. W. Kress, "Practical cone-beam algorithm Sfrdr I \_ f," *J. Opt. Soc. Am.*, vol. 1, no. 6, pp. 612–619, 1984.
- [14] W. E. Lorensen and H. E. Cline, "Marching cubes: A high resolution 3D surface construction algorithm," *Computer Graphics*, vol. 21, no. 4, pp. 163–169, 1987.
- [15] J. Gateno, J. J. Xia, J. F. Teichgraeber, and A. Rosen, "A new technique for the creation of a computerized composite skull model," *J. Oral and Maxillofac. Surg.*, vol. 61, no. 2, pp. 222–227, Feb. 2003.

- [16] G. R. J. Swennen, W. Mollemans, C. De Clercq, J. Abeloos, P. Lamoral, F. Lippens, N. Neyt, J. Casselman, and F. Schutyser, "A cone-beam computed tomography triple scan procedure to obtain a three-dimensional augmented virtual skull model appropriate for orthognathic surgery planning," *Journal of Craniofacial Surgery*, vol. 20, no. 2, p. 297, 2009.
- [17] G. R. J. Swennen, M. Y. Mommaerts, J. Abeloos, C. D. Clercq, P. Lamoral, N. Neyt, J. Casselman, and F. Schutyser, "A cone-beam CT based technique to augment the 3D virtual skull model with a detailed dental surface," *Int. J. Oral Maxillofac. Surg.*, vol. 38, no. 1, pp. 48–57, Jan. 2009.
- [18] J. J. Xia, J. Gateno, and J. F. Teichgraeber, "New clinical protocol to evaluate craniomaxillofacial deformity and plan surgical correction," *J. Oral Maxillofac. Surg.*, vol. 67, no. 10, pp. 2093–2106, Oct. 2009.
- [19] G. R. J. Swennen, F. Schutyser, and J. E. Hausamen, *Three-Dimensional Cephalometry: A Color Atlas and Manual*. Berlin, Germany: Springer, 2005.
- [20] W. H. Bell, *Surgical Correction of Dentofacial Deformities*. Philadelphia: WB Saunders Co., Jun. 1980.
- [21] M. M. Ash and S. P. Ramfjord, *Occlusion*. Philadelphia: WB Saunders Co., 1995.
- [22] J. P. Okeson, *Management of Temporomandibular Disorders and Occlusion*. St. Louis: CV Mosby, 2002.
- [23] T. Kondo, S. H. Ong, and C. K. W. Foong, "Tooth segmentation of dental study models using range images," *IEEE Trans. Med. Imag.*, vol. 23, no. 3, pp. 350–362, Mar. 2004.

- [24] M. Zhao, L. Ma, W. Tan, and D. Nie, "Interactive tooth segmentation of dental models," in *27th Annu. Int. Conf. Eng. Med. Biol. Soc.*, 2005, pp. 654–657.
- [25] J. J. Fang and T. H. Kuo, "Computer-aided design tracked motion-based dental occlusion surface estimation for crown restoration," *Computer-Aided Design*, vol. 41, no. 4, pp. 315–323, 2009.
- [26] S. Gold, A. Rangarajan, C. P. Lu, S. Pappu, and E. Mjolsness, "New algorithms for 2D and 3D point matching: pose estimation and correspondence," *Pattern Recognit.*, vol. 31, no. 8, pp. 1019–1031, Aug. 1998.
- [27] M. W. Walker, L. Shao, and R. A. Volz, "Estimating 3-D location parameters using dual number quaternions," *CVGIP: Image Underst.*, vol. 54, no. 3, pp. 358–367, Nov. 1991.
- [28] R. Sinkhorn, "A relationship between arbitrary positive matrices and doubly stochastic matrices," *Ann. Math. Statist.*, vol. 35, no. 2, pp. 876–879, 1964.
- [29] P. J. Besl and H. D. McKay, "A method for registration of 3-D shapes," vol. 14, no. 2, pp. 239–256, 1992.
- [30] V. J. Milenkovic and H. Schmidl, "Optimization-based animation," in *Proc. 28th Annu. Conf. Comput. Graph. and Interactive Techniques*, 2001, pp. 37–46.
- [31] L. Zhang, Y. J. Kim, G. Varadhan, and D. Manocha, "Generalized penetration depth computation," *Computer-Aided Design*, vol. 39, no. 8, pp. 625–638, Aug. 2007.
- [32] L. T. Hiew, S. H. Ong, and K. W. C. Foong, "Optimal occlusion of teeth," in *9th IEEE Int. Conf. Control, Automat., Robot., and Vision*, vol. pp, 2006, pp. 1–5.

- [33] C. Zhang, L. Chen, F. Zhang, H. Zhang, H. Feng, and G. Dai, “A new virtual dynamic dentomaxillofacial system for analyzing mandibular movement, occlusal contact, and TMJ condition,” *Lecture Notes in Comput. Sci.*, vol. 4561, pp. 747–756, 2007.
- [34] R. Delong, C. C. Ko, G. C. Anderson, J. S. Hodges, and W. H. Douglas, “Comparing maximum intercuspal contacts of virtual dental patients and mounted dental casts,” *The Journal of Prosthetic Dentistry*, vol. 88, no. 6, pp. 622–630, Dec. 2002.
- [35] W. C. Scarfe, A. G. Farman, M. D. Levin, and D. Gane, “Essentials of maxillofacial cone beam computed tomography,” *Alpha Omegan*, vol. 103, no. 2, pp. 62–67, Jun. 2010.
- [36] F. A. Quereshy, T. A. Savell, and J. M. Palomo, “Applications of cone beam computed tomography in the practice of oral and maxillofacial surgery.” *J. Oral Maxillofac. Surg.*, vol. 66, no. 4, pp. 791–6, Apr. 2008.
- [37] S. L. Hechler, “Cone-beam CT: applications in orthodontics,” *Dental Clinics of North America*, vol. 52, no. 4, pp. 809–823, 2008.
- [38] S. C. White and M. J. Pharoah, *Oral Radiology: Principles and Interpretation*. St. Louis, MI: Mosby, 2003.
- [39] W. C. Scarfe, A. G. Farman, and P. Sukovic, “Clinical applications of cone-beam computed tomography in dental practice.” *J. Can. Dent. Assoc.*, vol. 72, no. 1, pp. 75–80, Feb. 2006.
- [40] S. Tucker, L. H. S. Cevidanes, M. Styner, H. Kim, M. Reyes, W. Proffit, and T. Turvey, “Comparison of actual surgical outcomes and 3-dimensional surgical simulations.” *J. Oral Maxillofac. Surg.*, vol. 68, no. 10, pp. 2412–21, Oct. 2010.

- [41] L. H. C. Cevidanes, S. Tucker, M. Styner, H. Kim, J. Chapuis, M. Reyes, W. Proffit, T. Turvey, and M. Jaskolka, “Three-dimensional surgical simulation.” *Am. J. Orthod. Dentofacial. Orthop.*, vol. 138, no. 3, pp. 361–71, Sep. 2010.
- [42] G. R. J. Swennen, W. Mollemans, and F. Schutyser, “Three-dimensional treatment planning of orthognathic surgery in the era of virtual imaging.” *J. Oral Maxillofac. Surg.*, vol. 67, no. 10, pp. 2080–92, Oct. 2009.
- [43] G. Swennen and F. Schutyser, “Three-dimensional cephalometry: Spiral multi-slice vs cone-beam computed tomography,” *Am. J. Orthod. Dentofacial. Orthop.*, vol. 130, no. 4, pp. 410–416, 2006.
- [44] K. Babalola and T. Cootes, “AAM segmentation of the mandible and brainstem,” in *Proc. of the 3rd Workshop on 3D Segmentation in the Clinic: MICCAI*, 2009.
- [45] D. Kainmueller, H. Lamecker, H. Seim, S. Zachow, and S. Antipolis, “Multi-object segmentation of head bones,” *MIDAS Journal, Contribution to MICCAI Workshop - Head and Neck Auto-Segmentation Challenge*, 2009.
- [46] S. Zachow, H. Lamecker, B. Elsholtz, and M. Stiller, “Reconstruction of mandibular dysplasia using a statistical 3D shape model,” *International Congress Series*, vol. 1281, pp. 1238–1243, May 2005.
- [47] D. Kainmueller, H. Lamecker, H. Seim, M. Zinser, and S. Zachow, “Automatic extraction of mandibular nerve and bone from cone-beam CT data,” in *MICCAI 2009, Part II*, 2009, pp. 76–83.
- [48] M. P. Dupillier, “An automatic segmentation and reconstruction of mandibular structures from CT Data,” in *IDEAL’09*, 2009, pp. 649–655.

- [49] M. Loubele, F. Maes, F. Schutyser, G. Marchal, R. Jacobs, and P. Suetens, “Assessment of bone segmentation quality of cone-beam CT versus multislice spiral CT: a pilot study.” *Oral Surgery, Oral Medicine, Oral Pathology, Oral Radiology, and Endodontics*, vol. 102, no. 2, pp. 225–34, Aug. 2006.
- [50] J. Chen and Y. Han, “Shortest paths on a polyhedron,” in *Proc. of the Sixth Annual Symposium on Computational Geometry - SCG '90*. New York: ACM Press, 1990, pp. 360–369.
- [51] M. S. Floater, K. Hormann, and M. Reimers, “Parameterization of manifold triangulations,” in *Approximation Theory X: Abstract and Classical Analysis*, C. K. Chui, L. L. Schumaker, J. Stockler, Eds. Nashville: Vanderbilt Univ. Press, 2002, pp. 197–209.
- [52] E. W. Dijkstra, “A note on two problems in connexion with graphs,” *Numerische Mathematik*, vol. 1, pp. 269–271, 1959.
- [53] K. Hormann, B. Lévy, and A. Sheffer, “Siggraph course notes mesh parameterization: theory and practice,” in *SIGGRAPH 2007 Course Notes*. New York: ACM, 2007, pp. 1–122.
- [54] E. Catmull and J. Clark, “Recursively generated B-spline surfaces on arbitrary topological meshes,” *Computer-Aided Design*, vol. 10, pp. 350–355, Nov. 1978.
- [55] C. J. Taylor, D. H. Cooper, and J. Graham, “Training models of shape from sets of examples,” in *Proc. British Machine Vision Conference*, 1992, pp. 9–18.
- [56] C. Goodall, “Procrustes methods in the statistical analysis of shape,” *Journal of the Royal Statistical Society*, vol. 53, no. 2, pp. 285–339, 1991.
- [57] B. K. P. Horn, “Closed-form solution of absolute orientation using unit quaternions,” *Journal of the Optical Society of America A*, vol. 4, no. 4, pp. 629–642,

1987.

- [58] M. Bertram, M. A. Duchaineau, B. Hamann, and K. I. Joy, “Generalized B-spline subdivision-surface wavelets for geometry compression.” *IEEE Transactions on Visualization and Computer Graphics*, vol. 10, no. 3, pp. 326–38, 2004.
- [59] I. Daubechies and W. Sweldens, “Factoring wavelet transforms into lifting steps,” *The Journal of Fourier Analysis and Applications*, vol. 4, no. 3, pp. 247–269, May 1998.
- [60] C. Davatzikos, X. Tao, and D. Shen, “Hierarchical active shape models, using the wavelet transform.” *IEEE Transactions on Medical Imaging*, vol. 22, no. 3, pp. 414–23, Mar. 2003.
- [61] D. Nain, S. Haker, A. Bobick, and A. Tannenbaum, “Multiscale 3-D shape representation and segmentation using spherical wavelets.” *IEEE Transactions on Medical Imaging*, vol. 26, no. 4, pp. 598–618, Apr. 2007.
- [62] Y. Li, T.-S. Tan, I. Volkau, and W. L. Nowinski, “Model-guided segmentation of 3D neuroradiological image using statistical surface wavelet model,” in *2007 IEEE Conference on Computer Vision and Pattern Recognition*. IEEE, 2007, pp. 1–7.
- [63] S. Essafi, G. Langs, J.-F. Deux, A. Rahmouni, G. Bassez, and N. Paragios, “Wavelet-driven knowledge-based MRI calf muscle segmentation,” *2009 IEEE International Symposium on Biomedical Imaging: From Nano to Macro*, pp. 225–228, Jun. 2009.
- [64] T. Cootes, C. J. Taylor, D. H. Cooper, and J. Graham, “Active shape models—their training and application,” *Computer Vision and Image Understanding*, vol. 61, no. 1, pp. 38–59, Jan. 1995.

- [65] I. Berlin, “Segmentation of the liver using a 3D statistical shape model,” *ZIB-Report 04-09*, 2004.
- [66] S. Essafi, G. Langs, and N. Paragios, “Left ventricle segmentation using diffusion wavelets and boosting,” in *MICCAI 2009, Part II, LNCS 5762*, 2009, pp. 919–926.
- [67] J. Fripp, S. Warfield, S. Crozier, and S. Ourselin, “Automatic segmentation of the knee bones using 3D active shape models,” *18th International Conference on Pattern Recognition (ICPR’06)*, pp. 167–170, 2006.
- [68] R. H. Davies, C. J. Twining, T. F. Cootes, and C. J. Taylor, “Building 3D statistical shape models by direct optimisation.” *IEEE Transactions on Medical Imaging*, vol. 29, no. 4, pp. 961–981, Nov. 2009.
- [69] J. W. Ma and Y. H. Fan, “Face segmentation algorithm based on ASM,” in *2009 IEEE International Conference on Intelligent Computing and Intelligent Systems*, Nov. 2009, pp. 495–499.
- [70] M. D. Bruijne, B. V. Ginneken, M. A. Viergever, and W. J. Niessen, “Adapting active shape models for 3D segmentation of tubular structures in medical images,” *Inf Process Med Imaging*, vol. 18, pp. 136–47, 2003.
- [71] M. Zöckler, D. Stalling, and H.-C. Hege, “Fast and intuitive generation of geometric shape transitions,” *The Visual Computer*, vol. 16, no. 5, pp. 241–253, Jun. 2000.
- [72] H. Lamecker, M. Seebaß, H.-c. Hege, and P. Deuffhard, “A 3D statistical shape model of the pelvic bone for segmentation,” in *Proc. SPIE Medical Imaging 2004: Image Processing.*, 2004, pp. 1341–1351.

- [73] P. Dalal, L. Ju, M. McLaughlin, X. Zhou, H. Fujita, and S. Wang, “3D open-surface shape correspondence for statistical shape modeling : identifying topologically consistent landmarks,” in *ICCV09*, Kyoto, 2009, pp. 1857–1864.
- [74] Y. Lee, “Mesh parameterization with a virtual boundary,” *Computers & Graphics*, vol. 26, no. 5, pp. 677–686, Oct. 2002.
- [75] N. N. Mollemans, A. Daelemans, G. V. Hemelen, F. Schutyser, and S. Berge, “Virtual occlusion in planning orthognathic surgical procedures,” *Int. J. Oral Maxillofac. Surg.*, vol. 39, pp. 457–462, 2010.
- [76] Y. B. Chang, J. Xia, J. Gateno, Z. Xiong, X. Zhou, and S. Wong, “An automatic and robust algorithm of re-establishment of digital dental occlusion.” *IEEE Transactions On Medical Imaging*, vol. 29, no. 9, pp. 1652–63, 2010.
- [77] J. J. Xia and J. Gateno, “Accuracy of a Computer-Aided Surgical Simulation (CASS) system in the treatment of complex cranio-maxillofacial deformities: a pilot study,” *J Oral Maxillofac Surg*, vol. 65, no. 2, pp. 248–54, 2007.
- [78] K. Wiesent, K. Barth, N. Navab, P. Durlak, T. Brunner, O. Schuetz, and W. Seissler, “Enhanced 3-D-reconstruction algorithm for C-arm systems suitable for interventional procedures.” *IEEE Transactions on Medical Imaging*, vol. 19, no. 5, pp. 391–403, May 2000.
- [79] M. Zellerhoff, B. Scholz, E.-P. Ruehrschopf, and T. Brunner, “Low contrast 3D reconstruction from C-arm data,” *SPIE*, vol. 5745, pp. 646–655, 2005.
- [80] J. L. Prince and J. M. Links, *Medical Imaging Signals and Systems*. Englewood Cliffs, New Jersey: Prentice Hall, 2005.
- [81] J. C. Gore and S. Leeman, “The reconstruction of objects from incomplete

- projections,” *Physics in Medicine and Biology*, vol. 25, no. 1, pp. 129–136, 1980.
- [82] J. Hsieh, E. Chao, J. Thibault, B. Grekowicz, A. Horst, S. McOlash, and T. J. Myers, “A novel reconstruction algorithm to extend the CT scan field-of-view,” *Med. Phys.*, vol. 31, no. 9, pp. 2385–2391, 2004.
- [83] B. Ohnesorge, T. Flohr, K. Schwarz, J. P. Heiken, and K. T. Bae, “Efficient correction for CT image artifacts caused by objects extending outside the scan field of view.” *Medical Physics*, vol. 27, no. 1, pp. 39–46, Jan. 2000.
- [84] K. Rajgopal, N. Srinivasa, and K. Ramakrishnan, “Image reconstruction from incomplete projection data: a linear prediction approach,” in *Medical Imaging Systems Techniques and Applications Modalities*, Ed. C. ZLeondes. New York: Gordon and Breach Science Publishers, 1997, pp. 281–328.
- [85] K. Sourbelle, M. Kachelriess, and W. A. Kalender, “Reconstruction from truncated projections in CT using adaptive detruncation.” *European Radiology*, vol. 15, no. 5, pp. 1008–14, May 2005.
- [86] K. P. Anoop and K. Rajgopal, “Estimation of missing data using windowed linear prediction in laterally truncated projections in cone-beam CT.” in *EMBS 2007*, Jan. 2007, pp. 2903–6.
- [87] R. Clackdoyle and F. Noo, “A large class of inversion formulae for the 2D Radon transform of functions of compact support,” *Inverse Problems*, vol. 20, no. 4, pp. 1281–1291, Aug. 2004.
- [88] B. Zhang and G. L. Zeng, “Two-dimensional iterative region-of-interest (ROI) reconstruction from truncated projection data.” *Medical Physics*, vol. 34, no. 3, pp. 935–44, Mar. 2007.

- [89] S. Cho, J. Bian, C. A. Pelizzari, C.-T. Chen, T.-C. He, and X. Pan, "Region-of-interest image reconstruction in circular cone-beam microCT." *Medical Physics*, vol. 34, no. 12, pp. 4923–33, Dec. 2007.
- [90] J. HUBBELL, "Photon mass attenuation and energy-absorption coefficients," *The International Journal of Applied Radiation and Isotopes*, vol. 33, no. 11, pp. 1269–1290, Nov. 1982.
- [91] L. A. Feldkamp, L. C. Davis, and J. W. Kress, "Practical cone-beam algorithm," *Journal of the Optical Society of America A*, vol. 1, no. 6, p. 612, Jun. 1984.
- [92] L. Yu, Y. Zou, E. Y. Sidky, C. A. Pelizzari, P. Munro, and X. Pan, "Region of interest reconstruction from truncated data in circular cone-beam CT." *IEEE Transactions on Medical Imaging*, vol. 25, no. 7, pp. 869–81, Jul. 2006.
- [93] J. Wiegert, M. Bertram, T. Netsch, J. Wulff, J. Weese, and G. Rose, "Projection extension for region of interest imaging in cone-beam CT." *Academic Radiology*, vol. 12, no. 8, pp. 1010–23, Aug. 2005.
- [94] A. C. Kak and M. Slaney, *Principles of Computerized Tomographic Imaging*. New York: IEEE Press, 1988.
- [95] P. Deak, M. van Straten, P. C. Shrimpton, M. Zankl, and W. A. Kalender, "Validation of a Monte Carlo tool for patient-specific dose simulations in multi-slice computed tomography." *European Radiology*, vol. 18, no. 4, pp. 759–72, Apr. 2008.
- [96] B. Schmidt and W. A. Kalender, "A fast voxel-based Monte Carlo method for scanner-and patient-specific dose calculations in computed tomography," *Physica Medica*, vol. 18, pp. 43–53, 2002.

- [97] I. Sechopoulos, S. Vedantham, S. Suryanarayanan, C. J. D’Orsi, and A. Karellas, “Monte Carlo and phantom study of the radiation dose to the body from dedicated CT of the breast.” *Radiology*, vol. 247, no. 1, pp. 98–105, Apr. 2008.
- [98] C. J. Moore, T. E. Marchant, and A. M. Amer, “Cone beam CT with zonal filters for simultaneous dose reduction, improved target contrast and automated set-up in radiotherapy.” *Physics in Medicine and Biology*, vol. 51, no. 9, pp. 2191–204, May 2006.
- [99] M. Floater, “Mean value coordinates,” *Computer Aided Geometric Design*, vol. 20, no. 1, pp. 19–27, Mar. 2003. [Online]. Available: <http://linkinghub.elsevier.com/retrieve/pii/S0167839603000025>
- [100] Y. Zou and X. Pan, “Exact image reconstruction on PI-lines from minimum data in helical cone-beam CT.” *Physics in Medicine and Biology*, vol. 49, no. 6, pp. 941–59, Mar. 2004.
- [101] X. Pan, D. Xia, Y. Zou, and L. Yu, “A unified analysis of FBP-based algorithms in helical cone-beam and circular cone- and fan-beam scans.” *Physics in Medicine and Biology*, vol. 49, no. 18, pp. 4349–69, Sep. 2004.

## APPENDIX A

## BARYCENTRIC MAPPINGS

The parameterization over the mesh is a homeomorphism mapping  $\varphi : \Omega_S \rightarrow \Omega_D$  between the shape  $\Omega_S$  and a base domain  $\Omega_D$  with known topology. Practically, the mapping is defined by the vertices  $\mathbf{r}_i$  of a mesh and their corresponding points  $\mathbf{p}_i$  in the base domain

$$\varphi : \mathbf{r}_i \rightarrow \mathbf{p}_i \tag{A.1}$$

In barycentric mapping,  $\mathbf{p}_i$  is defined in a known planar topology and is a linear combination of its neighboring points. A simple approach to construct barycentric mapping is based on the physical model of springs. The springs are the analogy of edges in the mesh. When the boundaries of spring network (mesh) are fixed on the boundaries of the known planar topology, the interior spring network will be relaxed according to its most efficient energy configuration. Assume the spring is stable and returning to the rest state when all nodes of spring network lie on the planar topology. These nodes at stable state can be regarded as parameterization points. The parameterization of the mesh over a plane can be formed by a mapping between those corresponding nodes before and after relaxation of springs.

Let  $s$  be the spring constant and  $l$  be the length of the spring. The potential energy is given by  $E = \frac{1}{2}sl^2$ . For simplicity,  $\mathbf{r}_i, i = 0, 1, \dots, N - N_b - 1$  denote the interior vertices of the mesh, and  $i = N + N_b, \dots, N - 1$  are the boundaries vertices. Assume the mapping of boundary points between the mesh and the planar topology (i.e.  $\varphi : \mathbf{r}_i \rightarrow \mathbf{p}_i, i = N + N_b, \dots, N - 1$ ) is known. The potential energy of the spring network (network composed of the parameterization points) can be given by

$$E = \frac{1}{2} \sum_{i=0}^{N-N_b-1} \sum_{j \in C_i} \frac{1}{2} s_{ij} \|\mathbf{p}_i - \mathbf{p}_j\|^2 \tag{A.2}$$

where  $C_i$  is the set of indices of vertices connecting to  $\mathbf{r}_i$ , and  $s_{ij}$  is the spring constant between the connecting points  $\mathbf{p}_i$  and  $\mathbf{p}_j$ . The second  $\frac{1}{2}$  ensures the potential spring energy is calculated only once due to  $s_{ij} = s_{ji}$ . To achieve "stable spring state",  $E$  is minimized with respect to  $\mathbf{p}_i, \forall i$ . Since (A.2) is a quadratic expression, the condition when it is minimized is

$$\sum_{j \in C_i} s_{ij} \mathbf{p}_i = \sum_{j \in C_i} s_{ij} \mathbf{p}_j \quad (\text{A.3})$$

The  $\mathbf{p}_i$  can be expressed in terms of affine combinations of its connecting points as

$$\mathbf{p}_i = \sum_{j \in C_i} \tilde{\lambda}_{ij} \mathbf{p}_j \quad (\text{A.4})$$

where

$$\tilde{\lambda}_{ij} = \frac{s_{ij}}{\sum_{k \in C_i} s_{ik}}. \quad (\text{A.5})$$

It indicates

$$\sum_i \tilde{\lambda}_i = 1. \quad (\text{A.6})$$

$\tilde{\lambda}_{ij}$  is called barycentric coordinate of  $\mathbf{p}_i$  in terms of connecting vertices of  $\mathbf{p}_j, j \in C_i$  if both (A.4) and (A.6) are satisfied. If  $\tilde{\lambda}_{ij} \geq 0$ , this linear combination becomes the combination. The positive  $\tilde{\lambda}_{ij}$  can reduce the chance of overlapping triangles in the parameterization domain [53]. This can be achieved by choosing  $s_{ij}$  as Mean Value Coordinate proposed by Floater [99]. Of the note that Mean Value Coordinate contains information of edge lengths and face angles in the mesh and is not necessarily symmetric, i.e.  $s_{ij} \neq s_{ji}$ .

To calculate the parameterization by minimizing spring energy  $E$  in (A.2), (A.4) can be reformulated as a sparse linear system. Given known boundary points  $\mathbf{p}_i, i = N + N_b, \dots, N - 1$  in the parameterization domain and  $\tilde{\lambda}_{ij}$ , the interior points  $\mathbf{p}_i, i = 0, 1, \dots, N - N_b - 1$  can be calculated by solving the sparse linear system using sparse linear solver.

## APPENDIX B

## COMPOSITE LIFTING STEP

Assume the rectilinear grid is applied. Fig. 50 shows an example of the grid.  $r$  and  $c$  denote the row and column indices. The *s-lifting* step in the row using (3.13) is

$$\mathbf{v}_{r,c} \leftarrow \alpha \mathbf{v}_{r,c} + \tilde{\alpha}(\mathbf{e}_{r,c} + \mathbf{e}_{r,c+1}) \quad (\text{B.1})$$

$$\tilde{\mathbf{e}}_{r,c+i} \leftarrow \alpha \tilde{\mathbf{e}}_{r,c+i} + \tilde{\alpha}(\mathbf{f}_{r+i,c} + \mathbf{f}_{r+i,c+1}) \quad (\text{B.2})$$

Similarly, the *s-lifting* step in the column using (3.13) can be written by

$$\mathbf{v}_{r,c} \leftarrow \alpha \mathbf{v}_{r,c} + \tilde{\alpha}(\tilde{\mathbf{e}}_{r,c} + \tilde{\mathbf{e}}_{r+1,c}) \quad (\text{B.3})$$

$$\mathbf{e}_{r+i,c} \leftarrow \alpha \mathbf{e}_{r+i,c} + \tilde{\alpha}(\mathbf{f}_{r,c+i} + \mathbf{f}_{r+1,c+i}) \quad (\text{B.4})$$

Incorporated with (B.1), (B.3) can be written as

$$\mathbf{v}_{r,c} \leftarrow \alpha^2 \mathbf{v}_{r,c} + 4\tilde{\alpha}^2(\bar{\mathbf{f}}_{r,c}) + 4\alpha\tilde{\alpha}\bar{\mathbf{e}}_{r,c} \quad (\text{B.5})$$

where  $\bar{\mathbf{e}}_{\mathbf{v},r,c} \equiv \frac{\tilde{\mathbf{e}}_{r,c} + \tilde{\mathbf{e}}_{r+1,c} + \mathbf{e}_{r,c} + \mathbf{e}_{r,c+1}}{4}$  and  $\bar{\mathbf{f}}_{r,c} \equiv \frac{\mathbf{f}_{r,c} + \mathbf{f}_{r+1,c} + \mathbf{f}_{r,c+1} + \mathbf{f}_{r+1,c+1}}{4}$ . (B.5) is the composite *s-lifting* step on vertex point. (B.2) and (B.4) become the *s-lifting* step of edge points around the vertex  $\mathbf{v}_{r,c}$ .

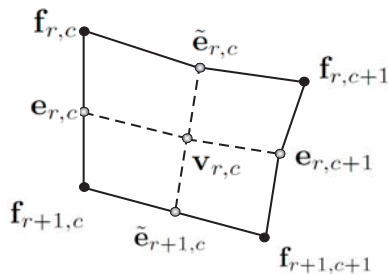


Fig. 50. An example of a rectilinear grid.

## APPENDIX C

## USER INTERACTION FOR INITIALIZATION

The user interaction can be implemented by incorporating CBCT volumetric image and its skull shape [Fig. 51(a)]. This skull shape is calculated by the simplest approach: thresholding segmentation and March Cube Algorithm. It is only used to provide reference for user interaction. Only a slice of the volumetric image is visualized in 3D space each time. It can be switched to the previous slice or the next slice. The skull shape can be temporarily hidden to visualize the internal content of the slice. Therefore, one has two objects to help identify a desired landmark point: the rough skull model and slices of the volumetric image. Landmark points are pinpointed on the slice of the image, and their coordinates are recorded.

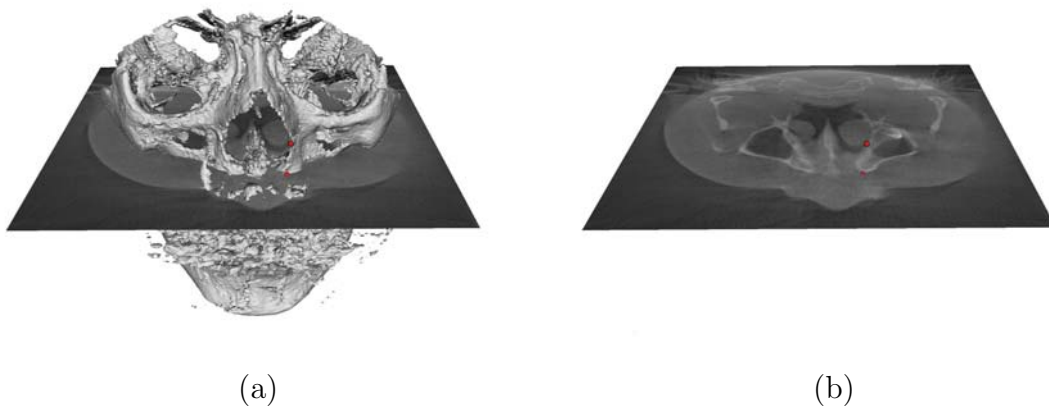


Fig. 51. (a) Selection of landmark points for initialization using user interaction. (b) The same user interaction but the skull shape is hidden to visualize the internal content of the slice.

## APPENDIX D

## II-LINE BPF ALGORITHM

Fig. 52(a) shows the geometry and the trajectory of circular cone-beam CT in the midplane.  $\theta$  is defined as the gantry rotational angle of the source starting from  $y$ -axis counterclockwise. The  $\pi$ -line concept is originated from the helical cone-beam CT reconstruction algorithms [100], but the modification in circular cone-beam CT geometry was first introduced by Pan *et al.* [101]. Fig. 52(b) shows the 3D view of the gantry rotation and  $\pi$ -line segments. The trajectory of the source lies on  $z = 0$  plane, and the imaginary trajectories (dotted circles) on the planes with  $z \neq 0$ . The  $\pi$ -line segments are defined as parallel chords on these circular trajectory and imaginary ones. Let  $\mathbf{r} = (x_r, y_r, z_r)$  be a point on the  $\pi$ -line segment  $\overline{CD}$  of the  $z = z_r$  plane and  $\mathbf{r}(\theta_A)$  and  $\mathbf{r}(\theta_B)$  points  $A$  and  $B$  on the trajectory, where  $\theta_A$  and  $\theta_B$  are the rotational angles of the source at  $A$  and  $B$ . All parallel  $\pi$ -line segments have the same direction defined by a unit vector:

$$\mathbf{u}_\pi = \frac{\mathbf{r}(\theta_A) - \mathbf{r}(\theta_B)}{\|\mathbf{r}(\theta_A) - \mathbf{r}(\theta_B)\|}. \quad (\text{D.1})$$

Assume the  $\pi$ -line segment  $\overline{AB}$  has the same  $x$ - and  $y$ - coordinates as the  $\overline{CD}$  except that they are at different  $z$  planes. Hence, the point  $\mathbf{r}$  in 3D space with a specific  $\pi$ -line direction  $\mathbf{u}_\pi$  can be uniquely determined by a quadruple  $(\lambda, \theta_A, \theta_B, z_r)$  as

$$\mathbf{r} = \mathbf{r}(\theta_A) + z_r \mathbf{u}_z + \lambda \mathbf{u}_\pi \quad (\text{D.2})$$

where  $\lambda \in [0, 1]$ , and  $\mathbf{u}_z = (0, 0, 1)$ . The reconstruction has two steps: first, backproject the projections into the  $k$ -line segments, and secondly, perform Hilbert transformation along each of  $\pi$ -line segments. The 3D volume is union of  $\pi$ -line segments and, for simplicity, one can describe the practical reconstruction of 3D images only on a  $\pi$ -line segment based on the theoretical results in [100].

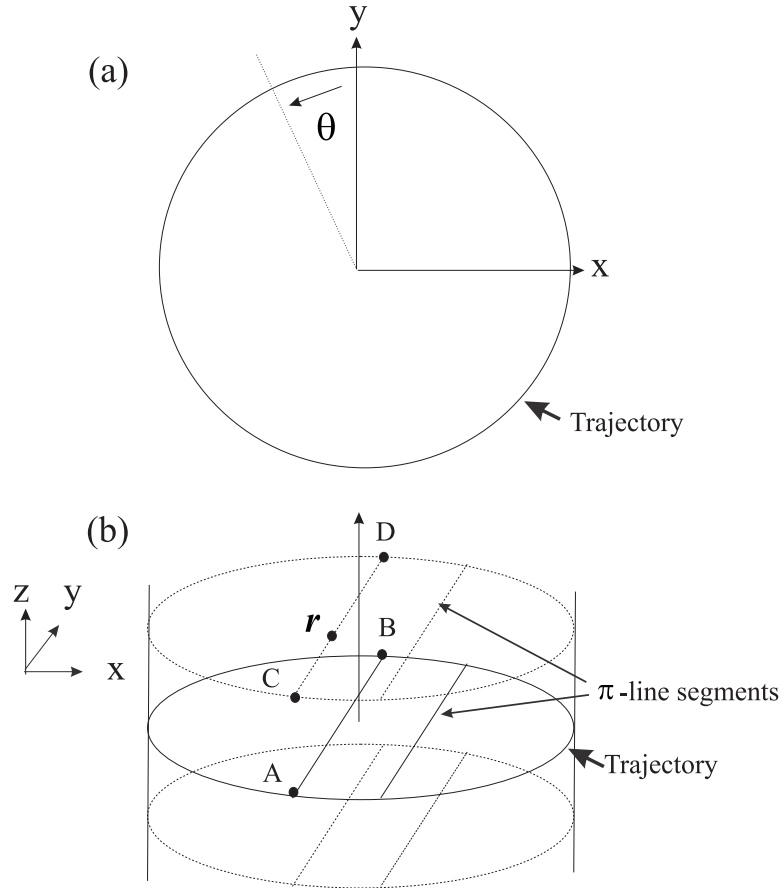


Fig. 52. Geometry of  $\pi$ -line reconstruction. (a) the trajectory in midplane  $z = 0$ . (b)  $\pi$ -line segments are defined as the chords on the circular trajectory which lies on the midplane  $z = 0$  and imaginary ones (dotted circles).

Consider the  $\pi$ -line segment  $\overline{AB}$ . Let  $\mathfrak{P}_{\parallel\theta}(u, v)$  be the projection image at some rotational angle  $\theta$  with the same  $u$ - $v$  coordinate mentioned above and  $L$  be the distance between the source and the detector. By (D.2),  $\mathbf{r}$  is equivalent to  $(\lambda, \theta_A, \theta_B, z_r)$ . The backprojected image  $b(\lambda, \theta_A, \theta_B, z_r)$  or  $b(\mathbf{r})$  on the  $\pi$ -line segment  $\overline{CD}$  is expressed as

$$\begin{aligned}
 b(\lambda, \theta_A, \theta_B, z_r) = & \int_{\theta_A}^{\theta_B} \frac{L^2}{(R + x \sin \theta - y \sin \theta)^2} \frac{\partial}{\partial u} \left( \frac{R}{\sqrt{u^2 + v^2 + L^2}} P_{\theta}(u, v) \right)_{(u,v)=(u_r, v_r)} d\theta \\
 & + \frac{P_{\theta_B}(u_r, v_r)}{d(\mathbf{r}, \theta_B)} - \frac{P_{\theta_A}(u_r, v_r)}{d(\mathbf{r}, \theta_A)} \quad (\text{D.3})
 \end{aligned}$$

where  $d(\mathbf{r}, \theta)$  is defined as the distance between  $\mathbf{r}$  and  $\mathbf{r}(\theta)$ .  $P_\theta(u_{\mathbf{r}}, v_{\mathbf{r}})$  is the line-integral which starts from the source at the rotational angle  $\theta$ , passes through the point  $\mathbf{r}$ , and ends at a point  $(u_{\mathbf{r}}, v_{\mathbf{r}})$  on the detector. Finally, the reconstructed image along the  $\pi$ -line segment  $\overline{CD}$  is

$$\hat{f}(\lambda, \theta_A, \theta_B, z_r) = \frac{1}{2\pi} H \left\{ \sqrt{(\lambda_B - \lambda)(\lambda - \lambda_A)} b(\lambda, \theta_A, \theta_B, z_r) \right\} \\ + \frac{1}{2\pi \sqrt{(\lambda_B - \lambda)(\lambda - \lambda_A)}} \left( P_{\theta_A}(u_{\mathbf{c}}, v_{\mathbf{c}}) + P_{\theta_B}(u_{\mathbf{c}}, v_{\mathbf{c}}) \right) \quad (\text{D.4})$$

where  $\mathbf{c}$  is the midpoint of  $\overline{CD}$ , and  $H \left\{ a(\lambda) \right\}$  is the Hilbert transform of  $a(\lambda)$ .  $[\lambda_A, \lambda_B]$  is an interval so that  $\left\{ \mathbf{r}(\theta_A) + z_r \mathbf{u}_z + \lambda \mathbf{u}_\pi \mid \lambda \in [\lambda_A, \lambda_B] \right\}$  includes the support set of the object and belongs to the segment  $\overline{CD}$ .

## VITA

Name	Yu-Bing Chang
Education	Ph.D. (Aug 2006 – May 2011) Electrical Engineering Texas A&M University, College Station, TX  M.S. (Sep 2001 – June 2003) Communication Engineering in Telecommunication and Signal Processing National Taiwan University, Taipei, Taiwan R.O.C.  B.S. (Sep 1997 – June 2001) Mechanical Engineering National Cheng Kung University, Tainan, Taiwan R.O.C.
Permanent address	WERC 244C, Department of Electrical and Computer Engineering, Texas A&M University, College Station, TX 77840.
Email	cyubing@gmail.com

The typist for this dissertation was Yu-Bing Chang.